

33
38
58
88
92
96
AD
AD

AD

USAAVLABS TECHNICAL REPORT 65-74

A METHOD FOR PREDICTING THE AERODYNAMIC LOADS AND DYNAMIC RESPONSE OF ROTOR BLADES

By

R. A. Piziali

642 221 640 782
FOR PERSONAL, SCIENTIFIC AND
TECHNICAL INFORMATION
NOT TO BE REPRODUCED
WITHOUT AUTHORITY

4.00 0.75 110.00

January 1966

Circle 1

U. S. ARMY AVIATION MATERIEL LABORATORIES

FORT EUSTIS, VIRGINIA

CONTRACT DA 44-177-AMC-163(T)

CORNELL AERONAUTICAL LABORATORY, INC.

BUFFALO, NEW YORK

Distribution of this
document is unlimited.



Disclaimers

The findings in this report are not to be construed as an official Department of the Army position, unless so designated by other authorized documents.

When Government drawings, specifications, or other data are used for any purpose other than in connection with a definitely related Government procurement operation, the United States Government thereby incurs no responsibility nor any obligation whatsoever; and the fact that the Government may have formulated, furnished, or in any way supplied the said drawings, specifications, or other data is not to be regarded by implication or otherwise as in any manner licensing the holder or any other person or corporation, or conveying any rights or permission, to manufacture, use, or sell any patented invention that may in any way be related thereto.

Disposition Instructions

Destroy this report when it is no longer needed. Do not return it to the originator.



DEPARTMENT OF THE ARMY
U. S. ARMY AVIATION MATERIEL LABORATORIES
FORT EUSTIS, VIRGINIA 23604

This report has been reviewed by the U.S. Army Aviation Materiel Laboratories and is considered to be technically sound. The report is published for the exchange of information and the stimulation of ideas.

Task 1P125901A14604
Contract DA 44-177-AMC-163(T)
USAAVLABS Technical Report 65-74
January 1966

A METHOD FOR PREDICTING THE AERODYNAMIC LOADS
AND DYNAMIC RESPONSE OF ROTOR BLADES

CAL Report BB-1932-S-1
by

R. A. Piziali

Prepared by
Cornell Aeronautical Laboratory, Inc.
Buffalo, New York

for

U. S. ARMY AVIATION MATERIEL LABORATORIES
FORT EUSTIS, VIRGINIA

*Distribution of this
document is unlimited.*

SUMMARY

An earlier effort (reference 1) proved the feasibility of a procedure for predicting the nonuniform induced velocity distributions and the corresponding airloads experienced by rotor blades. The present effort was undertaken to improve the aerodynamic representations used in this earlier work, improve the computational efficiency, and "close the loop" to enable the airloads and corresponding blade motions to be predicted simultaneously.

The aerodynamic representation was improved by satisfying the chordwise boundary condition (instead of using the lifting line representation). Considerable simplification was incorporated into the wake representation which resulted in a substantial increase in the computing efficiency and no loss of accuracy in the results. The equations of motion for the blade flapping and flapwise bending degrees of freedom were incorporated, and an iterative procedure was developed which yields a simultaneous solution for the aerodynamic loads and dynamic response experienced by the rotor blades.

The lift loading and bending moments were computed for the H-34 rotor at $\mu = 0.18$ and $\mu = 0.29$, and the HU-1A rotor system at $\mu = 0.08$ and $\mu = 0.26$. Comparisons of these results with measured results are presented both as distributions of the harmonic components and as time histories. Results of computations to investigate the sensitivity of the computed airloads and bending moments to variations in some of the wake parameters are presented and discussed.

FOREWORD

The work described in this report was performed by the Cornell Aeronautical Laboratory, Inc. (CAL), Buffalo, New York, for the U. S. Army Aviation Materiel Laboratories, (USAAVLABS), Fort Eustis, Virginia, over the 15 month period beginning 30 March 1964. This work is an extension of work accomplished at CAL over a period of years beginning in 1960 under Contract DA 44-177-TC-698.

Mr. R. A. Piziali was project engineer and author of this report. Mr. J. Balcerak and Mr. R. Whalen assisted in programming the computational procedure for the IBM 7044 EDP. The contributions of Dr. H. Daughaday and the many discussions with Messrs. R. P. White, Jr., F. A. DuWaldt, A. R. Trenka, and Dr. I. C. Statler of CAL were helpful and are appreciated by the author. Mr. J. Yeates administered the project for USAAVLABS.

BLANK PAGE

CONTENTS

	<u>Page</u>
SUMMARY	iii
FOREWORD	v
LIST OF ILLUSTRATIONS	viii
SYMBOLS	x
INTRODUCTION	1
ASSUMPTIONS	2
WAKE REPRESENTATION	4
BLADE REPRESENTATION	8
COMPUTATIONAL PROCEDURE	15
COMPUTER PROGRAM	19
COMPUTED RESULTS AND COMPARISON WITH MEASURED RESULTS	20
CONCLUSIONS AND RECOMMENDATIONS	31
REFERENCES	33
DISTRIBUTION	70
APPENDIXES	
I. Two-Dimensional Oscillating Wing Investigation of Wake Shed Vortex Representation	72
II. The Chordwise Induced Velocity Distribution Due to A Wake Vortex Element	81
III. Efficient Method for Numerically Computing Derivatives of Periodic Functions	86
IV. Flow Diagram for the Computer Program (Parts 1 and 2)	88

ILLUSTRATIONS

<u>Figure</u>		<u>Page</u>
1	Example of Possible Wake Configurations	35
2	The Tip-Path-Plane Oriented Coordinate System Used for Computing the Induced Velocities	36
3	Example of the K -Subscript Notation for Airload Points In Rotor Disk When $NR = 3$, $NA = 8$	36
4	Coordinate System Used in Blade Representation	37
5	Relation Between Wake Vortex Strengths and the NRA Bound Vortex Strengths When $NR = 3$, $NA = 8$	37
6	Major Steps in the Iterative Procedure of Solving the Equations	38
7	Segmentation of Rotor Blades for Computations	39
8	Measured and Computed Lift and Bending Moments; HU-1A at $\mu = 0.26$	40
9	Measured and Computed Lift and Bending Moments; HU-1A at $\mu = 0.08$	44
10a	Computed Quasi-Steady Γ , Total Γ , and Lift at $r/R = 0.95$; HU-1A at $\mu = 0.08$	48
10b	Computed Induced Velocity at $r/R = 0.95$; HU-1A at $\mu = 0.08$	49
11	Measured and Computed Lift and Bending Moments; H-34 at $\mu = 0.29$	50
12	Measured and Computed Lift and Bending Moments; H-34 at $\mu = 0.18$	54
13a	Computed Quasi-Steady Γ , Total Γ , and Lift at $r/R = 0.95$; H-34 at $\mu = 0.18$	58
13b	Computed Induced Velocity at $r/R = 0.95$; H-34 at $\mu = 0.18$	59
14a	Computed Pitching Moments; HU-1A at $\mu = 0.26$	60
14b	Computed Pitching Moments; HU-1A at $\mu = 0.08$	61

<u>Figure</u>		<u>Page</u>
14c	Computed Pitching Moments; H-34 at $\mu = 0.29$	62
14d	Computed Pitching Moments; H-34 at $\mu = 0.18$	63
15	Computed Pitching Moments about Midchord; H-34 at $\mu = 0.18$	64
16a	Comparison of Computed Lift at $r/R = 0.95$ for Wake with and without a Concentrated Root Trailing Vortex; HU-1A at $\mu = 0.26$	65
16b	Comparison of Computed Bending Moment at $r/R = 0.21$ with and without a Concentrated Root Trailing Vortex; HU-1A at $\mu = 0.26$	65
17	Distorted Tip Vortices on Retreating Side of Rotor Disk as Used in Computation; Blades in the $\psi = 90^\circ$ and 270° Positions; HU-1A at $\mu = 0.03$	66
18	Comparison of Lift at $r/R = 0.95$ Computed with and without Wake Distortion; HU-1A at $\mu = 0.08$	67
19	Comparison of Lift at $r/R = 0.95$ Computed for Two Positions of the Tip Vortex in the Wake; HU-1A at $\mu = 0.08$	67
20	Comparison of the Induced Velocity at $r/R = 0.95$ for Two Radial Positions of the Tip Vortex in the Wake; HU-1A at $\mu = 0.08$	68
21	Relative Orientation of the Blade and Recent Tip Vortices on Advancing Side of the Disk; HU-1A at $\mu = 0.08$	69

APPENDIXES

I. 1	Two-Dimensional Oscillating Airfoil Lift and Pitching Moment Transfer Functions; Zero Wake Advance ($D=1, \bar{\alpha}$)	77
I. 2	Two-Dimensional Oscillating Airfoil Lift and Pitching Moment Transfer Functions; 0.70 Wake Advance ($D=1+\bar{\alpha}/3$)	79
IV. 1	Flow Diagram for Part 1 of Computer Program	90
IV. 2	Flow Diagram for Part 2 of Computer Program	93

SYMBOLS

ADV	wake advance
A_n	Glauert coefficients
$\overline{A}_{ns}, \overline{B}_{ns}$	Fourier coefficients of generalized airload in the s^{th} degree of freedom
a_{ns}, b_{ns}	Fourier coefficients of blade response in the s^{th} degree of freedom
BA	blade azimuth position number
b	blade semichord
C_{L_α}	airfoil lift-curve slope
C_s	coefficient of the quasi-steady damping term
D	normalized (by semichord) distance from airfoil midchord to first shed vortex
\bar{d}	normalized (by semichord) shed vortex spacing
$f_s(r)$	normalized blade mode shape in the s^{th} degree of freedom
G_s	generalized airload in the s^{th} degree of freedom
g	structural damping
\dot{h}	blade section plunging velocity (positive upward)
I	quasi-steady part of Γ
K	subscript denoting collocation points in rotor disk
KA	azimuth position number
\mathcal{L}	blade section lift per unit span
$\bar{\mathcal{L}}$	stalled blade section lift per unit span
$\Delta \mathcal{L}$	cross-flow drag force for the blade section
M_s	generalized mass in the s^{th} mode
m	blade section pitching moment about midchord
\bar{m}	stalled blade section pitching moment about midchord

$\bar{m}_s(r)$	bending moment distribution in the s^{th} mode
NA	number of azimuth positions used in the computation
ND	number of degrees of freedom used in the computation
NR	number of blade radial segments used in the computation
NW	number of revolutions of wake used in the computation
NRA	total number of collocation points in rotor disk; $NRA = NR \times NA$
p_{ij}	wake element end points
q_s	tip deflection in the normal modes
R	total blade radius
r	radius to a blade section
\bar{r}	ratio of computed r to maximum value (stalled value) allowed
S_n	cosine components of the chordwise induced velocity coefficients ($n = 0, 1, 2, \dots$)
s	subscript denoting each blade mode
t	time
Δt	time increment corresponding to each azimuth increment i. e., $\Delta t = \Delta \psi / \Omega$
U	wake transport velocity in the X -direction
V_t	rotor translational velocity
$v(\theta)$	geometric or quasi-steady part of the chordwise normal velocity distribution
$\bar{v}(\theta)$	total chordwise normal velocity distribution
V_1	tangential component of total local velocity at blade section
V_2	normal component of total local velocity at blade section
V_T	total local velocity at blade section
w	wake transport velocity in the Z -direction

$w(\theta)$ chordwise normal induced velocity distribution

$\bar{w}(r, \psi)$ specified induced part of Z -component of wake transport velocity

X number of shed vortices per cycle of the airfoil motion

x chordwise coordinate (positive aft)

α_e effective angle of attack of blade section relative to V_f

α_g geometric angle of attack of blade section relative to shaft plane
(plane normal to shaft)

α_s compliment of shaft angle relative to V_f

α_T tip-path-plane angle relative to V_f

α_m stall angle for airfoil section

Γ total bound vorticity of blade section

$\gamma(\theta)$ chordwise bound vorticity distribution

θ secondary chordwise coordinate defined by $x = -b \cos \theta$

μ advance ratio; $\mu = \frac{V_f \cos \alpha_T}{\Omega r}$

ρ air density

σ induced velocity coefficients of Γ -equations

ϕ displacement of blade section relative to shaft plane

ψ azimuth angle

$\Delta\psi$ azimuth increment, $\Delta\psi = \frac{2\pi}{NA}$

Ω blade rotational speed

ω_s natural frequency of the s^{th} mode

INTRODUCTION

The U. S. Army Aviation Materiel Laboratories (USAAVLABS) have been directing a unified experimental and theoretical research effort which has for its objective the improvement of the state of the art used in the design and development of V/STOL aircraft. As a participant in this effort, Cornell Aeronautical Laboratory, Inc. (CAL) has been working on the development of a more accurate means (suitable for use in the design and development of rotor systems) of predicting the performance of rotors and the aeroelastic response experienced by the rotor blades.

The feasibility of the overall approach to predicting the nonuniform inflow distribution resulting from the wake of the rotor blades was demonstrated in an earlier initial effort (reference 1) conducted at CAL, in which the wake configuration was specified and the prediction of the blade response was circumvented by assuming the response to be given. This "open loop" (with respect to the blade response) approach enabled concentration of the effort on the aerodynamic aspect of the problem. Because of the encouraging results of the initial effort, the present second phase was undertaken to improve the aerodynamic representation of the blades and wake, compute the aerodynamic moments, "close the loop" to enable the blade motions to be predicted, and simplify the computer program.

ASSUMPTIONS

The method developed to predict the aerodynamic loads and dynamic response experienced by the blades of a rotor system in steady-state translational flight is based on the following principal assumptions:

1. The wake configuration can be adequately prescribed.
2. The blade slopes in the spanwise direction, and the section angles of attack below stall are small.
3. The inplane components of the induced velocities at the tip-path plane are small and can be neglected.
4. Below stall, the lift-curve slope is constant.
5. The blade section circulation is limited to a maximum value for angles of attack at and above stall.
6. For angles of attack above stall, the blade section normal force is taken as the sum of the stall-limited circulatory force and a cross-flow drag force.
7. The Mach number and Reynolds number effects are assumed to influence only the lift-curve slope.
8. The interference effects of the rotor hub, fuselage, etc., are negligible.

The first assumption (that of being able to prescribe adequately the wake configuration) is believed to be one of the major sources of discrepancy between the computed and measured results. Computations which indicate the sensitivity of the predicted results to the wake configuration have been made and will be presented in a latter section of this report.

"Wake configuration" means the time history of the spacial distribution of the vorticity which streams from each blade. In reality, a continuous sheet of shed and trailing vorticity streams from each blade with strengths proportional to the time and radial rates of change of the bound vorticity. Under the influence of the forces of viscosity and the three-dimensional induced velocity field (due to itself and the blade) through which it moves, this vortex wake diffuses, dissipates, and distorts. The exact configuration of this wake is not completely known and the state of the art is not sufficiently advanced to permit detailed prediction of this wake configuration.* The tip vortices, however, are

* There is some (as yet, unpublished) work proceeding at CAL which has developed a method for computing the displacement time history of a system of segmented concentrated vortices of finite core streaming from the rotor blade tips when their strength distribution is specified.

known to exist and persist; the form of these vortices has been visualized (e. g., the smoke studies of references 2 and 3).

It was desired to concentrate effort on the rotor aeroelastic prediction problem without having to undertake the equally complex problem of predicting the wake configuration. It was felt, moreover, that the wake configuration could be prescribed well enough to allow the development of the remaining aspects of the method to proceed. This approach has enabled the method of predicting rotor blade aeroelastic response to be developed and proved practical. The computed results cannot, of course, be any better than the prescribed wake configuration, but the problem of adequately predicting the wake configuration can now be undertaken separately.

The method for predicting rotor aeroelastic response, as presently developed, has several limitations which are really additional assumptions arbitrarily imposed only to expedite the development of the overall procedure; they are as follows:

1. Only the equations of motion for the flapwise degrees of freedom were included. The equations of motion for the remaining degrees of freedom (i. e., pitch, torsion, and the inplane degrees of freedom) and all the significant mass, elastic, and geometric coupling between all degrees of freedom remain to be included.
2. The rotor control settings are assumed known, and the total resultant force and moment computed for the rotor were not required to balance the fuselage forces and moment; i. e., the rotor-fuselage trim constraints are not imposed.

Now that the overall procedure has been developed and proved feasible, the additional degrees of freedom and coupling of item 1, above, can be incorporated and the additional aspect of the problem described in item 2 can be included to make the method complete and practical for use in the analysis, design, and development of rotor systems.

WAKE REPRESENTATION

As in reference 1, the shed and trailing vorticity distributions in the wake of each blade are represented by an arrangement of concentrated straight-line vortex segments; however, the arrangement of these vortex segments is now somewhat different than was used previously.

In the present representation, the azimuthal extent, behind each blade, of the grid of straight-line vortex segments representing the shed and trailing vorticity distributions can be truncated where desired and the wake continued on as segmented root and/or tip trailing vortices. (The grid can still be carried for the full extent of the wake, if desired.) The radial positions of the root and/or tip trailing vortices in the wake can be adjusted to account for the contraction of the wake. This wake representation can better represent the actual wake which, apparently, rolls up very quickly into a tip vortex (see the smoke studies of references 2 and 3). Figure 1(a) illustrates an example of a portion of a wake representation with a root and tip trailing vortex, and Figure 1(b) one with only a tip vortex (for this example, five radial blade segments have been used).

In the wake representation of reference 1, a segmented shed vortex was deposited in the flow at each azimuth position of the blade; thus, the nearest shed vortex to the blade was behind it a distance proportional to the time it takes the blade to traverse one azimuthal increment. The adequacy of this representation of the wake shed vorticity was investigated by using it in a computational model to predict the lift and pitching-moment transfer functions (for both the pitching and plunging cases) for a two-dimensional oscillating airfoil at zero mean angle of attack. The results were compared with the classical analytical solutions for this problem and, as was expected, the agreement was not very good. A computational investigation of discrete shed wake representations was then conducted by use of this computational model for the two-dimensional oscillating wing problem. It was found that reasonable agreement could be obtained in the reduced frequency range of interest by using the equally spaced discrete shed vortex representation if the entire wake were advanced, with respect to the blade producing it, a distance proportional to 70 percent of a time increment. Thus, on the basis of this result, the wake representation presently used is such that the wake of each blade can be advanced any desired amount. A description of the two-dimensional oscillating wing investigation of the discrete shed vortex wake representation and the results of it are presented in Appendix I.

It should be noted that the two-dimensional unsteady wake effects of thin-airfoil theory arise from the shed vorticity; whereas, for a three-dimensional oscillating wing, there is an additional source of the unsteady wake effects which is the attached trailing-type vorticity. The time-varying strength of the trailing vorticity from an oscillating three-dimensional wing influences the wing in the same manner as the shed vorticity; i. e.,

it attenuates and shifts the phase of the lift response to the time-varying angles of attack just as the shed vorticity. It is believed that the representation of the trailing vorticity reproduced these unsteady wake effects quite well.

In reality, the shed and trailing vorticity distributions in the wake streaming from each blade are respectively proportional to time and radial rates of change of the bound vorticity. Therefore, in the wake representation used, the strengths of the shed vortex elements deposited in the wake at each azimuth position are made equal to the change in strength (between azimuth positions) of the corresponding bound vortex elements. The strengths of the trailing vortex elements (in the grid portion of the wake) are made equal to the change in strength of adjacent bound vortex elements. Beyond the truncation of the wake grid, the root and/or tip trailing vortex strengths are made equal to the maximum value of the radial distribution of the bound vorticity on the blade in the azimuth position from which the elements were shed. The effects of viscous dissipation are neglected and, thus, the strengths of the wake vortex elements do not change with time.

Each wake vortex segment end point is given an individual transport velocity when it is deposited in the wake; thus, the transport velocities of the wake element end points which originate from each point in the rotor disk can be different. All wake element end points move with their individual velocities only for a specified (in the program input) number of time increments; for the remaining time increments, they all move with a common velocity. The initial wake element transport velocity distribution over the disk, the specified number of time increments they move with their individual velocities, and the common velocity they all acquire after this specified number of time increments are all input parameters. With this means of wake description, it is possible to (1) have all the wake element end points move with a common velocity for their entire life (i. e., an undistorted skewed helical wake), (2) have all the wake element end points move with individual velocities for their entire life (i. e., continuously distorted from the skewed helix), or (3) have all the wake element end points move with individual velocities only for a specified length of time and then revert to a common velocity (i. e., distorted from the skewed helical wake for a fixed length of time and then maintain that distorted configuration while moving away at uniform velocity).

This flexibility of describing the wake was built in only to allow various wake configurations to be tried and to determine the sensitivity of the results to each variation; it does not permit true wake distortions to be used. In reality, each element of the wake experiences a nonperiodic but time-varying transport velocity. The actual configurations of the wake streaming from each blade are not completely understood. For example, there is some question as to whether the shed vorticity persists long enough or is in such a configuration that it can significantly influence the following blades. Likewise, does the trailing vorticity from

the inboard portion of the blades (that vorticity of opposite sense to that of the tip vorticity) persist and assume a configuration (trailing root vortex) such that it can have a significant influence on the following blades?

The tip vortices and their configurations have been made visible (references 2 and 3). The observed distortions of these tip vortices from skewed helices are primarily the result of the mutual induced velocities between successive coils (layers) of the wake. These observed distortions are the initial phases of the rolling-up of the helices into two wing-like trailing vortices (i. e., downstream from the disk, the rotor wake is practically the same as a wing wake). These distortions are influenced by the advance ratio, the disk loading, and the number of blades in the rotor generating the vortices. A skewed stack of equally spaced parallel vortex rings will exhibit the same characteristic distortions. The initial phase of the rolling-up of the tip helices into two wing-like trailing vortices can best be observed in the downstream views of the rotor wake made visible in the smoke studies of reference 3.

In order to predict the distortions of these tip vortex helices, it will be necessary to evaluate the total induced velocity at each point on these vortices at successive increments of time allowing the vortex elements to move with their respective instantaneous velocities during each time increment. For sufficiently small time increments and enough collocation points, it should be possible to predict these distortions (i. e., displacement time histories)*

The computation of the wake-induced velocities at the blades is carried out in a nonrotating tip-path plane oriented (i. e., XY - plane is parallel to tip-path plane) coordinate system which is illustrated in Figure 2. The coordinate system translates with the rotor system at velocity, V_f ; thus, the wake element transport velocities in the X and Z directions are, respectively, $U = V_f \cos \alpha_T$ and $W = V_f \sin \alpha_T + \bar{w}(r, \psi)$ where $\bar{w}(r, \psi)$ is a distribution over the rotor disk of the induced part of the Z -component of the wake transport velocity. In this computational procedure, it is this component which makes it possible for each wake element end point to have an individual transport velocity. The wake transport in the Y -direction is taken to be zero; in reality, the transport in the Y -direction would be due to only the induced velocities in that direction and would result in a lateral distortion of the wake.

The wake element end points in the wake of a blade are labeled as ρ_{ij} where i denotes the azimuthal distance of the point in the wake behind the blade and j denotes the radial wake position; this notation is illustrated in Figure 1(a). The equations for the X , Y and Z coordinates of the wake points ρ_{ij} are (for $i \geq 2$)

* See footnote on page 2.

$$X = (V_f \cos \alpha_T) \left(\frac{\Delta \psi}{\Omega} \right) (i-1.0 - ADV) + r_j \cos(BA-i+ADV) \Delta \psi + (1.5) b_j \sin(BA-i+ADV) \Delta \psi$$

$$Y = r_j \sin(BA-i+ADV) \Delta \psi - (1.5) b_j \cos(BA-i+ADV) \Delta \psi$$

$$Z = -(V_f \sin \alpha_T - \bar{\omega}(r_j, \psi_{KA})) \left(\frac{\Delta \psi}{\Omega} \right) (i-1.0 - ADV) + \phi_{oc}(r_j)$$

where BA is the azimuth position of the blade shedding the wake, ADV is the fraction of a time increment that the wake is advanced, r_j is the radius to the blade segment end points, b_j is the blade semichord at the blade segment end points, ψ_{KA} is the azimuth position of the blade when the wake element end point was shed, and $\phi_{oc}(r_j)$ is the steady deflection of the blade segment end points. The coordinates of the points p_{ij} when $i = 1$ are simply the coordinates of the blade trailing edge at the ends of the blade segments.

BLADE REPRESENTATION

For the blade representation, the theory of two-dimensional, unsteady, thin airfoils has been used. The blade is divided into NR spanwise segments, and the chordwise aerodynamic boundary condition is satisfied at the midsection of each of these segments for the blade in each of NA azimuth positions; thus, there are a total of NRA ($\equiv NR \times NA$) points in the rotor disk where the boundary condition is satisfied and the airloads are computed. The subscript notation for these points over the disk is given in Figure 3. The spanwise loading is assumed constant over each of these blade segments, and it is from the ends of these segments that the trailing vorticity of the wake representation streams with strength equal to the change in strength of the bound vorticity between adjacent segments. The three-dimensional effects due to the interaction of a spanwise segment with its neighbors has not been included. Thus, each blade segment is considered to be two-dimensional, and the three-dimensional effects of the wake are included at each blade radial station.

The chordwise aerodynamic boundary condition requires that the sum of the velocities normal to the chord be zero (i. e., there can be no flow through the airfoil). The chordwise distribution of these normal velocities is composed of three parts. The first part is termed the quasi-steady part and is due to orientation of the blade segment relative to the total local velocity vector, its camber, and its pitching and plunging velocities associated with the blade dynamic response. The second part is termed the wake-induced velocity and is computed from the wake vortex representation. The third part, termed the airfoil-induced velocity, is that due to the bound vorticity distribution and is required to balance the sum of the first two parts. That is, it is the bound vorticity distribution which is considered to be the unknown and must be such as to create an airfoil-induced velocity distribution which just cancels the sum of the quasi-steady and wake-induced velocities. This sum of the quasi-steady and wake-induced velocities is, thus, termed the impressed velocity distribution because, when it is impressed on the airfoil, a bound vorticity distribution is called for to create canceling airfoil-induced velocities.

The coordinate system used for description of the blade representation is shown in Figure 4 where the airfoil chord is centered on the x -axis with the leading and trailing edges at $-b$ and $+b$, respectively. For convenience in the formulation, a transformation is made to a secondary coordinate, θ , by the following transformation:

$$x = -b \cos \theta \quad (1)$$

Let the chordwise distribution of bound vorticity (i. e., the chordwise singularity distribution required to satisfy the boundary condition) on a given blade radial station, for each instant of time, be expressed in a Glauert series, thusly:

$$\gamma(\theta, t) = 2 \left[A_0(t) \cot \frac{\theta}{2} + \sum_{n=1}^{\infty} A_n(t) \sin n\theta \right]. \quad (2)$$

The total circulation on the airfoil is given by

$$\Gamma = \int_{-b}^{+b} \gamma(x) dx.$$

Thus,

$$\Gamma = 2\pi b (A_0 + \frac{1}{2} A_1). \quad (3)$$

The chordwise distribution of the pressure difference is given by the following form of the linearized Bernoulli equation for unsteady flow,

$$\Delta p(x, t) = \rho \left[V_1 \gamma(x, t) + \frac{\partial}{\partial t} \int_{-b}^x \gamma(\xi, t) d\xi \right] \quad (4)$$

and can be expressed in terms of the Glauert coefficients by substituting (2) into (4), thusly:

$$\begin{aligned} \Delta p(\theta, t) = & 2\rho V_1 \left[A_0 \cot \frac{\theta}{2} + \sum_{n=1}^{\infty} A_n \sin n\theta \right] \\ & + 2\rho b \frac{\partial}{\partial t} \left[(A_0 + \frac{1}{2} A_1) \theta + (A_0 + \frac{1}{2} A_2) \sin \theta \right. \\ & \left. + \frac{1}{2} \sum_{n=2}^{\infty} \frac{1}{n} (-A_{n-1} + A_{n+1}) \sin n\theta \right]. \end{aligned} \quad (5)$$

The airfoil unsteady lift and pitching moment about the midchord per unit span can also be expressed in terms of Glauert coefficients by substituting (5) into the following expressions:

$$\begin{aligned} \mathcal{L} &= \int_{-b}^{+b} \Delta p(x) dx \\ \mathcal{M} &= - \int_{-b}^{+b} x \Delta p(x) dx ; \end{aligned}$$

thus,

$$\mathcal{L} = 2\pi b \rho V_1 \left[A_0 + \frac{1}{2} A_1 + \frac{b}{2V_1} \frac{\partial}{\partial t} (3A_0 + A_1 + \frac{1}{2} A_2) \right] \quad (6)$$

$$\mathcal{M} = \pi b^2 \rho V_1 \left[A_0 + \frac{1}{2} A_2 - \frac{b}{2V_1} \frac{\partial}{\partial t} (A_0 + \frac{3}{4} A_1 - \frac{1}{4} A_3) \right]. \quad (7)$$

It should be noted the lift depends only on the first three coefficients of the Glauert series, and pitching moment depends only on the first four.

Due to real fluid effects, the bound circulation, lift, and pitching moment do not experimentally attain the magnitudes given by equations (3), (6), and (7). An empirical correction factor, $C_{l\alpha}/2\pi$, is therefore applied to the bound circulation and the circulatory part of the lift and moment; the $C_{l\alpha}$ is the measured lift-curve slope for the airfoil section. The bound circulation, lift, and pitching moment are thus

$$\Gamma = C_{l\alpha} b (A_0 + \frac{1}{2} A_1) \quad (8)$$

$$\mathcal{L} = C_{l\alpha} b \rho V_1 (A_0 + \frac{1}{2} A_1) + \pi b^2 \rho \frac{\partial}{\partial t} (3A_0 + A_1 + \frac{1}{2} A_2) \quad (9)$$

$$\begin{aligned} \mathcal{M} = \frac{1}{2} C_{l\alpha} b^2 \rho V_1 (A_0 + \frac{1}{2} A_1) + \frac{1}{2} \pi b^2 \rho V_1 (-A_1 + A_2) \\ - \frac{1}{2} \pi b^3 \rho \frac{\partial}{\partial t} (A_0 + \frac{3}{4} A_1 - \frac{1}{4} A_3). \end{aligned} \quad (10)$$

The computation of the lift, moment, and Glauert coefficients is in the time domain and for each radial station the Glauert coefficients are known only at NA equally spaced discrete azimuth positions. Numerically the time derivatives indicated in equations (9) and (10) were evaluated at these discrete points by a procedure which "effectively" fits the points with a Fourier series and then takes the slope of this curve. This procedure is presented in Appendix III.

Because the bound vortex strength for each radial segment is periodic and the wake vorticity depends on the radial and time rates of change of the bound vorticity, each of the strengths of the wake vortex elements can be expressed in terms of the NRA bound vortex strengths as indicated in Figure 5. If the relative orientations of the blade segments and the wake elements are known (or prescribed), application of the Biot-Savart law enables the chordwise distribution of induced velocity on a blade segment at a point, K , in the disk to be expressed in terms of the wake vortex strengths and, thus, in terms of the NRA strengths of the bound vorticity as

$$w_K(x) = \sum_{j=1}^{NRA} C_{Kj}(x) \Gamma_j \quad (11)$$

where $C_{Kj}(x)$ is the sum of the Biot-Savart coefficients (expressing the induced velocity distribution over the chord due to a single straight-line element) for all wake elements whose strengths depend on Γ_j . The derivation of the expression for the chordwise-induced velocity distribution due to a single arbitrarily oriented vortex filament is presented in Appendix II.

For each blade segment and instant of time (i. e., at each point, K , in the rotor disk), the expression of the chordwise aerodynamic boundary condition is given by the following integral equation:

$$v_K(x) + w_K(x) - \frac{1}{2\pi} \int_{-b}^{+b} \frac{\gamma_K(\xi) d\xi}{x - \xi} = 0, \quad (12)$$

where

$$\left. \begin{aligned} v_K(x) &= (-\dot{h} + V_1 \alpha_g + \dot{\alpha}_g x)_K \\ \text{and} \\ w_K(x) &= \sum_{j=1}^{NRA} C_{Kj}(x) \Gamma_j \end{aligned} \right\} \quad (13)$$

are, respectively, the quasi-steady and wake-induced parts of the chordwise normal velocity distribution. If the wake-induced part of the normal velocity distribution (expressed in the θ -coordinate) is expanded in a Fourier cosine series

$$w_K(\theta) = \sum_{j=1}^{NRA} (S_{0Kj} + \sum_{n=1}^{\infty} S_{nKj} \cos n\theta) \Gamma_j, \quad (14)$$

then the impressed velocity distribution which is defined as the sum of the quasi-steady and wake-induced velocities can be written as

$$v_K(\theta) + w_K(\theta) \equiv \bar{v}_{0K} + \sum_{n=1}^{\infty} \bar{v}_n \cos n\theta \quad (15)$$

where

$$\left. \begin{aligned} \bar{v}_{0K} &= (-\dot{h} + V_1 \alpha_g)_K + \sum_{j=1}^{NRA} S_{0Kj} \Gamma_j \\ \bar{v}_{1K} &= (-b \dot{\alpha}_g)_K + \sum_{j=1}^{NRA} S_{1Kj} \Gamma_j \\ \bar{v}_{nK} &= \sum_{j=1}^{NRA} S_{nKj} \Gamma_j ; \quad n = 2, 3, 4, \dots \end{aligned} \right\} \quad (16)$$

and S_{nKj} is the sum of the n^{th} harmonic cosine components (of the Biot-Savart coefficients) for each wake element whose strength depends on Γ_j . The derivation of the expressions for the first four cosine components of the chordwise normal induced velocity distribution (i. e., S_0 , S_1 , S_2 and S_3) due to a single wake vortex filament is presented in Appendix II.

The result of evaluating the integral of (12), after changing to the θ -coordinate and substituting (2) for $\gamma_K(\theta)$ is also a cosine series,

$$+ \frac{1}{2\pi} \int_{-b}^{+b} \frac{\gamma_K(\xi) d\xi}{x - \xi} = +A_{0K} - \sum_{n=1}^{\infty} A_{nK} \cos n\theta. \quad (17)$$

By substituting (15) and (17) into (12),

$$\bar{v}_{0K} + \sum_{n=1}^{\infty} \bar{v}_{nK} \cos n\theta = A_{0K} - \sum_{n=1}^{\infty} A_{nK} \cos n\theta, \quad (18)$$

and equating the coefficients of like terms, the Glauert coefficients can be expressed in terms of the coefficients of the series representing the impressed velocity distribution, thusly:

$$\left. \begin{aligned} A_{0K} = \bar{v}_{0K} &\equiv (-\dot{h} + V_1 \alpha_g)_K + \sum_{j=1}^{NRA} S_{0Kj} \Gamma_j \\ A_{1K} = -\bar{v}_{1K} &\equiv (+b \dot{\alpha}_g)_K - \sum_{j=1}^{NRA} S_{1Kj} \Gamma_j \\ A_{nK} = -\bar{v}_{nK} &\equiv - \sum_{j=1}^{NRA} S_{nKj} \Gamma_j \quad n = 2, 3, 4, \dots \end{aligned} \right\} \quad (19)$$

As a result of this identification of Glauert coefficients with the cosine coefficients of the impressed velocity distribution, the lift and moment are seen to depend on only the first four coefficients of the cosine expansion of this impressed velocity distribution.

From (8) and (19), the equation for the bound vortex strength at a point, K , of the disk is

$$\Gamma_K = C_{L\alpha_K} b_K (-\dot{h} + V_1 \alpha_g + \frac{1}{2} b \dot{\alpha}_g)_K + C_{L\alpha_K} b_K \sum_{j=1}^{NRA} (S_{0Kj} - \frac{1}{2} S_{1Kj}) \Gamma_j \quad (20)$$

or by letting

$$\left. \begin{aligned} I_K &\equiv C_{L\alpha_K} b_K (-\dot{h} + V_1 \alpha_g + \frac{1}{2} b \dot{\alpha}_g)_K \\ \sigma_{Kj} &\equiv C_{L\alpha_K} b_K (S_{0Kj} - \frac{1}{2} S_{1Kj}), \end{aligned} \right\} \quad (21)$$

equation (20) becomes

$$\Gamma_K = I_K + \sum_{j=1}^{NRA} \sigma_{Kj} \Gamma_j. \quad (22)$$

This is the equation for the bound vortex strength of each blade segment at each azimuth position (i. e., each instant of time) and, thus, the general equation of a simultaneous set of NRA equations for the bound circulations. The constant term, I_K , of each of these equations depends only on the blade response and flight condition (i.e., it depends only on the quasi-steady part of the impressed velocity distribution and is referred to as the quasi-steady bound vorticity); the second term is the induced part of Γ_K . This set of equations is solved iteratively using the Gauss-Sidel method (see reference 4).

For the present method, the only blade degrees of freedom considered are the flapping and the flapwise bending; the pitching and torsion motions

are specified. The blade normal modes are used in the description of the blade dynamic response and, thus, the total plunging displacement and velocity with respect to the rotor shaft plane (plane normal to shaft at rotor hub) are

$$\phi_{KA}(r) = \sum_{s=1}^{ND} f_s(r) q_{KA_s} \quad (23)$$

$$\dot{\phi}_{KA}(r) = \sum_{s=1}^{ND} f_s(r) \dot{q}_{KA_s} \quad (24)$$

where ND is the number of modes, and $f_s(r)$ and q_{KA_s} are, respectively the normalized bending mode shapes and tip deflections in each mode, s at each azimuth station KA .

The \dot{h} term in the I_K of (21) is the effective plunging velocity and includes, in addition to the plunging velocity of (24), the component of the rotor translational velocity, V_f , normal to the blade at each spanwise segment, thus:

$$\dot{h} = V_f \sin \alpha_s + (V_f \cos \alpha_s)(\cos \psi_{KA}) \sum_{s=1}^{ND} f'_s(r) q_{KA_s} + \sum_{s=1}^{ND} f_s(r) \dot{q}_{KA_s} \quad (25)$$

When (19) is substituted into (8), the equation for the bound vortex strength is

$$\Gamma_K = C_{l_{\alpha_K}} b_K \left(\bar{v}_0 - \frac{1}{2} \bar{v}_{1K} \right)_K \quad (26)$$

The linear part of the impressed velocity distribution is $(\bar{v}_{0K} + v_{1K} \cos \theta)$. Therefore, by use of (1), the factor $(\bar{v}_0 - \frac{1}{2} \bar{v}_1)$ of (26) can be interpreted as the value of the linear part of the impressed velocity distribution at $x = +\frac{b}{2}$ the three-quarter chord; that is, the bound vorticity depends only on the linear component of the impressed velocity distribution at the three-quarter chord. This fact is used in defining the airfoil section stall in the computation. A blade section is defined to be stalled when the linear component of the impressed velocity distribution at the three-quarter chord exceeds that on the airfoil at its measured stall angle of attack. Thus, if α_m is the measured stall angle for the section, then the value of the bound vorticity at stall, is by (26), $\Gamma_{mK} = C_{l_{\alpha_K}} b_K (V_{1K} \sin \alpha_m)$ and the section is said to be stalled when

$$\bar{R}_K \equiv \frac{\Gamma_K}{\Gamma_{mK}} = \frac{C_{l_{\alpha_K}} b_K \left(\bar{v}_0 - \frac{1}{2} \bar{v}_{1K} \right)}{C_{l_{\alpha_K}} b_K (V_{1K} \sin \alpha_m)} = \frac{\bar{v}_{0K} - \frac{1}{2} \bar{v}_{1K}}{V_{1K} \sin \alpha_m} > 1.0 \quad (27)$$

The Γ_{mK} can be computed once the value of α_m is specified. During the iterative solution of the simultaneous set of Γ -equations, the values of the Γ_K are not allowed to exceed their respective Γ_{mK} . Thus, the

magnitudes of the Γ which are shed into the wake are limited. This is an approximation to prevent large, unrealistic values of vorticity from being shed into the wake from sections which are above their stalling angle of attack.

The lift and pitching moment are computed by (9) and (10) when $\bar{R} \leq 1.0$ (i. e., when the airfoil section is below stall) but, when $\bar{R} > 1.0$ and the section is stalled, the lift and moment are approximated by the following:

$$\bar{\mathcal{L}}_K = \rho V_{1K} \Gamma_{mK} + \Delta \mathcal{L}_K \quad (28)$$

where

$$\Delta \mathcal{L}_K = 2 \rho b_K V_T^2 \sin^2 \alpha_{eK}$$

and

$$\bar{M}_K = \frac{1}{2} b_K \bar{\mathcal{L}}_K. \quad (29)$$

That is, the stalled lift is computed as the sum of the stalled (limited) circulatory lift and a cross-flow drag force, $\Delta \mathcal{L}$. The stalled pitching moment about the midchord is computed as the moment due to the stalled lift, $\bar{\mathcal{L}}_K$, acting at the quarter-chord. The velocity, V_T , is the total local resultant velocity acting normal to the spanwise axis (or midchord axis) of the local blade segment and is given by

$$V_T^2 = V_1^2 + V_2^2 \quad (30)$$

The velocities, V_1 and V_2 are the two orthogonal components of V_T in a plane normal to the local spanwise axis. Velocity V_1 lies on the intersection of this plane with a plane normal to the shaft.

$$V_1 = (V_f \cos \alpha_s) \sin \psi + \Omega r \quad (31)$$

$$V_2 = \omega - V_f \sin \alpha_s - (V_f \cos \alpha_s) \left(\frac{d\phi}{dr} \right) \cos \psi - \dot{\phi} \quad (32)$$

where ϕ is the blade displacement given by (23).

The angle, α_e (effective angle of attack), is the local angle between the line of zero lift for the airfoil and the direction of V_T ; it is given by

$$\alpha_e = \alpha_g + \delta \quad (33)$$

where $\delta = \arctan (V_2/V_1)$.

COMPUTATIONAL PROCEDURE

The computational procedure is fundamentally an iterative procedure which repetitively computes the aerodynamic loads and solves the equations of motion of the blade so as to obtain consistent airloads and blade response. The resulting solution includes all the aerodynamic coupling between the degrees of freedom.

The computational procedure requires that the wake configuration be specified; that is, that the relative orientation of the blade segments and the wake vortex elements be known. To establish this relative orientation, the first-order displacements of the blades relative to the shaft are needed. Thus, in addition to the rotor translational velocity, shaft angle, and wake transport velocities, a reasonable approximation of the steady-state displacement of the blade relative to the shaft (i. e., coning and/or steady bending), and the first harmonic cosine flapping angle are needed to establish the relative orientation of the blade segments and wake elements. If the steady blade displacement and first cosine harmonic flapping (relative to the rotor shaft) predicted by the method are significantly different from the estimates used to establish the relative orientation of the blades and wake, the computed values should be used to re-establish the wake orientation and then the computation repeated.

First, the blade and wake coordinates are computed, and then an integration (summation) over the wake is performed to obtain the matrices of induced velocity coefficients S_{0k_j} through S_{3k_j} as defined in equation (14). These coefficients are for the wake-induced velocities normal to the tip-path-plane, but are computed at the steady-state deflected positions of the blades. Because the blade spanwise slopes are small, these induced velocities are assumed to act in the direction of V_2 [equation (32)]. From these induced velocity coefficients, the matrix of coefficients, σ_{k_j} , for the simultaneous set of bound vortex equations (Γ - equations) is computed.

Next, an iterative procedure is used to solve the equations for the aerodynamic loads and blade response. (A flow diagram indicating the main conceptual elements of this iterative procedure is presented in Figure 6.) The procedure begins with a first approximation to the blade response and then evaluates the constants, I , [given by equation (21)] of the Γ - equations. The Γ - equations are next solved iteratively by use of the Gauss-Sidel method and then the Glauert coefficients evaluated by equation (19). From the Glauert coefficients, the lift and pitching moments are computed, and then a "generalized airload" is computed in each mode for each azimuth position by integrating the product of mode shape and the spanwise airload over the span. The generalized airload in each mode is then harmonically analyzed and used as the forcing function for that mode at each harmonic. The blade equations of motion for each mode are then solved for the response at each harmonic. With

this new approximation to the blade response, the I 's of the Γ - equations are recomputed and the entire computational process is repeated. This process is repeated until the blade response converges to within prescribed limits.

The generalized airload is not the forcing function as conventionally defined because it contains, in addition to the aerodynamic forces independent of the response, all the aerodynamic loads which are directly and indirectly a result of the blade response. These additional loads are the aerodynamic spring, damping and mass forces, and the aerodynamic coupling force from the wake. Normally, terms representing these aerodynamic forces that are proportional to the system response are put on the left side of the equation of motion along with the other terms which are also proportional to the system response. The forces that are independent of the system response are put on the right side of the equation. In the computational procedure which has been developed, these response-dependent components of the airload are implicit in the solution of the Γ - equations and the computation of the resultant airloads. Therefore, by using the generalized airload as the forcing function, the response-dependent airloads are effectively taken from the left side of the equation and included with the conventional forcing function on the right. This, of course, does not alter the equation of motion nor its solution. In the computational procedure described above, the generalized airload (right side of equation of motions) is evaluated for the existing approximation to the response (from previous iteration). By using this as the forcing function, the equation of motion is then solved for the next approximation to the response. Unfortunately, when this process is repeated it will not always converge.

An investigation was made to determine and understand the controlling factors of this iterative procedure. It was found that convergence of this procedure was improved when the dependence of the right side of the equation on the variables (i. e., on the response) was reduced. This is evident when the right side is, in fact, independent of the variables, then the result of the first iteration is the solution. Thus, in the computational procedure which has been developed, the dependence of the right side (i. e., the generalized airloads) on the response is reduced by subtracting an approximation for the quasi-steady damping from both sides of the equation. That is, a term which is believed to be the largest response-dependent part of the airload has effectively been brought back to the left side of the equation from the right side. This quasi-steady damping subtracted from the right side is computed as a function of the response of the previous iteration, while that subtracted from the left is computed as a function of the response of the present iteration. When the solution converges, these two are equal and the equation is unaltered. This procedure has worked very well, thus far, and the solution obtained is independent of this approximate quasi-steady damping correction term, but the rate of convergence does depend on it. It was found that both halving and doubling this term increased the number of iterations required for convergence without changing the solution.

The equations of motion for the blade which were actually used in the iterative procedure are obtained as indicated in the following. The equation of motion for a generalized coordinate q_s (tip deflection in a normal mode) expressing the balance of all the generalized forces in that coordinate is

$$M_s \ddot{q}_s + i g_s M_s \omega_s^2 \dot{q}_s + M_s \omega_s^2 q_s = G_s \quad (34)$$

where the first term on the left is the inertia force, the second is the structural damping force (proportional to the spring force but in phase with the velocity, g_s is the structural damping coefficient), the third is the spring force, and the term on the right is the generalized airload. The quasi-steady damping term to be subtracted from both sides of equation (34) to improve convergence is approximated as

$$D_s = -C_{l\alpha} \Omega \rho \dot{q}_s \int_0^R b(r) r f_s^2(r) dr \quad (35)$$

The generalized coordinate and the generalized airload are expanded in the following Fourier series:

$$q_s = a_{0s} + \sum_{n=1}^{\infty} (a_{ns} \cos n \Omega t + b_{ns} \sin n \Omega t) \quad (36)$$

$$G_s = \bar{A}_{0s} + \sum_{n=1}^{\infty} (\bar{A}_{ns} \cos n \Omega t + \bar{B}_{ns} \sin n \Omega t) \quad (37)$$

By substituting these expressions for q_s and G_s in equations (34) and (35), subtracting equation (35) from both sides of equation (34), and then equating coefficients of like terms in the result, the following are obtained as the equations of motion used in the iterative procedure:

$$\left. \begin{aligned} M_s \omega_s^2 a_{0s}^{(i)} &= A_{0s}^{(i-1)} \\ M_s (\omega_s^2 - n^2 \Omega^2) a_{ns}^{(i)} + (M_s \omega_s^2 g_s + C_s n \Omega) b_{ns}^{(i)} &= \bar{A}_{ns}^{(i-1)} + (C_s n \Omega) b_{ns}^{(i-1)} \\ M_s (\omega_s^2 - n^2 \Omega^2) b_{ns}^{(i)} - (M_s \omega_s^2 g_s + C_s n \Omega) a_{ns}^{(i)} &= \bar{B}_{ns}^{(i-1)} + (C_s n \Omega) a_{ns}^{(i-1)}; \end{aligned} \right\} \quad (38)$$

$n = 1, 2, 3, \dots$

where the superscript (i) indicates the iteration number and

$$C_s \equiv C_{l\alpha} \rho \Omega \int_0^R r b(r) f_s^2(r) dr \quad (39)$$

is the coefficient of the quasi-steady damping term. Thus for each generalized coordinate (degree of freedom) at each harmonic of the rotational speed there is a pair of simultaneous equations for the sine and cosine components of the response.

After the iterative procedure has converged, the radial distribution of the structural bending moments at each harmonic (cosine and sine) are computed from the blade response in each normal mode and the normal mode moment distributions as follows:

$$\left. \begin{aligned} \bar{M}_o(r) &= \sum_{s=1}^{ND} a_{o_s} \bar{m}_s(r) \\ \bar{M}_{na}(r) &= \sum_{s=1}^{ND} a_{n_s} \bar{m}_s(r) \\ \bar{M}_{nb}(r) &= \sum_{s=1}^{ND} b_{n_s} \bar{m}_s(r) \end{aligned} \right\} \quad (40)$$

where the $\bar{m}_s(r)$ are the bending moment distributions in each normal mode, s . It should be noted that in this procedure the steady blade displacements are represented by the sum of the steady deflections in the normal modes. While the number, ND , of modes used is adequate to represent the significant dynamic response of the blade (because the frequency response in each mode is such that significant dynamic response occurs only near the natural frequency of the mode), this number of modes is not necessarily adequate to represent the static deflection shape of the blade for purposes of computing steady bending moments. This procedure will, however, yield the static blade deflection shape with sufficient accuracy for the aerodynamic aspects of the problem. This is because the blade section effective angle of attack is a function of the blade spanwise slope (first derivative with respect to radius) whereas the bending moments depend on the local blade curvature (second derivative with respect to radius). For a more accurate prediction of the steady bending moments, corresponding to the steady-state aerodynamic loads (plus the centrifugal loading due to built-in precone, if used), one of the standard procedures for computing static deflections of beams should be used.

COMPUTER PROGRAM

The computer program is written entirely in Fortran IV for the IBM 7044 EDP, and is physically two separate programs (Part 1 and Part 2) which are run sequentially. Each part required essentially the entire available core storage capacity. The program required two tape drives in addition to the three for the monitor system input, output, and library files. Each of these two parts is subdivided into subroutines for ease and convenience of programming, check out, and the incorporation of modifications. The running time for the complete program depends on the individual problem being processed (i. e., on the number of blades, blade segments, azimuth positions, the wake configuration used, the number of revolutions of wake, the number of degrees of freedom used, and the number of iterations required to obtain the solution). For the computations which have thus far been made, Part 1 of the program has required from 0.10 to 0.20 hour and Part 2 has required from 0.15 to 0.25 hour of machine time.

Part 1 of the program generates the blade segment and wake element coordinates, and then it evaluates the matrices of induced velocity coefficients by integrating the Biot-Savart expression over the wake — these are stored on tape. Part 2 of the program evaluates the coefficients for the Γ -equations and the equations of motion; then it solves the system of equations by the iterative procedure. After the solution has converged, the time histories of all the results are harmonically analyzed and both the time histories and their Fourier coefficients are printed as outputs together with all the inputs for both parts of the program. Flow diagrams indicating the logic for both parts of the program are presented in Appendix IV.

COMPUTED RESULTS AND COMPARISONS WITH MEASURED RESULTS

The computational procedure was used to analyze two flight conditions of each of two rotor systems for which measured airloads and blade bending moments are available. These four computations are for the HU-1A rotor at advance ratios of 0.08 and 0.26, and for the H-34 rotor at advance ratios of 0.18 and 0.29. Comparisons of the measured and computed lift loads and blade-flapwise bending moments are presented; however, only the computed pitching moments are presented because measurements of them are not available.

The dynamic response of a rotor blade can be expressed in terms of its response in each of its normal modes. The response in each normal mode at each harmonic of the rotational speed is proportional to both the amplification factor and the generalized force for the specific mode and harmonic. The amplification factor is determined by the ratio of the harmonic forcing frequency to the natural frequency (of the mode under consideration), and the generalized force is determined by the mode shape and radial distribution of the airload at the specific harmonic. Therefore, to predict accurately the bending moments at each harmonic (and, thus, the total bending moments), it is necessary to know the natural frequencies and to predict the radial distribution of the airload at each harmonic accurately; it is not sufficient to simply predict time histories of the airload which look similar (that is, agree approximately in the lower harmonics) to the measured airloads at a few radial stations. Because of the importance of the harmonic components of the airload, their radial distributions are presented here, in the comparisons of the measured and computed results, in addition to the time histories of the total airload. Furthermore, presentation of the harmonics is a much more detailed view of the airload distribution (over the rotor disk) because it displays its constituents and can thus provide a much more critical comparison. Both forms of presentation are also used for the bending moments.

In addition to the computations made for comparison with the measured results, a computational investigation was made to determine the relative sensitivity to some of the input wake configuration parameters. It was found that the sensitivities depend on the particular application. The only general conclusion which can be drawn is that the wake configuration is important and a better means for establishing it more accurately is needed. Results of this investigation are presented later.

All the input information required for the computations, as well as the measured results used for the comparisons, was obtained from references 5 and 6. The bending normal mode shapes, moment distributions, and natural frequencies were computed from the blade mass and elastic distributions contained in these references. All the computations for both rotor systems were made for 24 blade azimuth positions. For the

computations, the HU-1A blade was divided into 8 spanwise segments and the H-34 into 9 spanwise segments as shown in Figure 7. The midpoints of these segments include all the radial stations for which measured airloads are available. In all the computations presented for comparison with measured results, the first three azimuthal segments of wake behind each blade were of the grid representation and the remainder of the wake was only a tip vortex positioned at 90 percent (representative contraction observed in reference 2) of the blade radius. The number of revolutions of wake varied for each case depending on the advance ratio. Unless otherwise noted, the computed momentum induced velocity is used for the induced part, $\bar{w}(r, \psi)$, of the Z -component of wake transport velocity.

The steady components (mean value) have been subtracted from the time-history presentations in the comparisons of computed and measured results, and the radial distribution of these components is presented with the other harmonic components.

HU-1A at $\mu = 0.26$

To establish the wake configuration for this case, the following are the values of the parameters used:

$$V_f = 188.0 \text{ feet per second}$$

$$\alpha_T = 5.8 \text{ degrees}$$

$$\omega(r, \psi) = -6.0 \text{ feet per second}$$

$$NW = 2 \quad (\text{Number of revolutions of wake})$$

$$ADV = 0.7 \quad (\text{wake advance})$$

The measured and computed time histories and radial distributions of the harmonics of the lift loadings and the blade-flapwise bending moments are presented in Figure 8. From the time histories, it appears that there is reasonable correlation between the measured and computed results. The correlation does not, however, appear as good when the radial distribution of the harmonics is compared. In general, the correlation for the airloads is best for the lower harmonics. The radial distributions of the higher harmonics of the airload are not as well predicted as their relative amplitudes. This is true at most harmonics of the bending moments. It is noted that above the 5th harmonic the measured and computed bending moments are insignificant.

The reversal, at the inboard end of the blade, in the radial distribution of the measured steady-bending moment is due to the centrifugal force moments (arising from the built-in precone of the blades) exceeding the lift moments at the inboard end of the blade. Because the steady component of the lift loading is overpredicted, the lift moment exceeds these centrifugal moments at the inboard end of the blade and the reversal does not occur in the computed steady-bending moment.

In the time history of the airloads, it was observed that the computed airloads are slightly advanced with respect to the measured airloads on the advancing side of the disk and retarded on the retreating side. This effect would result if the wake configuration, used in the computation, was skewed slightly more than the actual wake. Thus, a blade would see the wake of the preceding blade sooner on the advancing side and later on the retreating side. This small difference could arise because of an error in the advance ratio or because of induced velocities in the X-direction (which have been neglected), increasing the transport velocity in that direction.

HU-1A at $\mu = 0.08$

The wake configuration for this case was established by the following values of the parameters:

$$V_f = 55.1 \text{ feet per second}$$

$$\alpha_T = 2.5 \text{ degrees}$$

$$\omega(r, \psi) = -21.0 \text{ feet per second}$$

$$NW = 6 \text{ (revolutions of wake)}$$

$$ADV = 0.7 \text{ (wake advance)}$$

The time histories and radial distribution of the harmonics of the air-loading and blade-flapwise bending moments are presented in Figure 9. The correlation here is not as good as that obtained at $\mu = 0.26$. The mean value of the airloading has been underpredicted and likewise the higher harmonics of the airloading have been underpredicted. The discrepancies are attributed primarily to the wake configuration's being a poor representation of the real wake for this case. The abrupt changes in the airload on both the advancing and retreating sides of the disk (which are due to the induced velocity variation) are not well predicted for this case.

The various contributions to the computed lift loading at $r/R = 0.95$ are presented in Figure 10. Here in Figure 10a are presented, for this radial station, the quasi-steady bound vorticity, Γ , and the total bound vorticity, Γ' , together with the lift loading Z . The induced velocity (which is directly proportional to the difference between Γ' and the quasi-steady bound vorticity) is presented in Figure 10b. It is observed here that the induced velocity is most negative over the rear half of the disk and is nearly zero or positive over the forward half of disk. This is characteristic of the induced velocity distributions of translating rotors because (as observed in Figure 21) the blade stations are generally on the downwash side of the preceding blade tip vortices as the blade goes from $\psi = 270$ degrees to $\psi = 90$ degrees (rear half of disk) and on the upwash side of them as the blade goes from $\psi = 90$ degrees to $\psi = 270$ degrees (forward half of disk). It is also observed that, while the induced velocity incurs a large total change as the blade passes from the rear half of the disk to the forward half of the disk, it does not change as abruptly as would be expected (nor as is observed in Figure 13b, for the H-34 at $\mu = 0.18$). The real wake (tip vortex) is probably much closer to the rotor disk on the advancing and retreating sides of the disk because of the Z - component of the distortion of the tip vortex due to its rolling up on itself at the sides of the wake as described in the section on the wake representation. Also, corresponding distortions in the X and Y - directions could make the approach of the blade to the preceding blade's tip vortex more abrupt (i. e., the angle between

this vortex and the blade would be small) as viewed in X-Y plane rather than very gradual as was the case for this computation (where the angle is nearly 90 degrees). The reversal in the distribution of the steady-bending moment, Figure 9d, and negative value near the blade root are overpredicted for this case because the steady component of lift was underpredicted and thus the negative moments due to the centrifugal loading arising from the precone are predominant. The overall correlation of the harmonics of the bending moments appears to be fairly good compared to the correlation of the airloads. This is because the higher harmonics of the bending moments are negligible, and it is the higher harmonics of the airload which are not well predicted. The correlation of the lower harmonics of the airload is reasonable and so also are the significant lower harmonics of the bending moments.

H-34 at $\mu = 0.29$

The following parameter values were used to establish the wake configuration for this case:

$$V_f = 189.2 \text{ feet per second}$$

$$\alpha_T = 6.0 \text{ degrees}$$

$$\bar{\omega}(r, \psi) = -6.4 \text{ feet per second}$$

$$NW = 2 \text{ (revolutions of wake)}$$

The comparisons of the measured and computed time histories and harmonic distributions of the airloads and bending moments are presented in Figure 11. Because of errors in the measured steady component (zeroth harmonic) of the bending moments, they are not presented in Figure 11d. The time histories of the airload appear to correlate reasonably well. However, the harmonic distributions indicate that the correlation is primarily at the lower harmonics, while the higher harmonics are generally overpredicted. It is interesting to note that the relative correlation of the first harmonic cosine component of the lift is very similar to that obtained for the HU-1A at $\mu = 0.26$, and that the first and second harmonic components of the lift for these two cases are also similar.

It is evident from the time histories of the bending moments, that only the low harmonics correlate, and this is confirmed in the harmonic distributions. The higher harmonics are generally overpredicted. This is especially true for the eighth harmonic and is due to the third bending mode natural frequency being near the eighth harmonic of the rotational speed.

H-34 at $\mu = 0.18$

For this case, the wake configuration was established by the following values of the wake parameters:

$$V_f = 118.2 \text{ feet per second}$$

$$\alpha_T = 3.3 \text{ degrees}$$

$$\bar{w}(r, \psi) = -10.6 \text{ feet per second}$$

$$NW = 3 \text{ (revolutions of wake)}$$

$$ADV = 0.7 \text{ (wake advance)}$$

The time histories and the radial distribution of harmonics of the lift loading and bending moments are presented in Figure 12. The correlation in both the time histories and the harmonics of the airloads for this case is, in general, better than for the other cases. The abrupt rise and fall of the airloads on the advancing and retreating side of the disk, Figure 12a, have apparently been slightly overpredicted here, whereas for the low advance ratio case for the HU-1A they were underpredicted. It is also noted that the computed airloads are slightly advanced with respect to the measured airloads on the advancing side of the disk and slightly retarded on the retreating side as was noted for the HU-1A at $\mu = 0.26$. This seems to be generally true for most of the computations. Here again the harmonic distributions portray the discrepancies between the measured and computed airloads while the time histories appear to correlate reasonably well. The computed radial distributions of the steady and first harmonic components compare quite well with those measured. The computed radial distributions of the second and higher harmonics contain relatively large radial variations. Similar variations are evident in the second and third measured components but with a small amplitude.

Because of errors in the measured steady component (zeroth harmonic) of the bending moments, they are not presented in Figure 12d. The oscillatory moments correlate reasonably well, except for the higher harmonic response, due primarily to the third bending mode.

An interesting insight into the genesis of the airloading can be obtained from Figure 13, where for $r/R = 0.95$, the quasi-steady component, I , of the bound vorticity, the total bound vorticity, Γ , the airloading, \mathcal{L} , and the wake-induced velocity time histories are presented. It should be remembered that the difference between the I and Γ curves is the induced part of the bound vorticity which is proportional to the wake-induced velocity. First, it is noted for this case that the decreasing airload as the blade goes from $\psi = 0$ to $\psi = 60$ degrees is not due to the blade encountering abruptly the downwash of a trailing vortex, but is due to the rapidly decreasing quasi-steady component of Γ (i. e., due

to the blade velocity, motions, and pitch inputs). The sharp rise in the airload as the blade goes from $\psi = 300$ degrees to $\psi = 330$ degrees is similarly due to I . The sharp decrease from $\psi = 75$ degrees to $\psi = 120$ degrees and the rise from $\psi = 240$ to $\psi = 290$ degrees are partially due to the wake-induced velocity variation, but predominately the result of the I variation. The sharp rise on the advancing side, and drop on the retreating side, is due only to the wake-induced velocity variation. Thus, it is seen that the character of the airloads is strongly influenced by the quasi-steady aspect of the problem. The wake-induced velocity variations are characteristically "hat shaped", as in Figures 10b and 13b.

In the past, there has been speculation that the lift variation on the advancing and retreating sides of the disk (which resembles the "characteristic" induced velocity variation of a single vortex) was a reflection of the induced velocity field of the tip vortex of the preceding blade. From the above discussion, it is evident that this is not necessarily true. For this case, the lift variation (which has this characteristic) is the result of both the wake-induced and quasi-steady velocities and not primarily the reflection of only the induced velocity experienced by the blade section.

Pitching Moments

The measured pitching moments were not available; therefore, only the computed pitching moment time histories are presented in Figure 14. It should be noted that these pitching moments are about the airfoil midchord. The computed pitching-moment time histories are seen to be very similar to the corresponding lift time histories; this is because the predominant part of the pitching moment about the midchord is due to the lift acting at the quarter-chord. This can be seen by evaluating the pitching moments about the quarter-chord $x = -b/2$; thus,

$$\begin{aligned} M_x = -\frac{b}{2} &= -\int_{-b}^{+b} \left(x + \frac{b}{2}\right) \Delta p(x) dx \\ &= -\int_{-b}^{+b} x \Delta p(x) dx - \frac{b}{2} \int_{-b}^{+b} \Delta p(x) dx. \end{aligned} \quad (41)$$

From equations (6) and (7), these two terms are identified as the pitching moment about the midchord, M , and the moment of the lift, \mathcal{L} , acting at the quarter-chord; thus the moment about the midchord is

$$M = M_x = -\frac{b}{2} + \frac{b}{2} \mathcal{L}. \quad (42)$$

The moment about the quarter-chord can be expressed in terms of the Glauert coefficients by substituting equation (5) into (41) to obtain

$$M_x = -\frac{b}{2} = \frac{\pi}{2} b^2 \rho V_1 (A_1 + A_2) - \frac{\pi}{2} b^3 \rho \frac{\partial}{\partial t} \left[4A_0 + \frac{7}{4} A_1 + \frac{1}{2} A_2 - \frac{1}{4} A_3 \right]. \quad (43)$$

In Figure 15, for $r/R = 0.75$ and 0.95 on the H-34, the computed pitching moments about the midchord are compared with the moment due to the lift acting at the quarter-chord. The differences, while a small part of the moment about the midchord, represent the total moment about the quarter-chord (aerodynamic center), which is due entirely to the nonuniform part of the chordwise "impressed" velocity distribution and the unsteady effects; this is obvious from equations (43) and (19). These moments can, therefore, represent a significant part of the moments about the pitch and elastic axes. It should be remembered that the shed vortex wake is not well represented in the present wake configuration, and this could significantly influence these moments because they depend on higher-ordered variations of the chordwise "impressed" velocity distribution.

Sensitivity to Wake Parameters

Computations were made to determine the relative sensitivity of the results to variations in several of the wake configuration parameters. The following were investigated:

1. The effect of using a rolled-up root and tip trailing vortex versus only a tip vortex beyond the grid portion of the wake.
2. The effect of changing "wake advance" (i. e., the amount by which the entire wake is advanced with respect to the blade producing it).
3. The effect of adding distortions of the tip vortex in the Z-direction which approximate that observed in smoke studies.
4. The effect of varying the radial location of the rolled-up tip vortex (i. e., varying the contraction).

For all computations of this investigation, the first three azimuthal segments of wake behind each blade are of the grid representation and the remainder of the wake is represented by concentrated root and/or tip trailing vortices.

For the HU-1A rotor at $\mu = 0.26$, two computations were made to determine the effect of using a concentrated trailing root vortex at $r/R = 0.30$ in addition to the trailing tip vortex at $r/R = 0.90$. The strengths of these concentrated trailing vortices were equal to and

varied azimuthally as the maximum value of the radial distribution of the blade bound vorticity. It was found that adding the concentrated root vortex of strength equal to the tip vortex had a relatively small effect on the airloading and the bending moments. This is evident in Figure 16 where the time histories of the airloading at $r/R = 0.95$ and the bending moments at $r/R = 0.21$ are presented. Thus, for this rotor and flight condition, the root vortex had very little effect on the computed results.

The effect of wake advance was investigated using the HU-1A rotor at $\mu = 0.26$ where the wake advance was changed from 0.0 to 0.7. This had a relatively small effect, but, in general, increasing the wake advance attenuated and shifted the phase of the airloads, blade response, and bending moments at the higher harmonics. This attenuation was relatively large for the response in the blade modes near resonance. For example, the first antisymmetric blade response at the third harmonic decreased 30 percent, and the second antisymmetric response at the fifth harmonic decreased 38 percent. The attenuation in the higher harmonics of the lift variation is as expected because increasing the wake advance increases the effectiveness of the shed vorticity which attenuates and shifts the phase of the lift variations.

The effect of distorting the wake in the Z -direction was investigated by introducing distortions, of the form reported in references 2 and 7, into the wake of the HU-1A rotor at $\mu = 0.08$. This distortion of the tip vortex is the initial phase of the rolling up of these (initially helical) vortices into two wing-like trailing vortices and is primarily influenced by the advance ratio, the disk loading, and the number of blades in the rotor. The rotor used to visualize these distortions and the HU-1A rotor are both two-bladed. The form of the distortion used is taken, therefore, from results at comparable advance ratios in reference 7 and scaled according to the relative disk loadings for the two rotors. It was hoped that this would introduce distortions of at least the proper form and indicate their effect relative to the regular skewed helical wake.

The distortion of the wake used is shown in Figure 17, where the tip vortices on the retreating side of the rotor disk are presented. The computed airloads at $r/R = 0.95$ obtained with and without the above wake distortion are presented in Figure 18. The largest effect on the airload appears on the retreating side of the disk where the distortion was large and such as to bring the tip vortex of the preceding blade closer to the following blade.

The computations with and without distortion of the tip vortices were made for the trailing tip vortices positioned at $r/R = 0.90$. In Figure 19 is presented a comparison of the airloadings at radial station $r/R = 0.95$ when the same wake distortion was used but the position of the trailing tip vortex was changed from $r/R = 0.90$ to $r/R = 1.00$. The difference in the airloading is seen to be quite large, and the results

are similar at the other blade radial stations. The relatively large induced effect due to the blade station crossing tip vortices of the preceding blades (on the advancing and retreating of the disk) when the vortex is at $r/R = 0.90$ has been noticeably diminished when the vortex is positioned at $r/R = 1.00$. This is also evident in Figure 20 where the wake-induced velocity variations for the two cases are compared. Similar results were also obtained when the radial position of the tip vortices was changed without including the distortion of the tip vortices.

The magnitude of the jump in the wake-induced velocity from the rear half of the disk to the front half is less and more gradual with the tip vortex positioned at $r/R = 1.00$. It is also noted that the downwash over the rear half of the disk is less and the relative upwash over the front half of the disk is greater with the vortex at $r/R = 1.00$. The reason for these relatively large differences in the induced velocities and airloads between the two cases can be explained with the aid of Figure 21, where there is presented (for the advancing side of the disk) a projection of the X-Y plane of the locus of blade radial station $r/R = 0.95$ together with the X-Y plane projection of the two "youngest" tip vortices. Figure 21a is for the tip vortices positioned at $r/R = 0.90$ and Figure 21b is for the tip vortices positioned at $r/R = 1.00$. In Figure 21a (for the tip vortices at $r/R = 0.90$), it is seen that this blade station passes over these tip vortices at approximately the intersection of their projections. Thus this blade station passes from the downwash side of the two vortices to the upwash side of both of them simultaneously with a subsequent rapid change in the induced velocity from downwash to upwash.* However, in Figure 21b it is seen that, for the vortices at $r/R = 1.00$, this does not happen, but rather the blade station passes over the two vortices in a region where their projections are separated. Thus, for this case, the blade station requires a much larger azimuth interval to pass from the downwash side to the upwash side of both vortices with a subsequently slower change in the induced velocity experienced. Also, when the vortices are at $r/R = 1.00$ (Figure 21b), it is seen that on the rear half of the disk the blade station is farther from these two vortices and on this front half of the disk it is closer to them. Thus, the downwash effect will be reduced while the upwash effect will be increased as is observed in the induced velocities of Figure 20.

* It should be remembered when viewing these wake-induced velocity time histories with respect to the effects of the preceding blade wakes, that they represent the total wake-induced velocity experienced by the blade station and include the downwash of the attached near wake trailing vorticity which superimposes a negative bias on the effects of the preceding blade wakes.

Sensitivity to Blade Natural Frequencies

For the HU-1A at $\mu = 0.26$ the computed response of the second antisymmetric blade bending mode was overpredicted (see Figures 8c and 8d), and this mode is very near resonance with the fifth harmonic of the rotor speed. This situation occurs for most of the computed cases because it is impossible to avoid proximity to resonance for all the blade modes. Thus, because the damping ratios are quite small (it is estimated to be 0.035 from the computed response and phase angle of the second antisymmetric mode of the HU-1A at $\mu = 0.26$), the operating point for these bending modes can be on the very steep slopes of the amplification factor curve and small changes (or errors) in the natural frequency can have very large effects on the response in such modes. This was confirmed by making small changes in the natural frequency of the second antisymmetric mode for the HU-1A at $\mu = 0.26$. It should be noted that this is not a characteristic of the computational procedure, but rather an inherent characteristic of the physical system and will be a problem for any method of prediction. Because of this sensitivity, the blade's coupled natural frequencies should be used even if the uncoupled mode shapes are used.

CONCLUSIONS AND RECOMMENDATIONS

The results of this effort have proved the feasibility of this computational approach to the rotor aeroelastic problem. The following objectives have been attained:

1. "Closing the loop" with respect to the blade motions.
2. Satisfying the chordwise aerodynamic boundary condition.
3. Simplifying the discrete wake representation.

Considering the sensitivity of the results to the blade natural frequencies and the wake configuration, the agreement of the computed results with the measured results is quite good.

Based on this work, the following specific conclusions are made

1. The computed bending moments and airloads are sensitive to the blade natural frequencies.
2. Accurate computation of the blade airloads and bending moments requires the coupled natural frequencies of the blades to be accurately determined.
3. The computed results are sensitive to the wake configuration. For the discrete type wake representation used, it was found that, for the cases computed,
 - a. The presence of a concentrated root vortex had little effect.
 - b. Advancing the shed vortices (closer to the blade trailing edge) attenuated and shifted the phase of the computed blade response.
 - c. Distortions of the wake normal to the tip-path plane can have a significant influence on the results.
 - d. The position of the rolled-up tip vortex can have a significant effect.
4. Significant aerodynamic pitching moments about the quarter-chord are computed (for a flat plate or symmetrical airfoil) by satisfying the chordwise aerodynamic boundary condition and including unsteady effects.

The present procedure does not impose the rotor-fuselage trim constraints on the resultant rotor forces and moments; that is, the rotor shaft angle and rotor control settings are required as inputs to the computation and the rotor resultant force and moment are unconstrained results of the computation. However, in the task of designing a rotor system for a specific fuselage, c. g. location, and flight condition, it is the rotor control settings, blade stresses, and aerodynamic loads which are sought and the resultant rotor forces and moments must balance the forces and moments of the fuselage. Thus for the design and development of rotor systems, and also for the analysis of existing rotor systems, a practical method of prediction should include the appropriate trim equations.

The computational procedure in its present form is incomplete and has limited use for rotor design analysis. On the basis of the encouraging results which have been obtained with the present method, it is recommended that further effort be expended to remove its limitations. Specifically the following should be accomplished:

1. Incorporate the pitch, torsion, and in-plane degrees of freedom and the significant coupling between all degrees of freedom.
2. Develop a procedure for adequately predicting the wake configuration.
3. Incorporate the necessary rotor-fuselage trim equations into the procedure.

REFERENCES

1. Piziali, R. A., and DuWaldt, F. A., A Method for Computing Rotary Wing Airload Distribution in Forward Flight, Cornell Aeronautical Laboratory Report BB-1495-S-1, TCREC Technical Report 62-44, November 1962.
2. Tararine, S., Experimental and Theoretical Study of Local Induced Velocities Over a Rotor Disc for Analytical Evaluation of the Primary Loads Acting on Helicopter Rotor Blades, Engineering Division, Giravions Dorand Company, Report No. DE 2012, 15 October 1960.
3. Gray, R., An Aerodynamic Analysis of a Single Bladed Rotor in Hovering and Low-Speed Forward Flight as Determined from Smoke Studies of the Vorticity Distribution in the Wake, Office of Naval Research, Report No. 356, September 1956.
4. Faddeeva, V. N., Computational Methods of Linear Algebra, Dover Publications, Inc., 1959.
5. Measurement of Dynamic Airloads on a Full-Scale Semirigid Rotor, Bell Helicopter Report No. 525-099-001, TCREC Technical Report 62-42, December 1962.
6. Scheiman, J., A Tabulation of Helicopter Rotor-Blade Differential Pressures, Stresses, and Motions as Measured in Flight, NASA TM X-952, March 1964.
7. Tararine, S., Experimental and Theoretical Study of Local Induced Velocities Over a Rotor Disk, CAL/TRECOM Symposium Proceedings, Volume I, Buffalo, New York, 26-28 June 1963.

8. vonKarman, T., and Sears, W. R., Airfoil Theory for Non-uniform Motion, Journal of the Aeronautical Sciences, Volume 5, Number 10, August 1938.
9. Jeffrey, H., and Jeffrey, B. S., Methods of Mathematical Physics, Cambridge University Press, 1956.

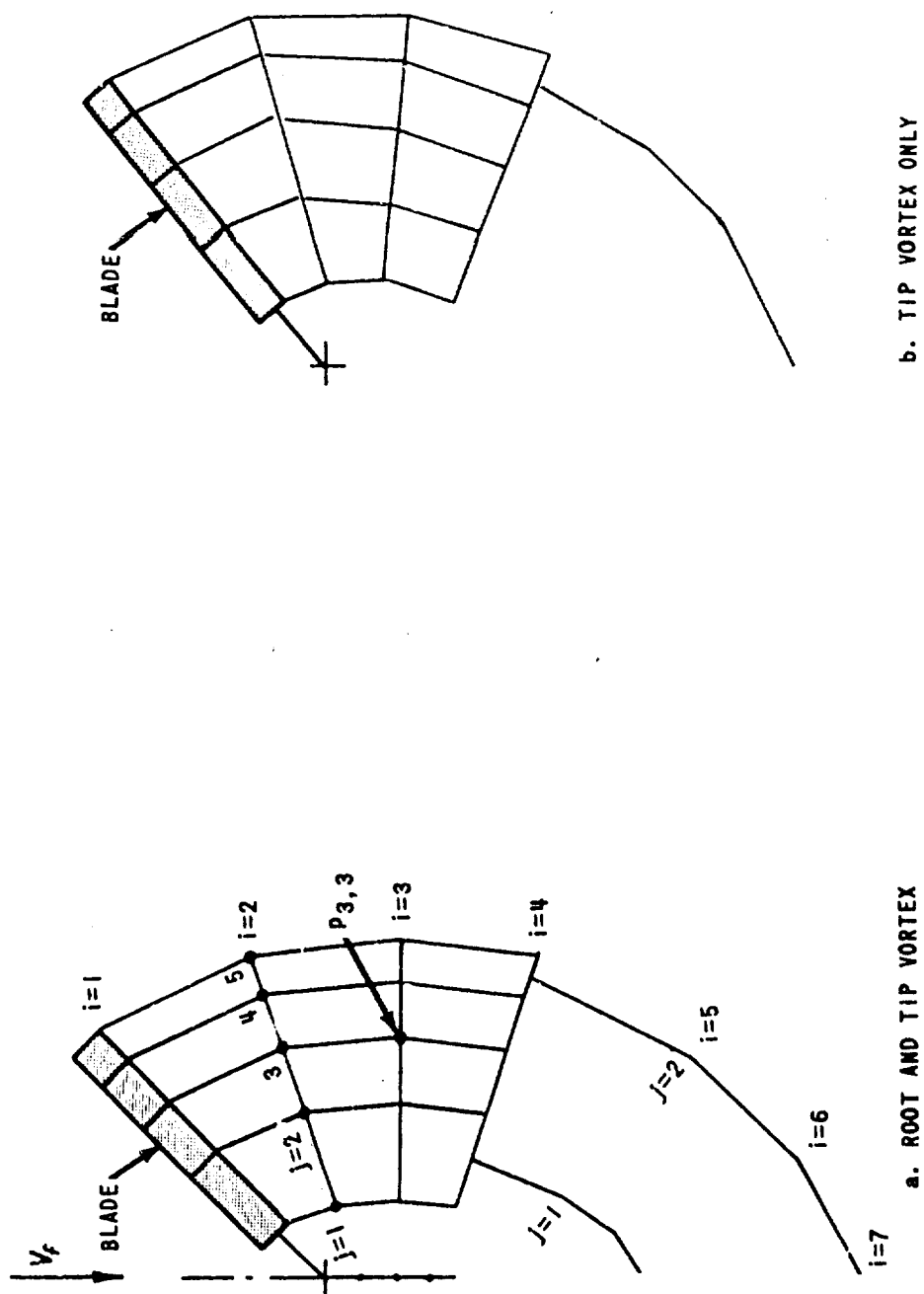


Figure 1. EXAMPLE OF POSSIBLE WAKE CONFIGURATIONS.

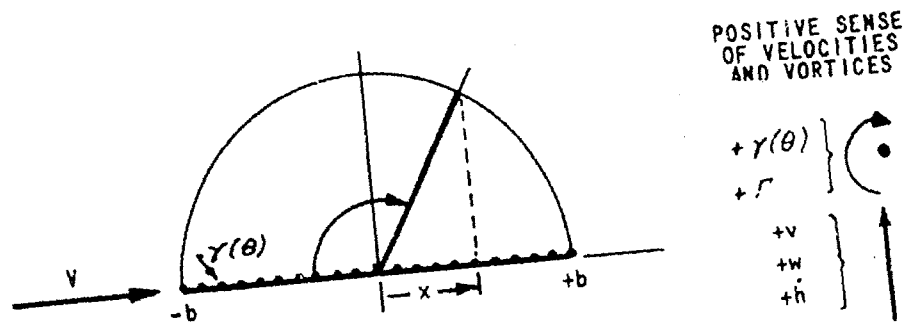


Figure 4. COORDINATE SYSTEM USED IN BLADE REPRESENTATION.

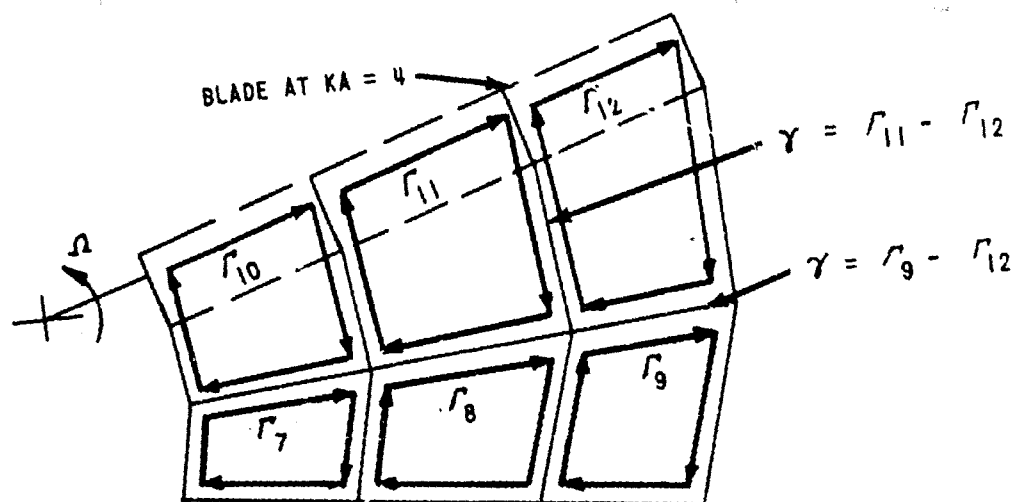


Figure 5. RELATION BETWEEN WAKE VORTEX STRENGTHS AND THE NRA BOUND VORTEX STRENGTHS WHEN $NR = 3$, $NA = 8$.

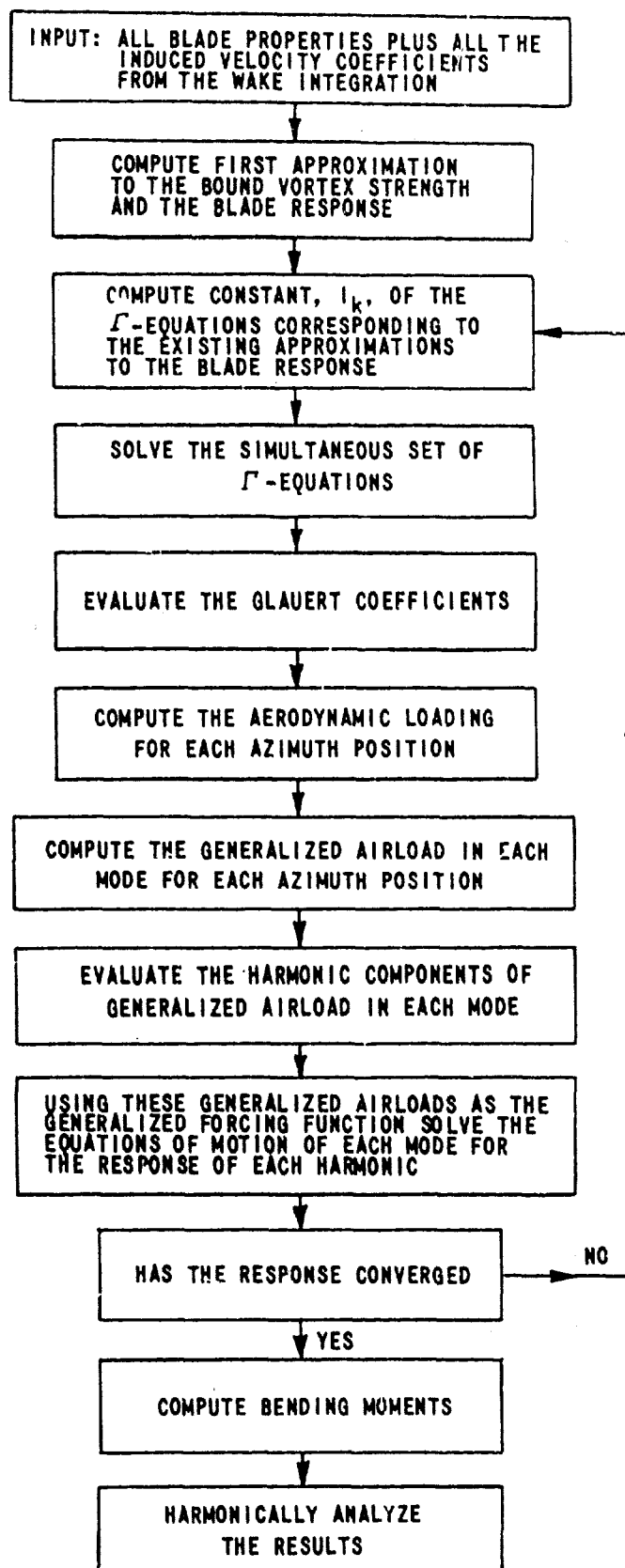


Figure 6. MAJOR STEPS IN THE ITERATIVE PROCEDURE OF SOLVING THE EQUATIONS.

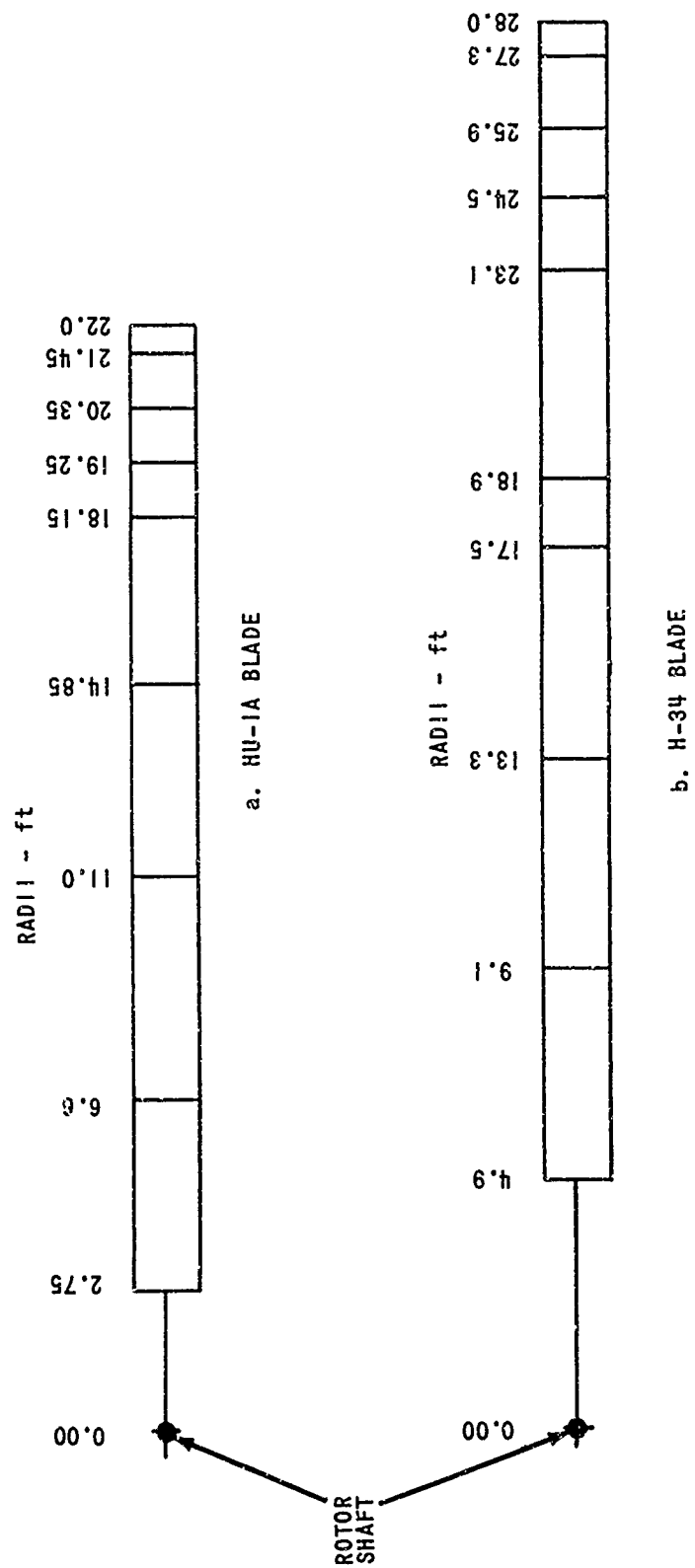
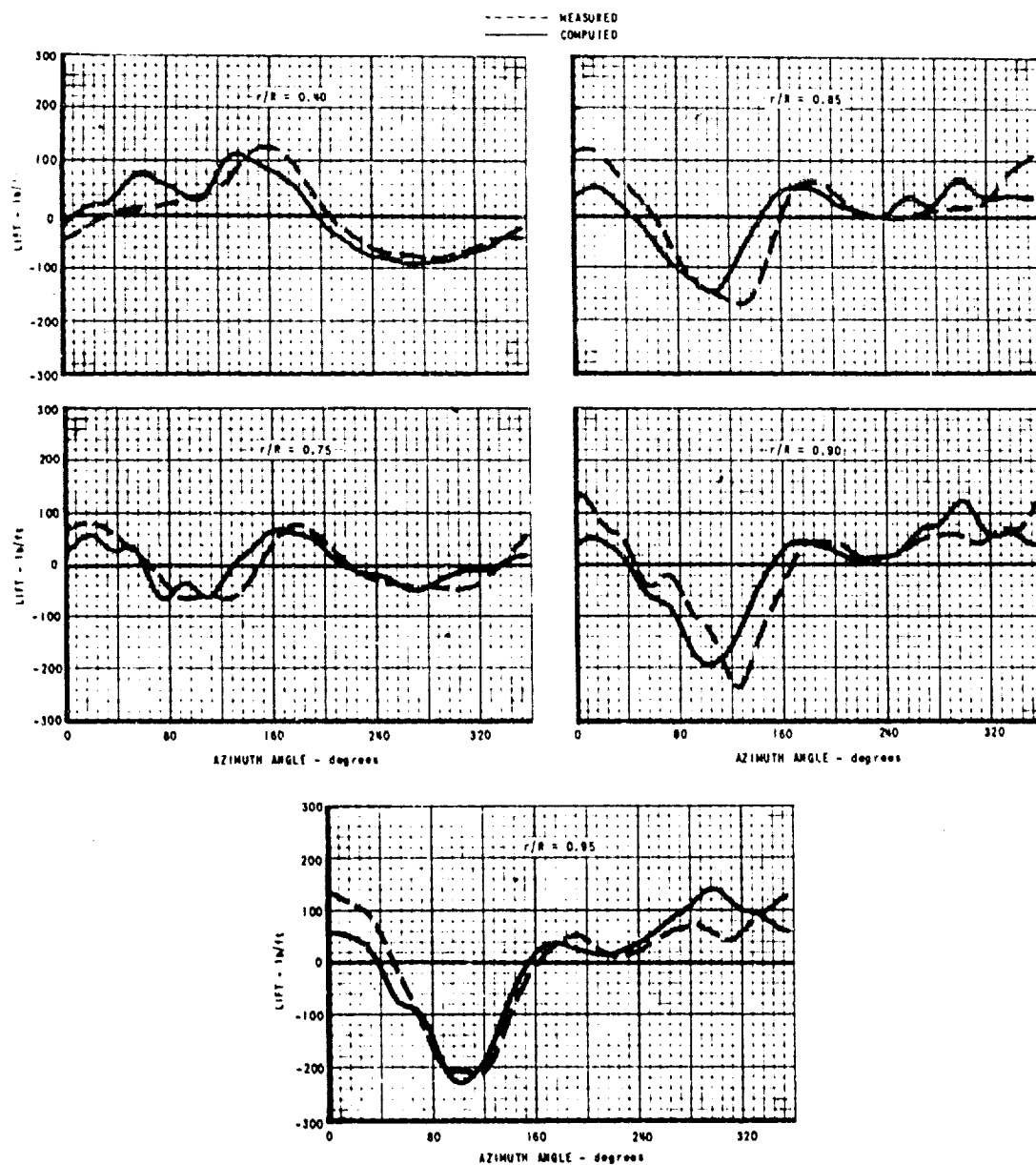
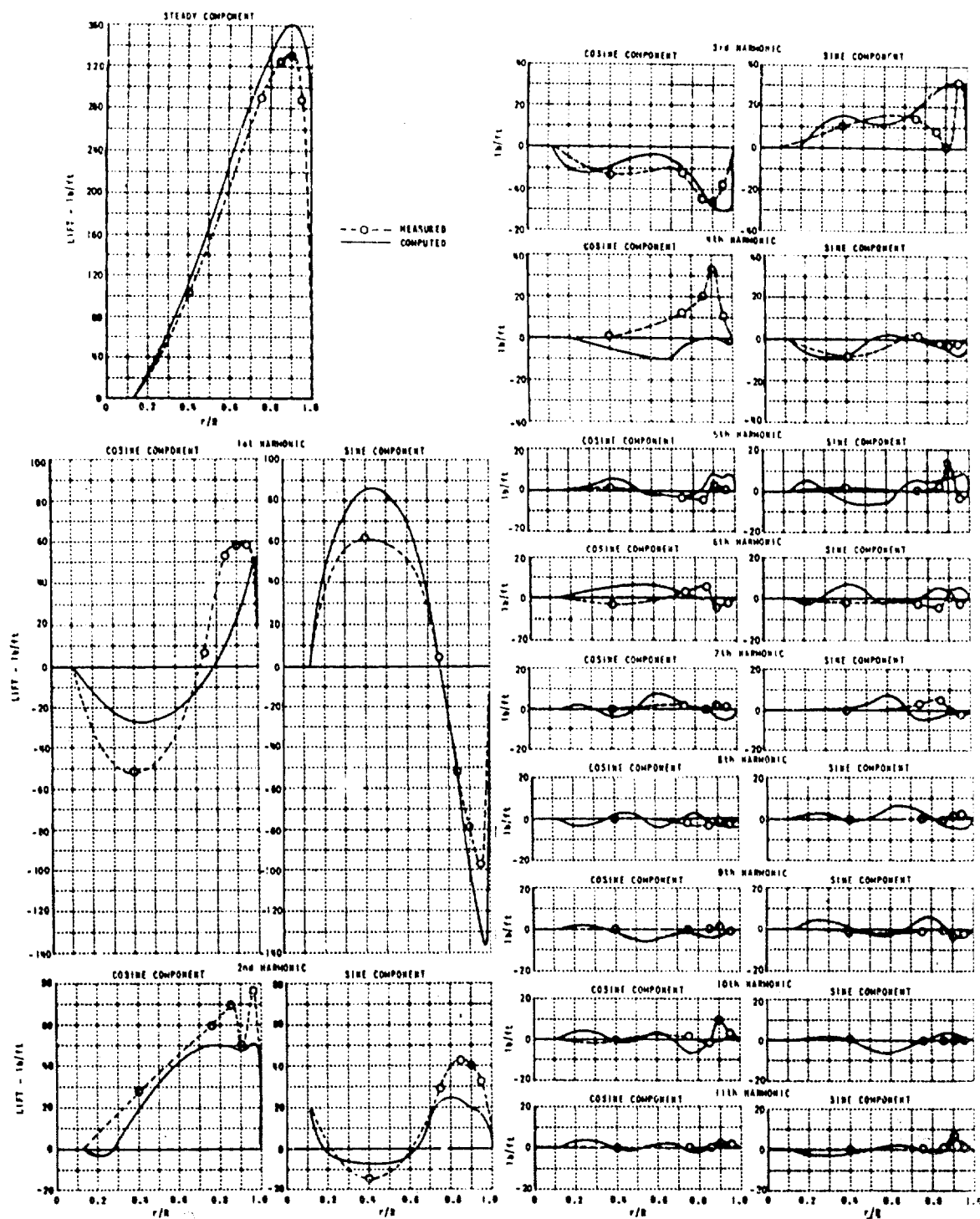


Figure 7. SEGMENTATION OF ROTOR BLADES FOR COMPUTATIONS.



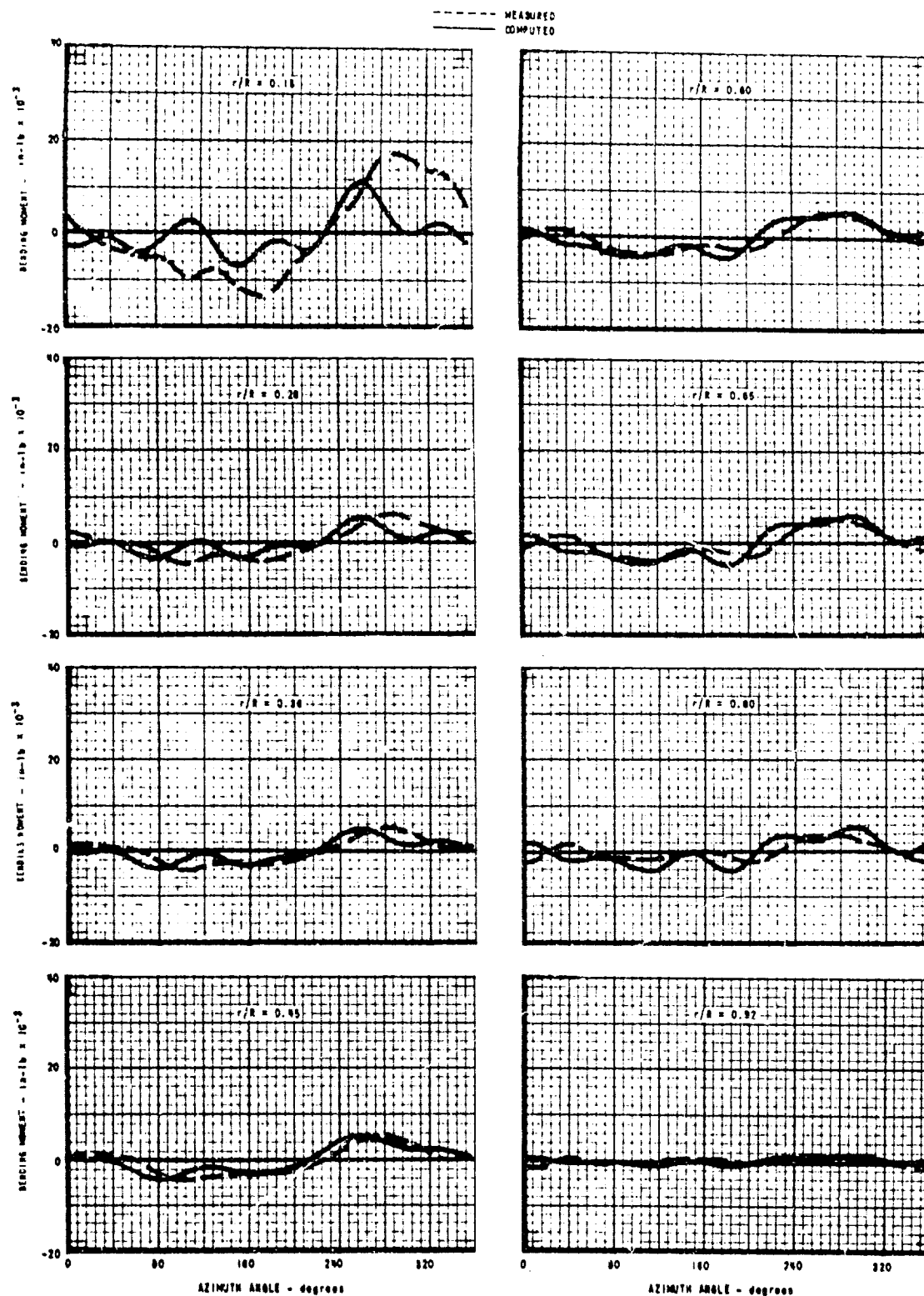
a. TIME HISTORIES OF LIFT

Figure 8. MEASURED AND COMPUTED LIFT AND BENDING MOMENTS;
HU-1A AT $\mu = 0.26$.



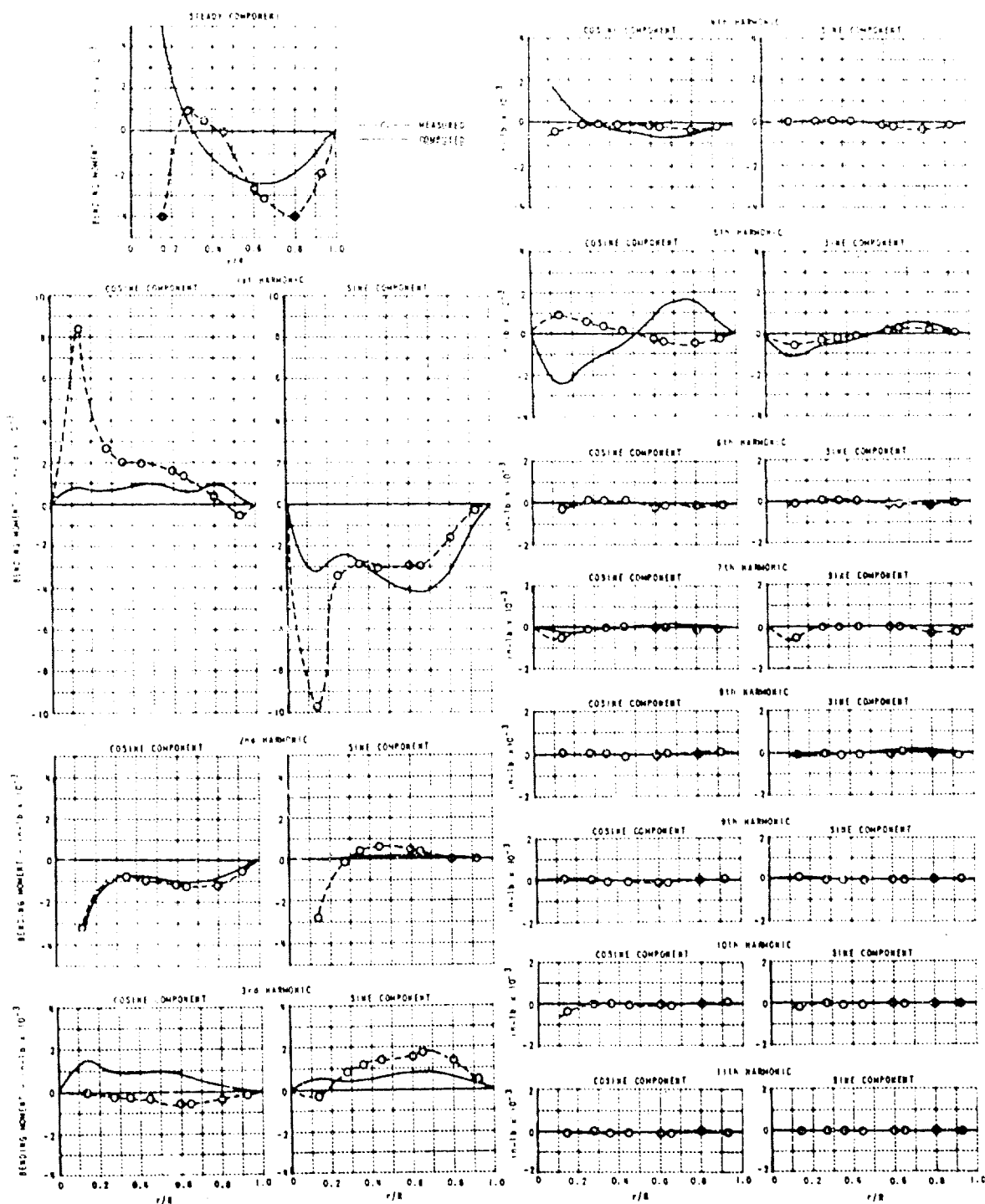
b. HARMONICS OF LIFT

Figure 8 (Cont'd). MEASURED AND COMPUTED LIFT AND BENDING MOMENTS;
HU-1A AT $\mu = 0.26$.



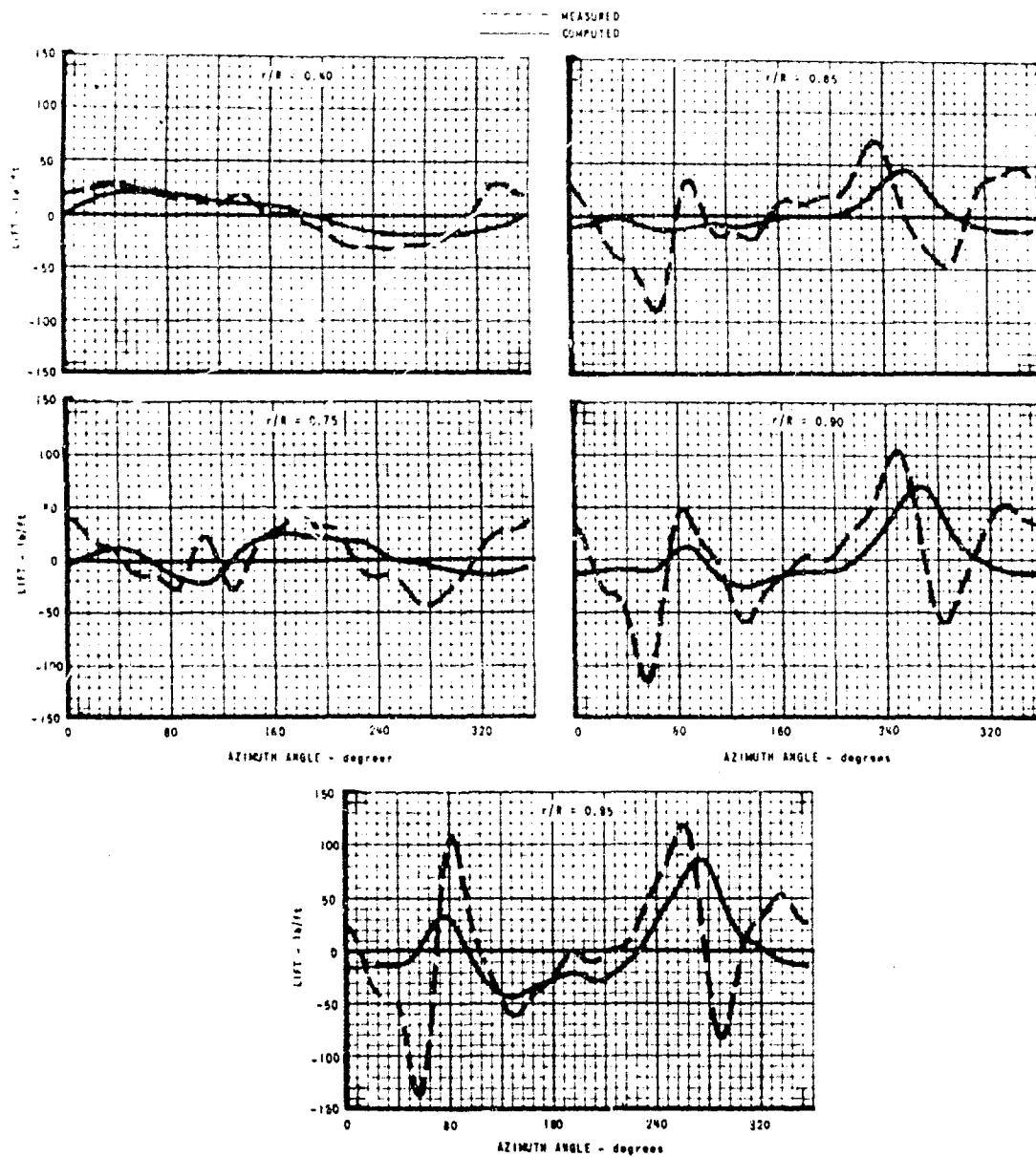
c. TIME HISTORIES OF BENDING MOMENTS

Figure 8 (Cont'd). MEASURED AND COMPUTED LIFT AND BENDING MOMENTS ;
HU-1A AT $\mu = 0.26$.



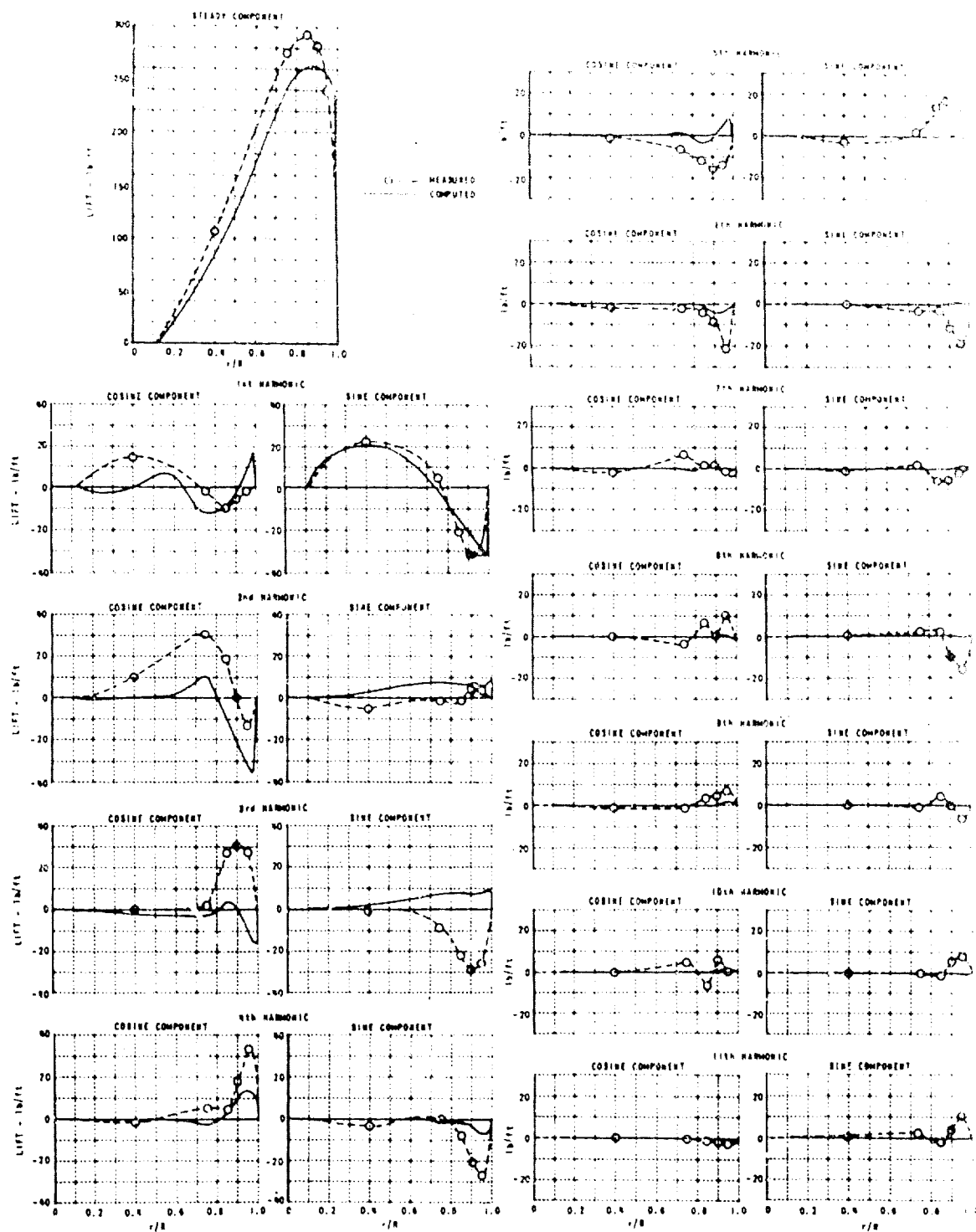
d. HARMONICS OF BENDING MOMENTS

Figure 8 (Cont'd). MEASURED AND COMPUTED LIFT AND BENDING MOMENTS;
HU-1A AT $\mu = 0.26$.



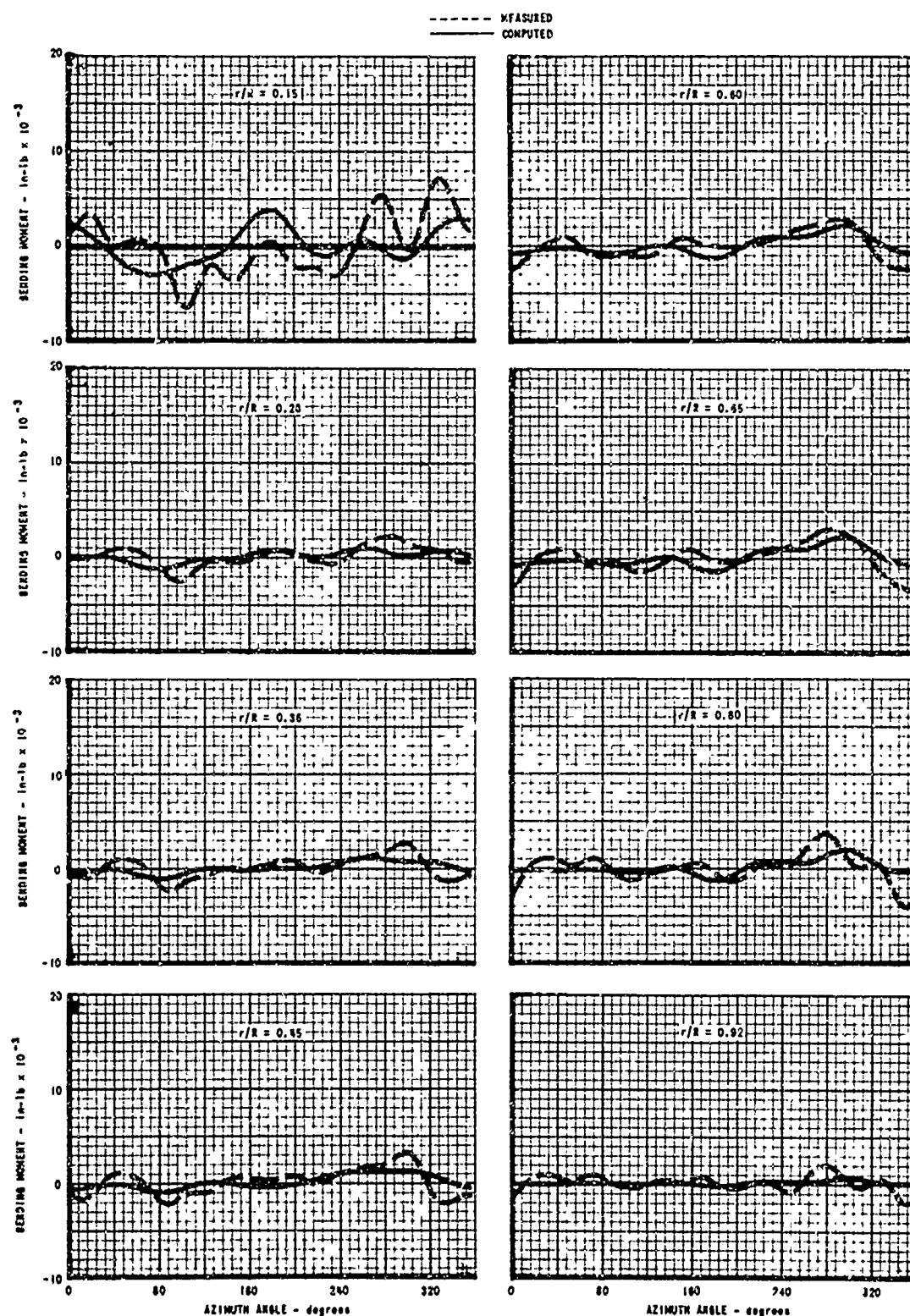
a. TIME HISTORIES OF LIFT

Figure 9. MEASURED AND COMPUTED LIFT AND BENDING MOMENTS;
HII-1A AT $\mu = 0.08$.



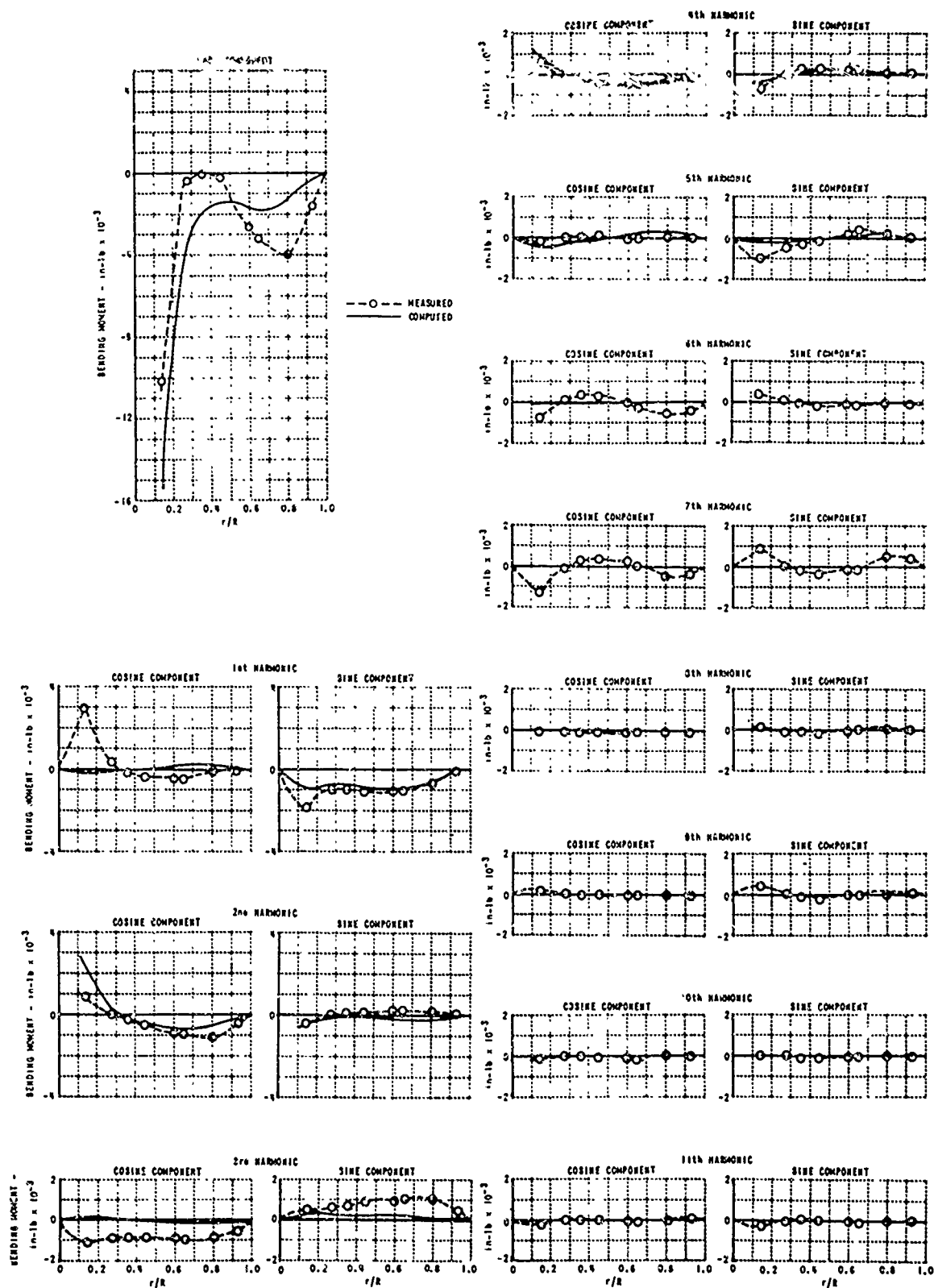
B. HARMONICS OF LIFT

Figure 3 (Cont'd). MEASURED AND COMPUTED LIFT AND BENDING MOMENTS;
HU-1A AT $\mu = 0.08$.



c. TIME HISTORIES OF BENDING MOMENTS

Figure 9 (Cont'd). MEASURED AND COMPUTED LIFT AND BENDING MOMENTS;
HU-1A AT $\mu = 0.08$.



d. HARMONICS OF BENDING MOMENTS

Figure 9 (Cont'd). MEASURED AND COMPUTED LIFT AND BENDING MOMENTS;
HU-1A AT $\mu = 0.08$.

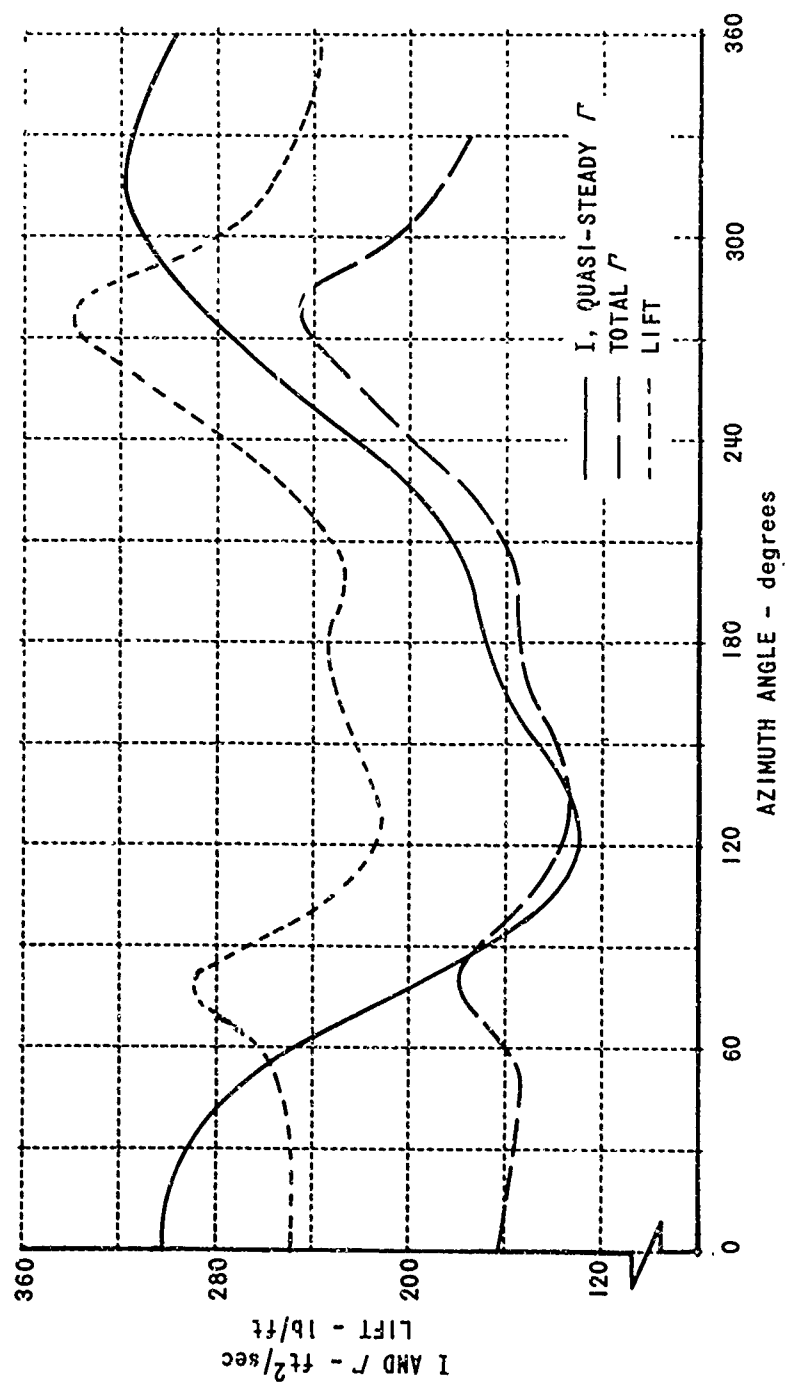


Figure 10a. COMPUTED QUASI-STEADY I' , TOTAL I' , AND LIFT AT $r/R = 0.95$; HU-1A AT $\mu = 0.08$.

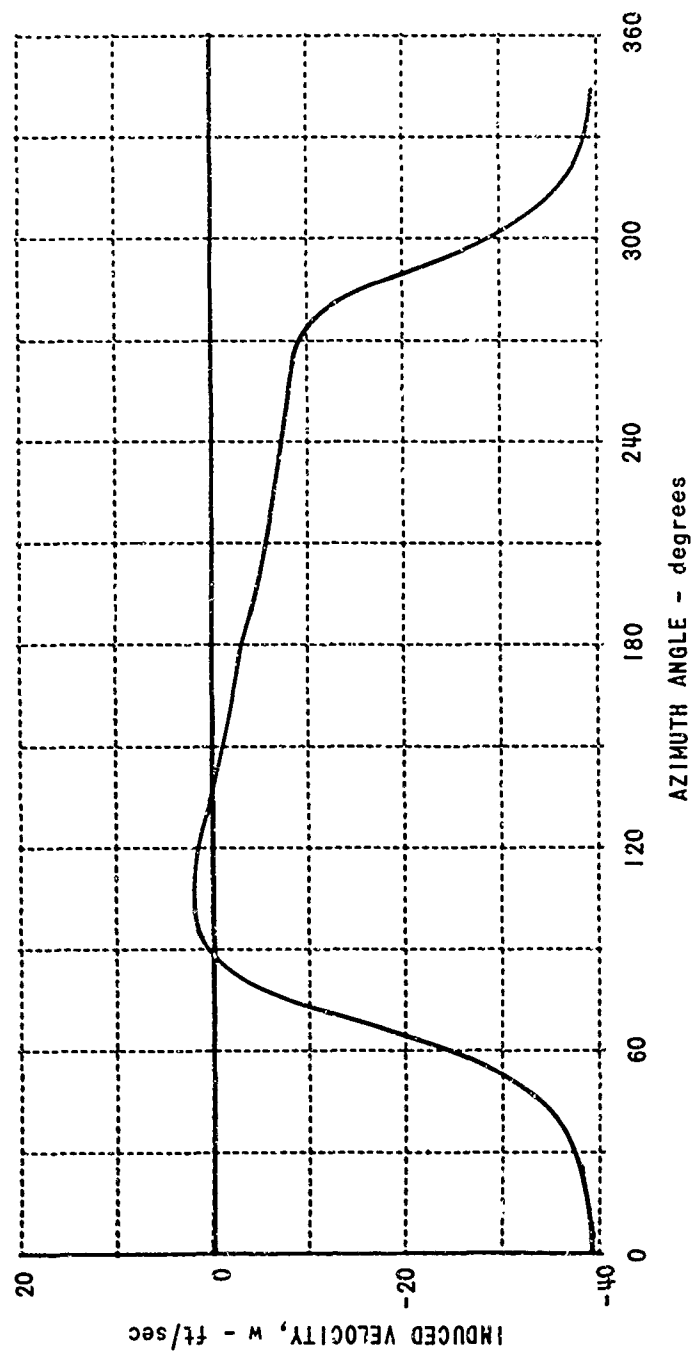


Figure 10b. COMPUTED INDUCED VELOCITY AT $r/R = 0.95$; HU-1A AT $\mu = 0.08$.

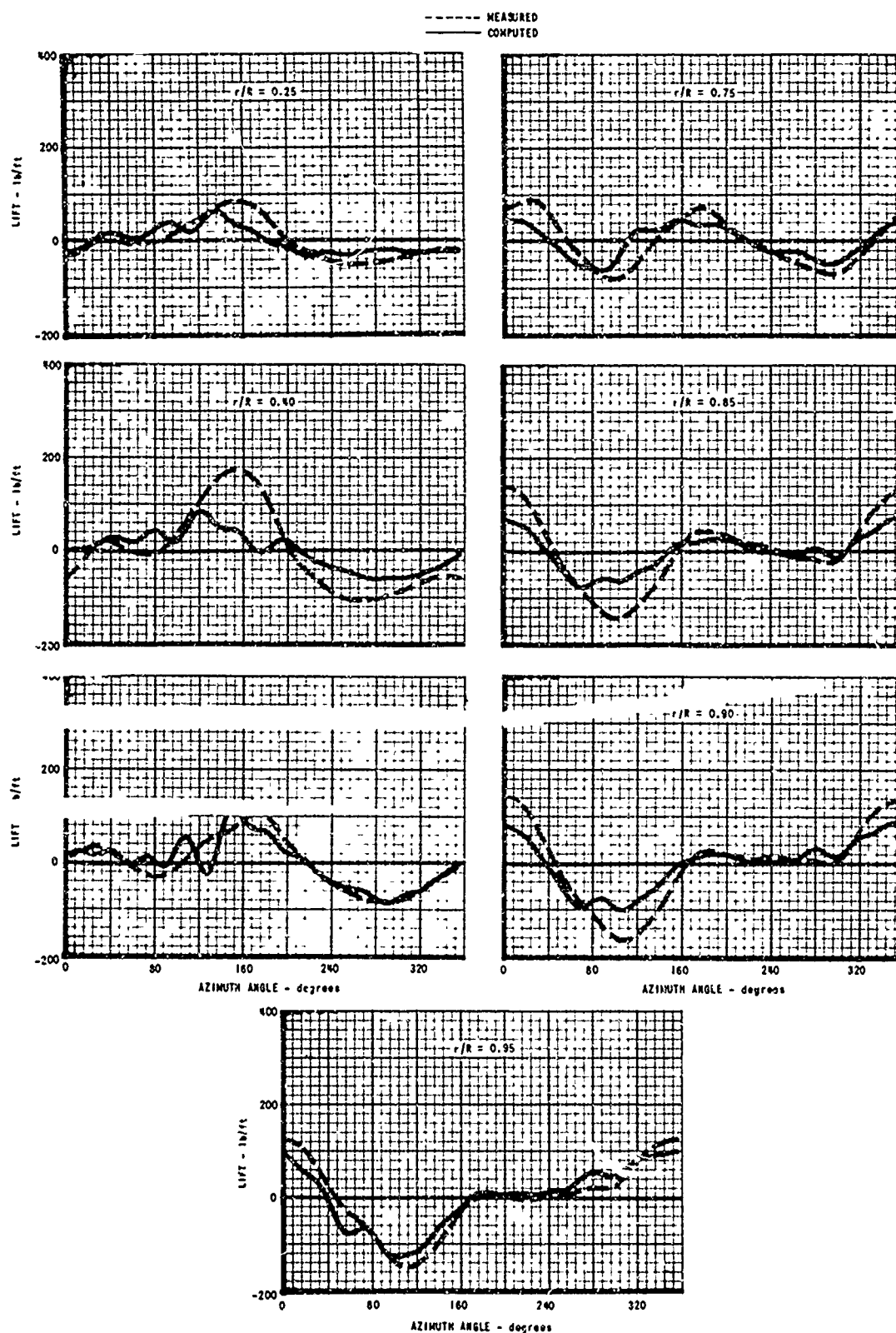
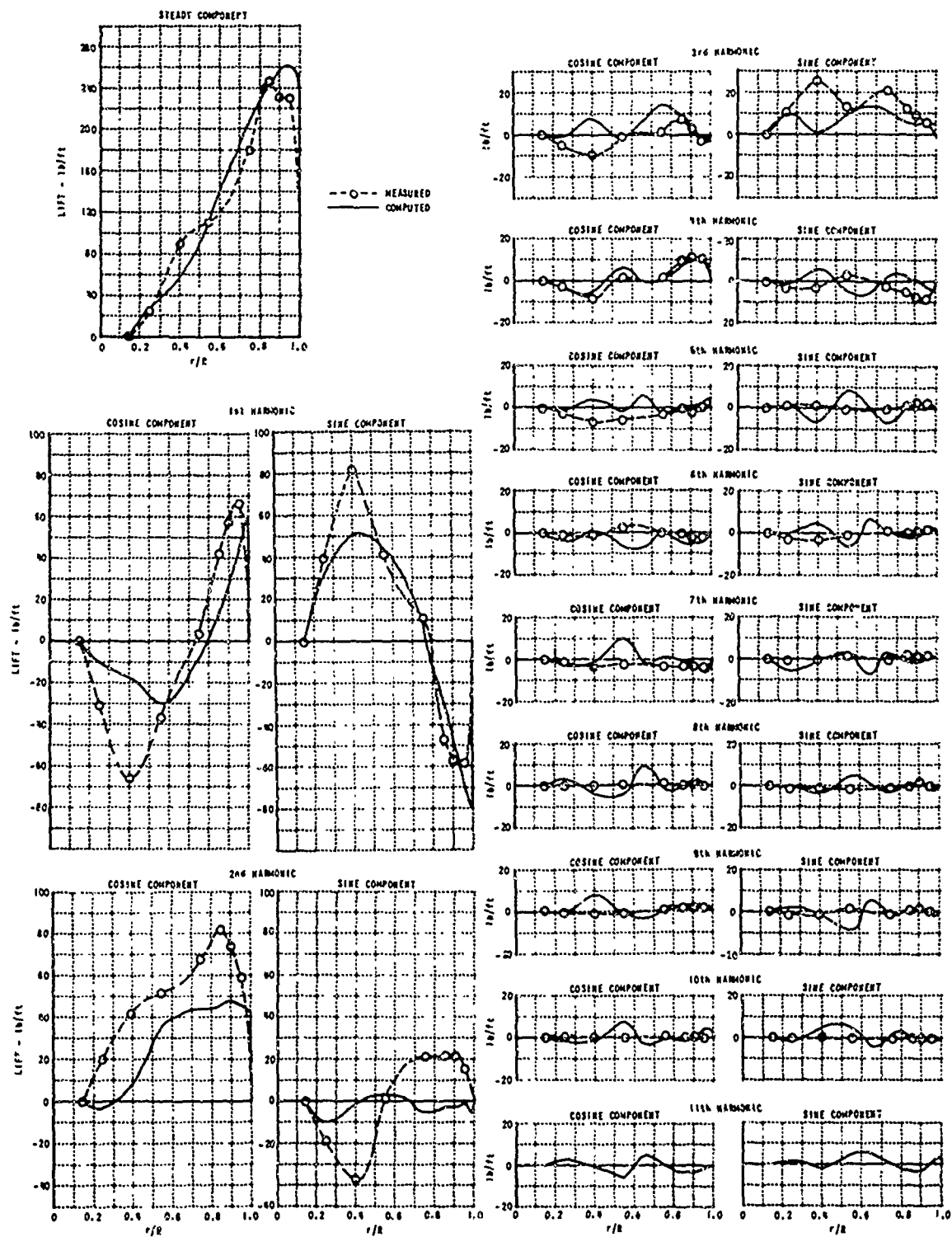
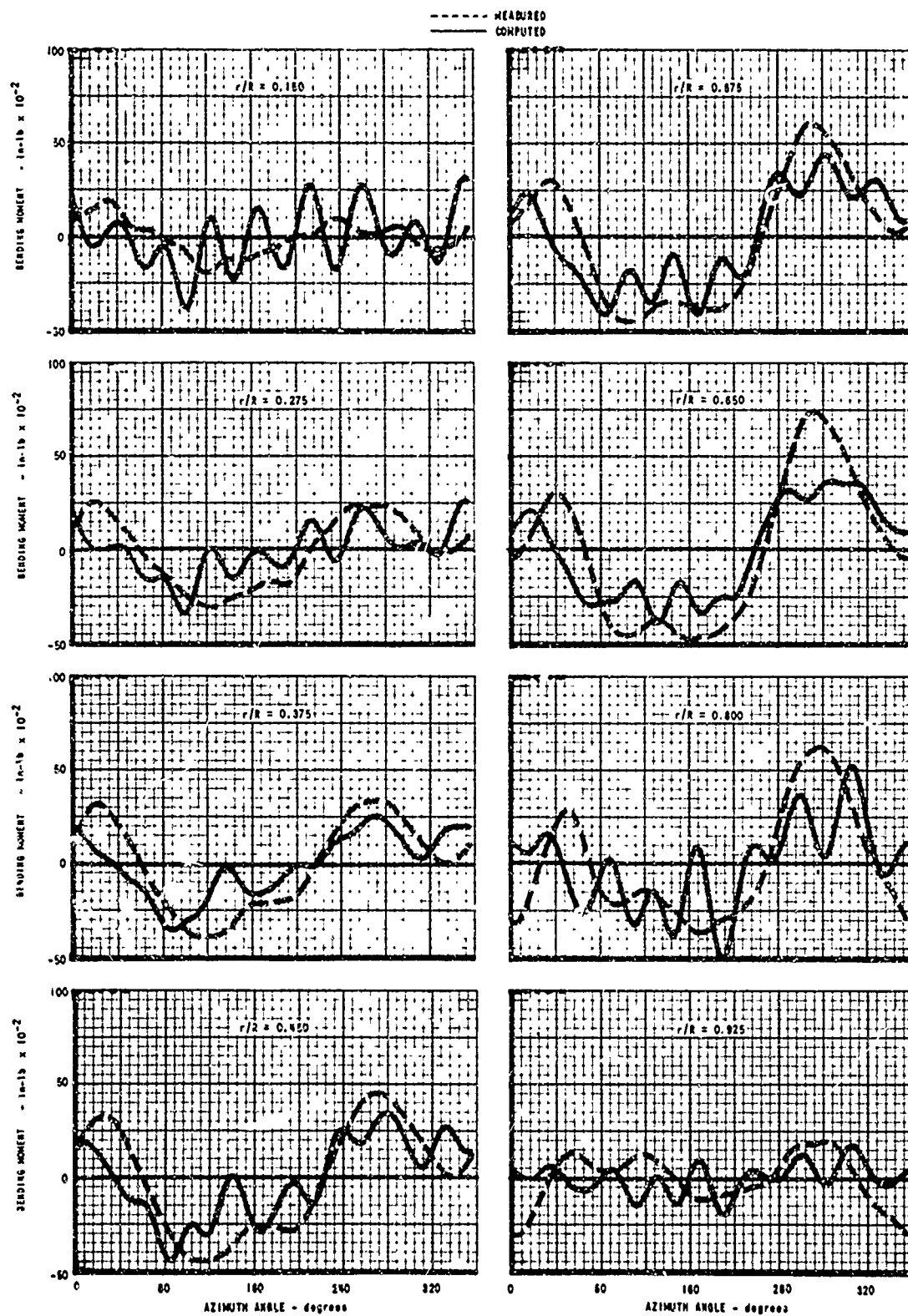


Figure 11. MEASURED AND COMPUTED LIFT AND BENDING MOMENTS;
H-34 AT $\mu_L = 0.29$.



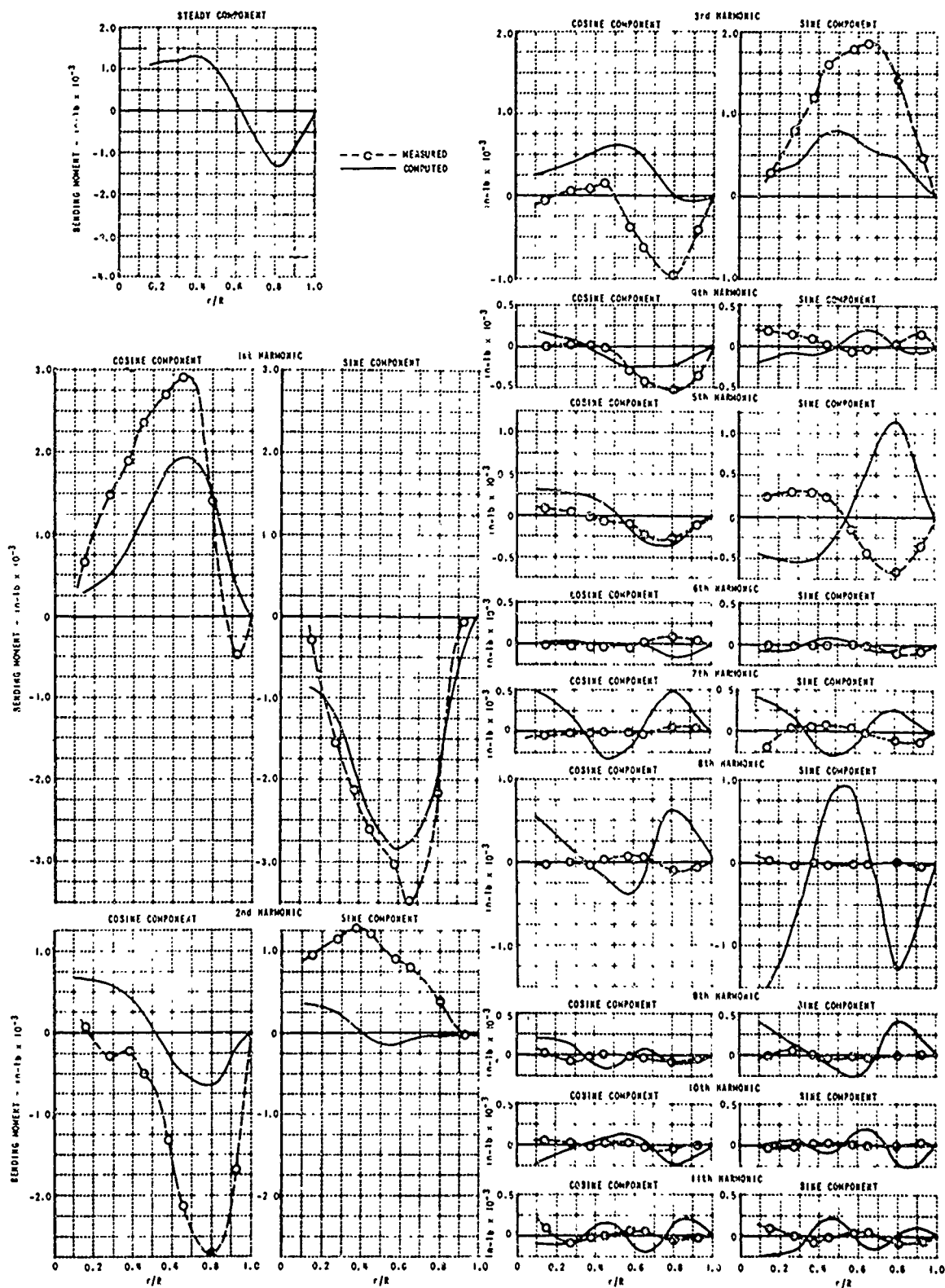
b. HARMONICS OF LIFT

Figure 11 (Cont'd). MEASURED AND COMPUTED LIFT AND BENDING MOMENTS;
H-34 AT $\mu = 0.29$.



c. TIME HISTORIES OF BENDING MOMENTS

Figure II (Cont'd) MEASURED AND COMPUTED LIFT AND BENDING MOMENTS;
H-34 AT $\mu = 0.29$.



d. HARMONICS OF BENDING MOMENTS

Figure 11 (Cont'd). MEASURED AND COMPUTED LIFT AND BENDING MOMENTS;
H-34 AT $\mu = 0.29$.

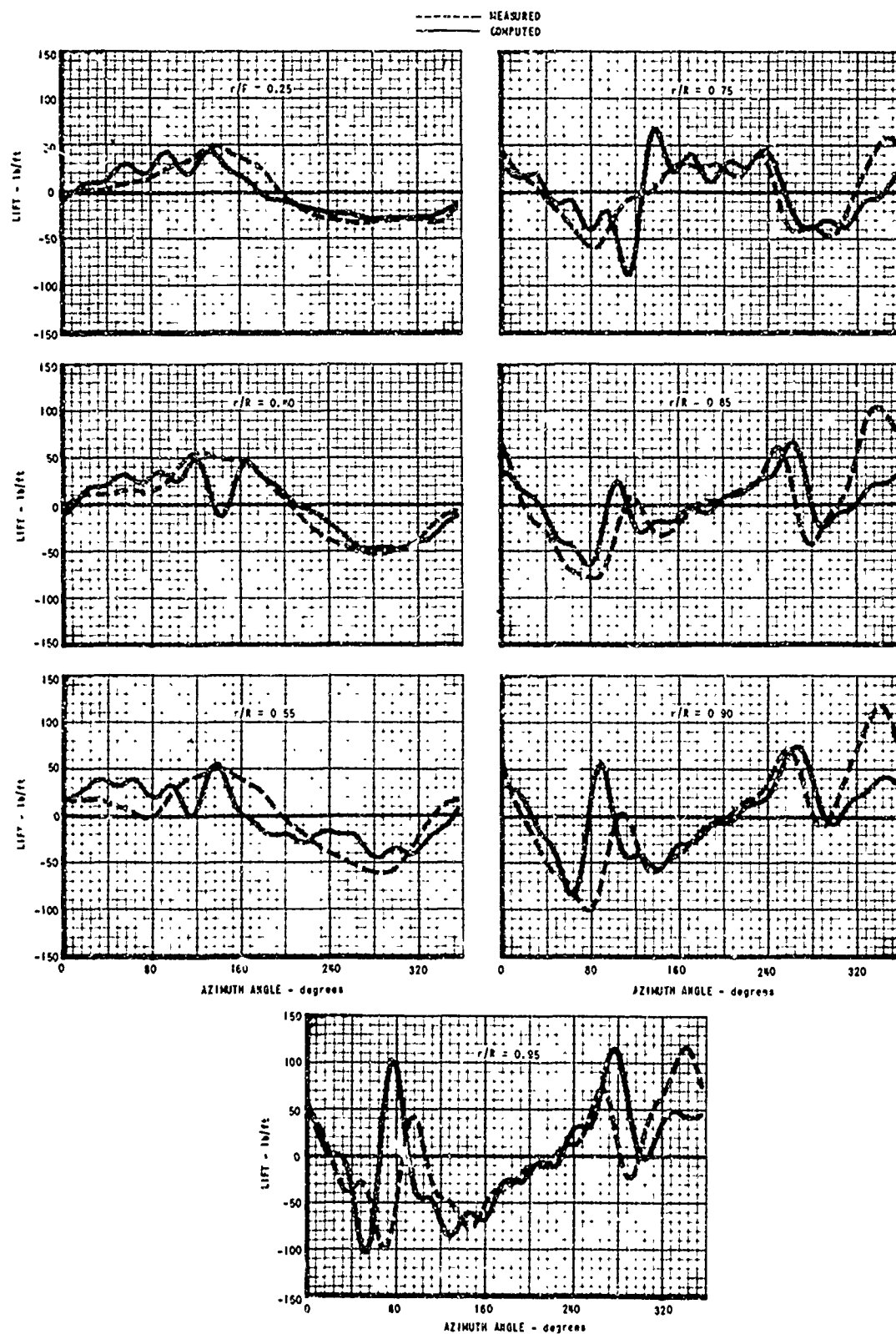
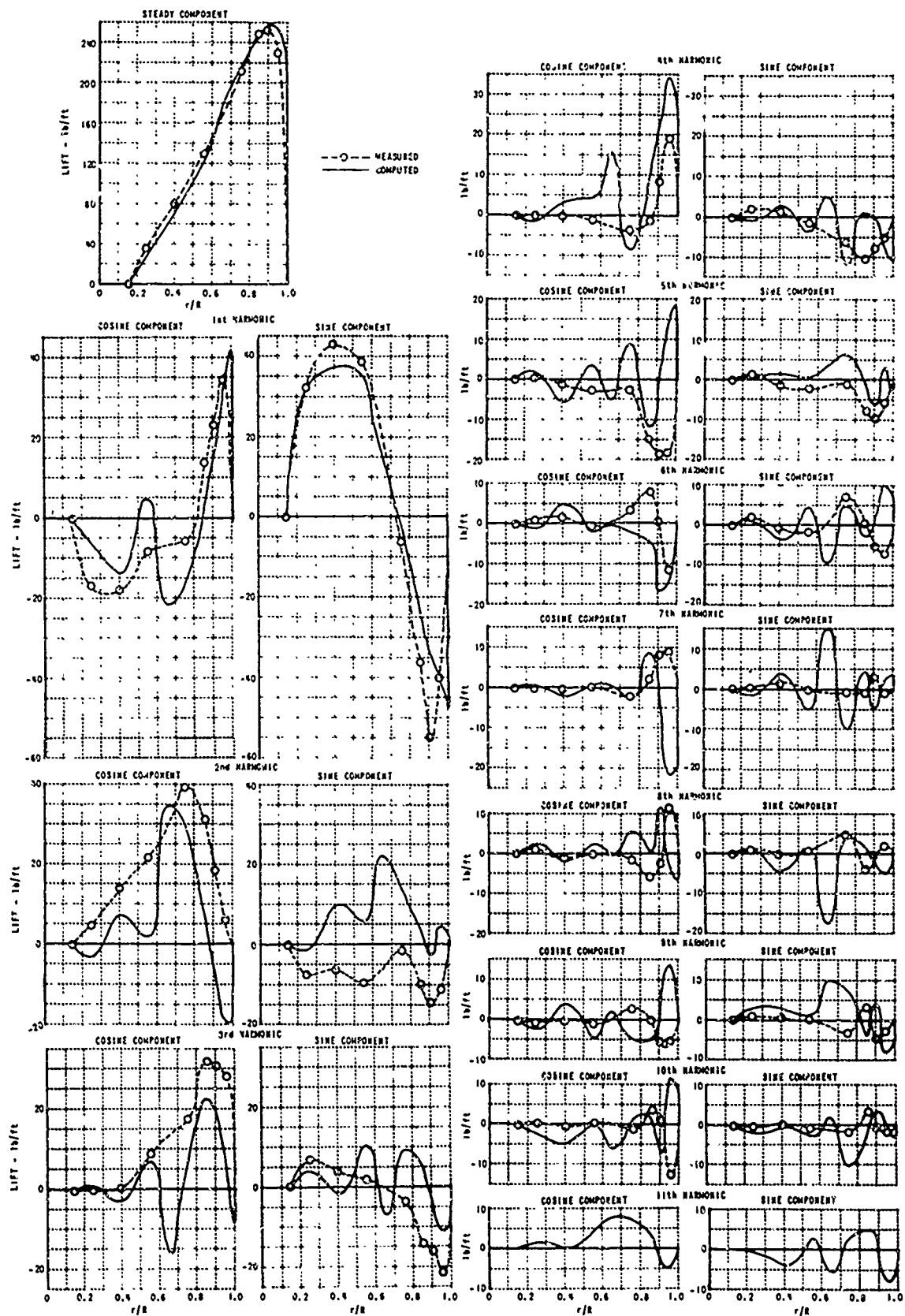
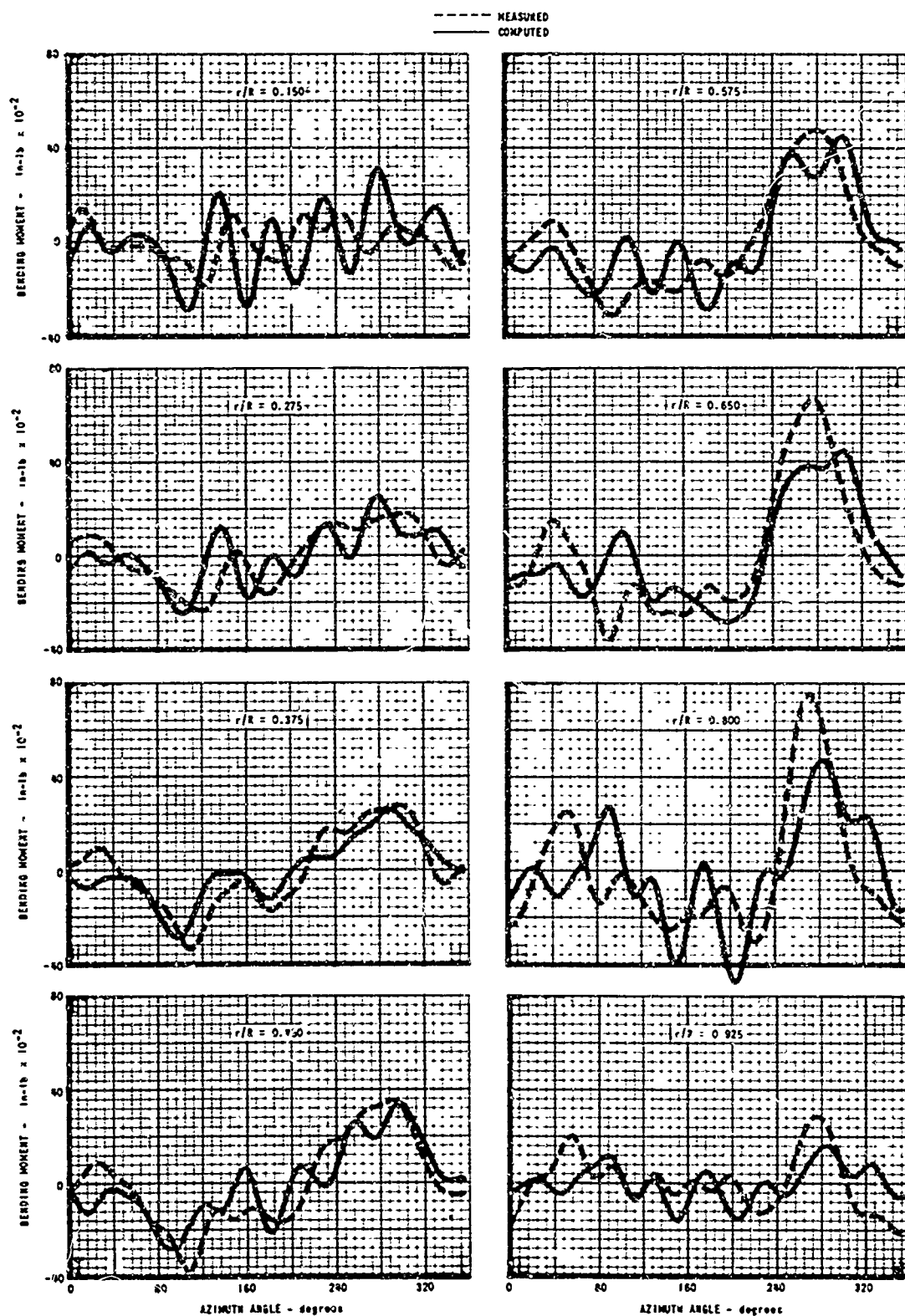


Figure 12. MEASURED AND COMPUTED LIFT AND BENDING MOMENTS:
H-34 AT $\mu = 0.18$.



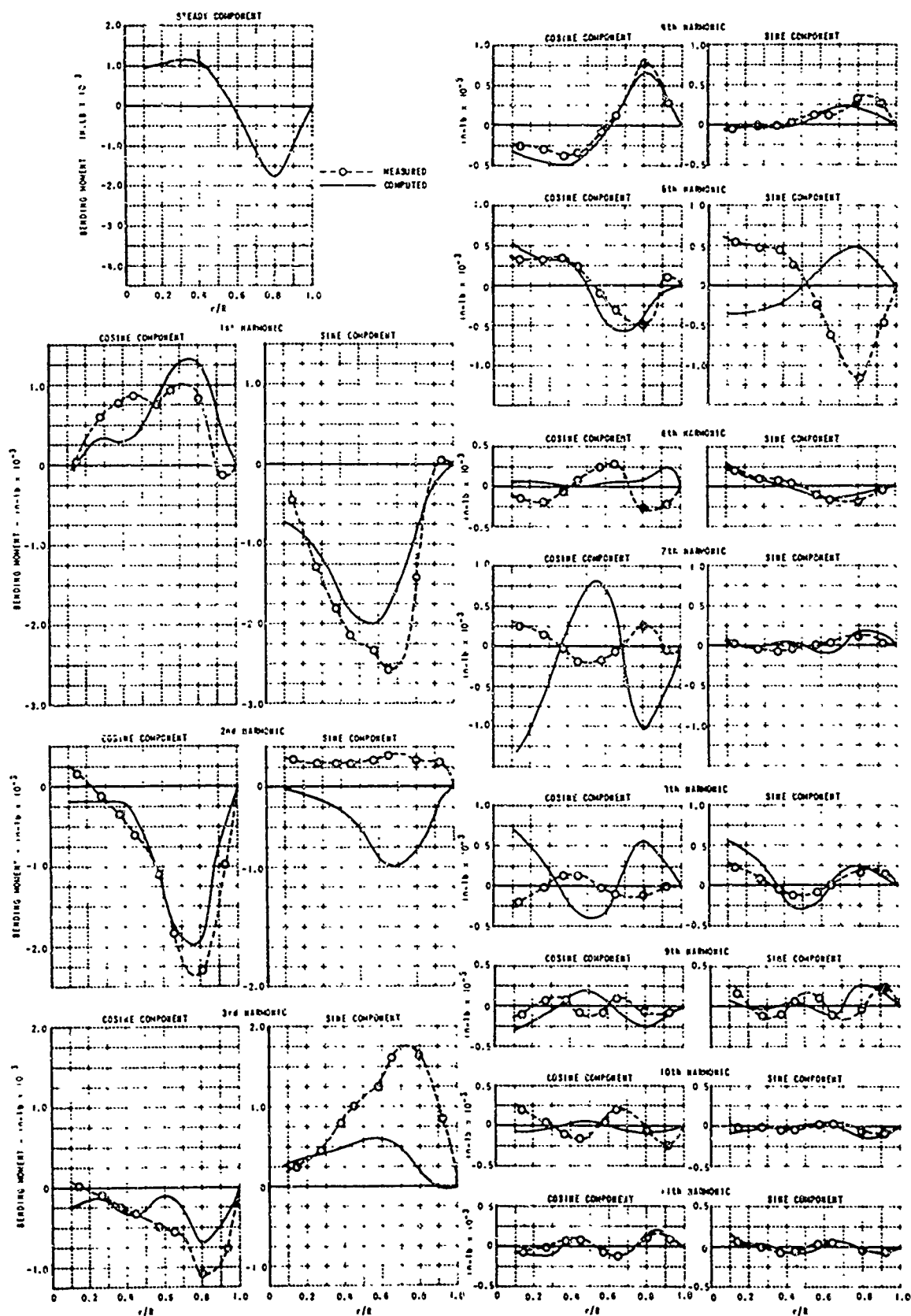
b. HARMONICS OF LIFT

Figure 12 (Cont'd). MEASURED AND COMPUTED LIFT AND BENDING MOMENTS;
H-34 AT $\mu = 0.18$.



c. TIME HISTORIES OF BENDING MOMENTS

Figure 12 (Cont'd) MEASURED AND COMPUTED LIFT AND BENDING MOMENTS;
H-34 AT $\mu = 0.18$.



d. HARMONICS OF BENDING MOMENTS

Figure 12 (Cont'd) MEASURED AND COMPUTED LIFT AND BENDING MOMENTS;
H-34 AT $\mu = 0.18$.

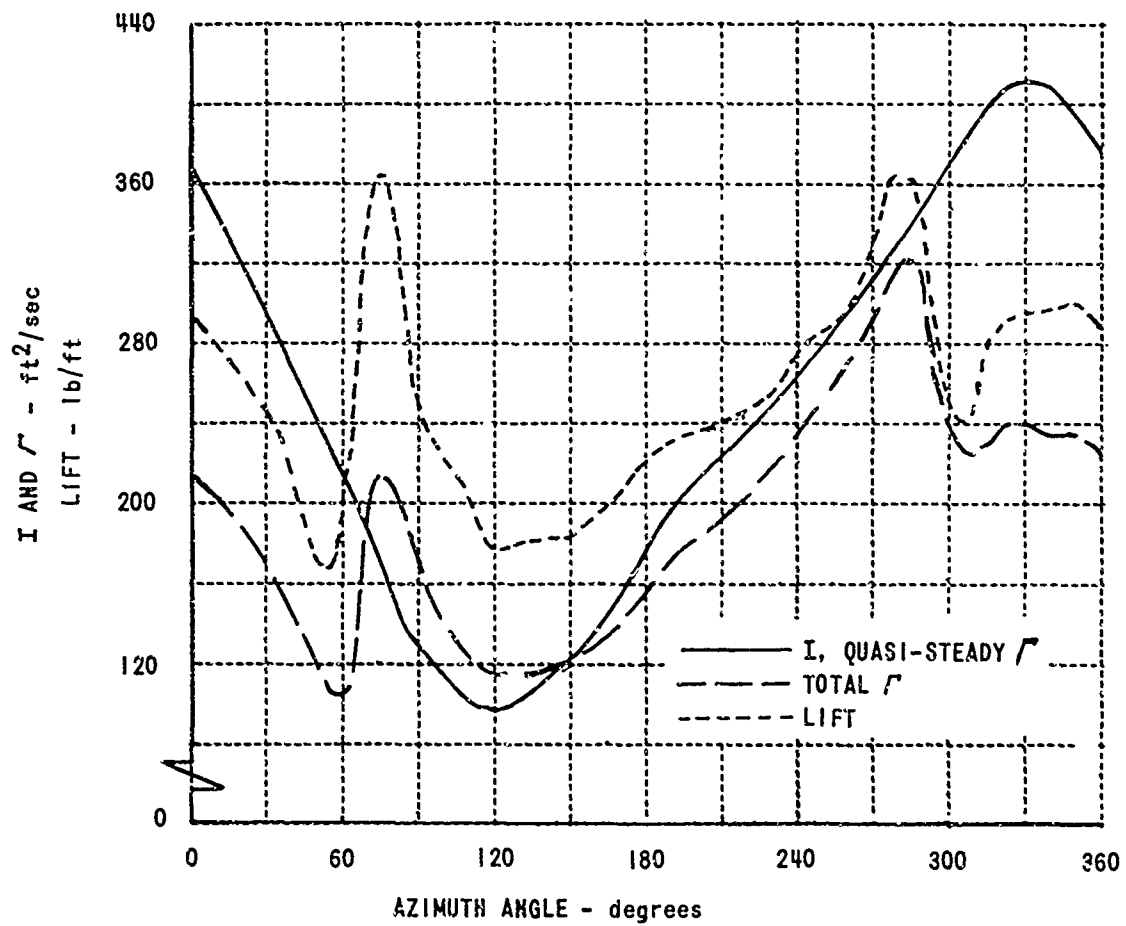


Figure 13a. COMPUTED QUASI-STEADY Γ , TOTAL Γ , AND LIFT AT $r/R = 0.95$; H-34 AT $\mu = 0.18$.

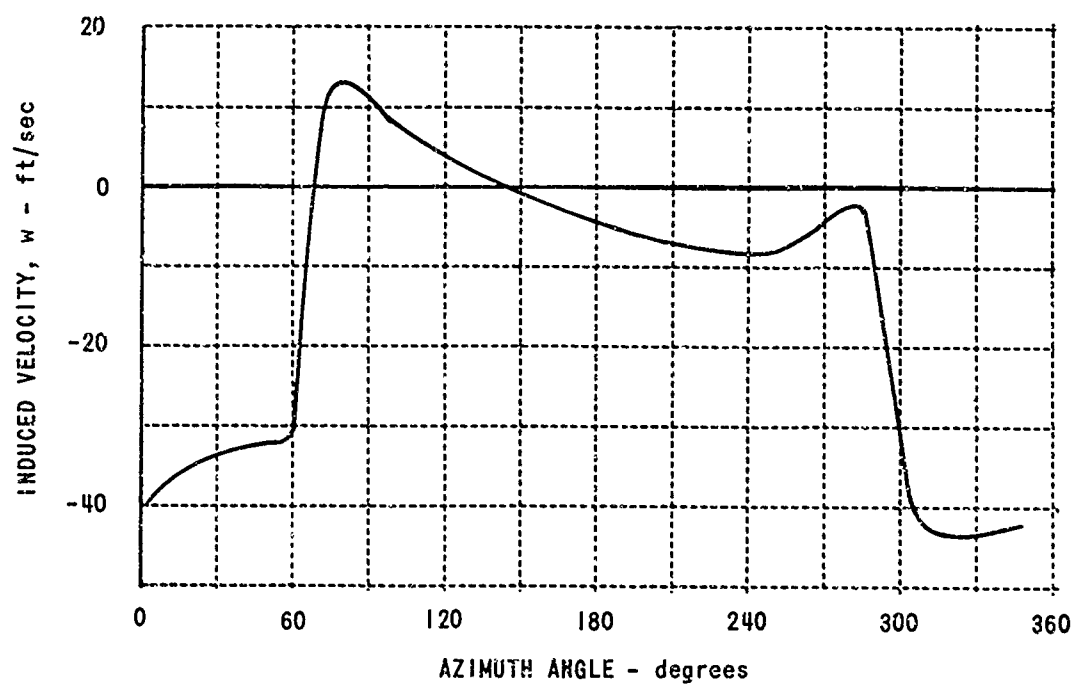


Figure 13b. COMPUTED INDUCED VELOCITY AT $r/R = 0.95$; H-34 AT $\mu = 0.18$.

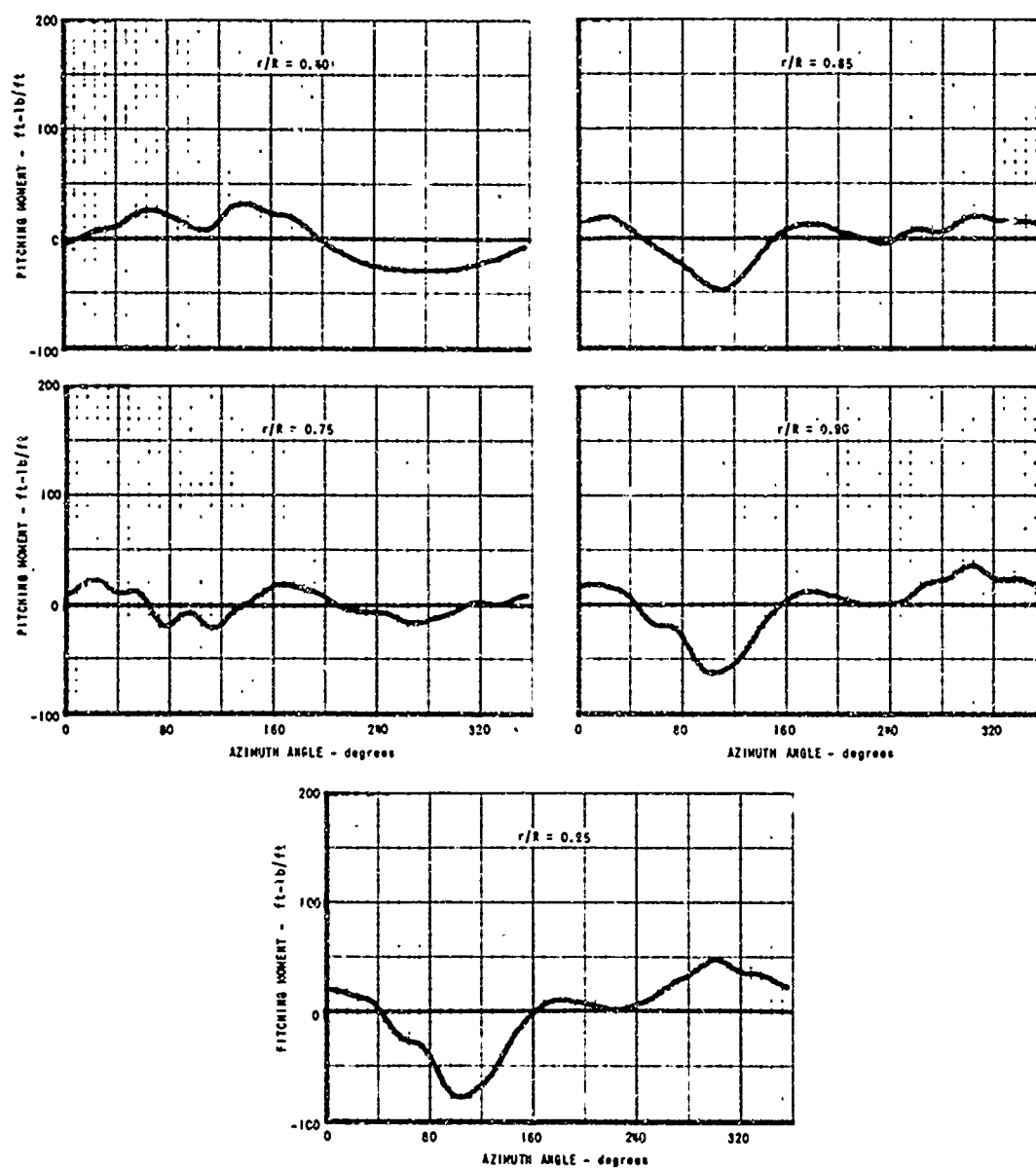


Figure 14a. COMPUTED PITCHING MOMENTS; HU-1A AT $\mu = 0.26$.

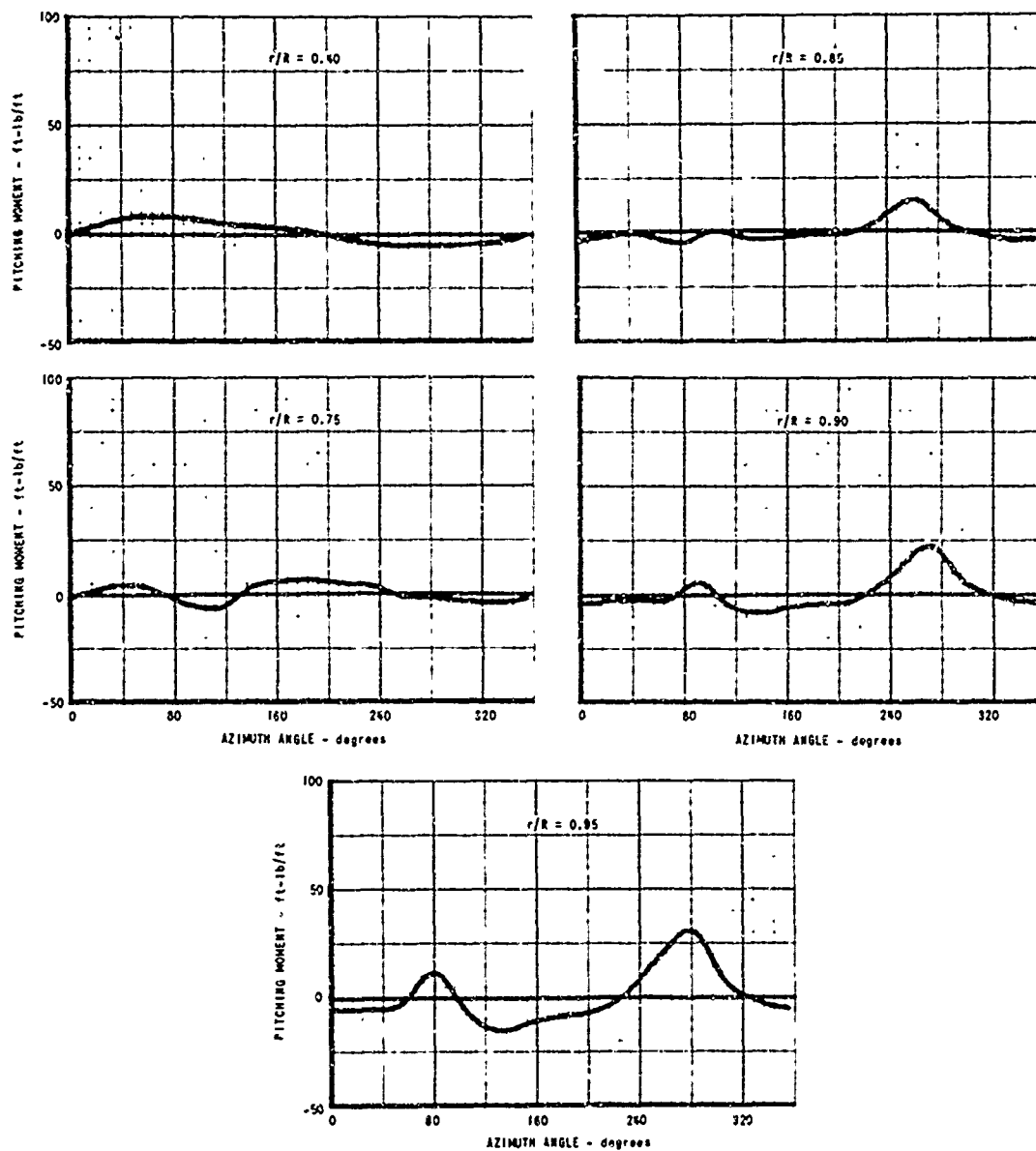


Figure 14b. COMPUTED PITCHING MOMENTS; HU-1A AT $\mu = 0.08$.

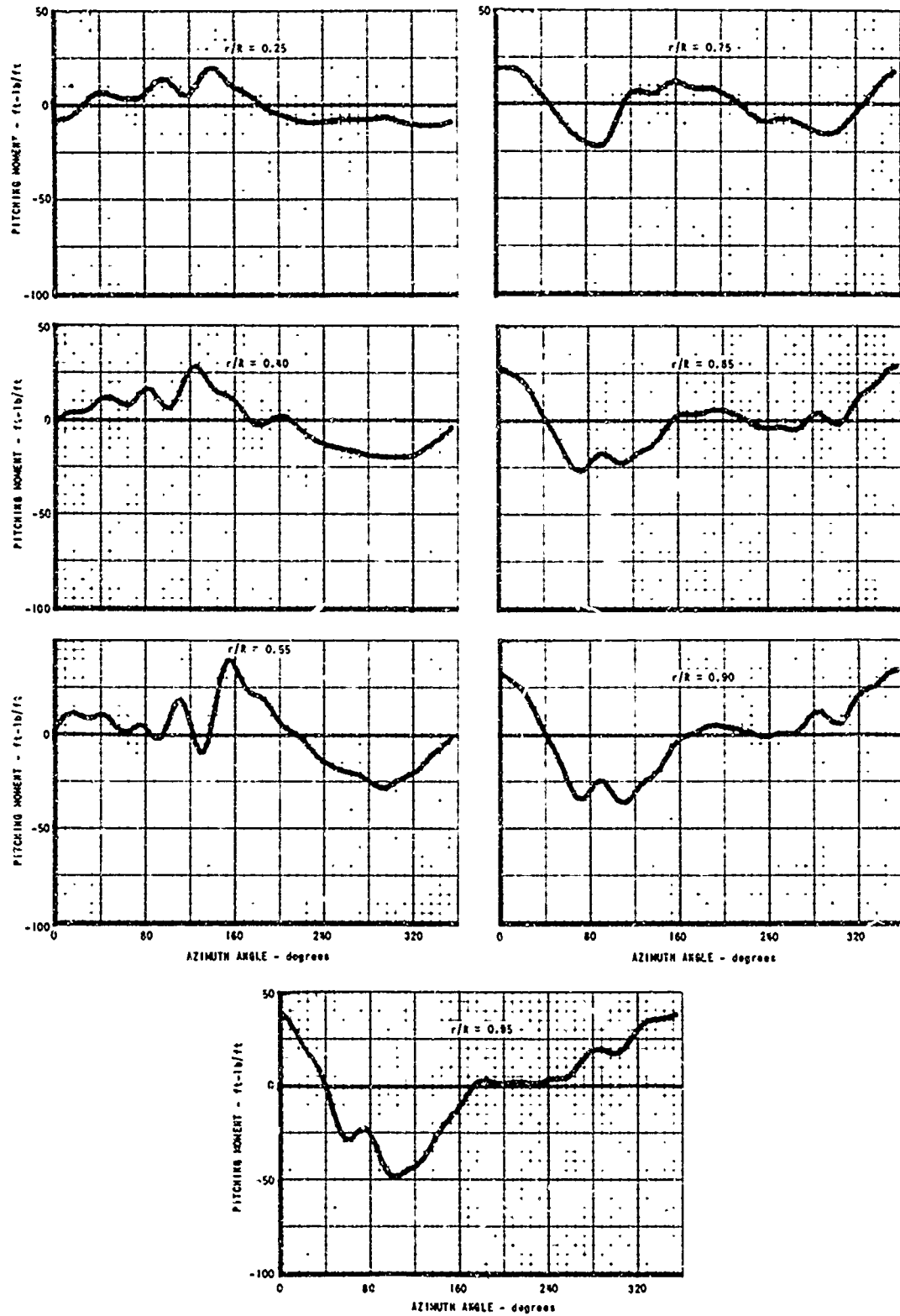


Figure 14c. COMPUTED PITCHING MOMENTS; H-34 AT $\mu = 0.29$.

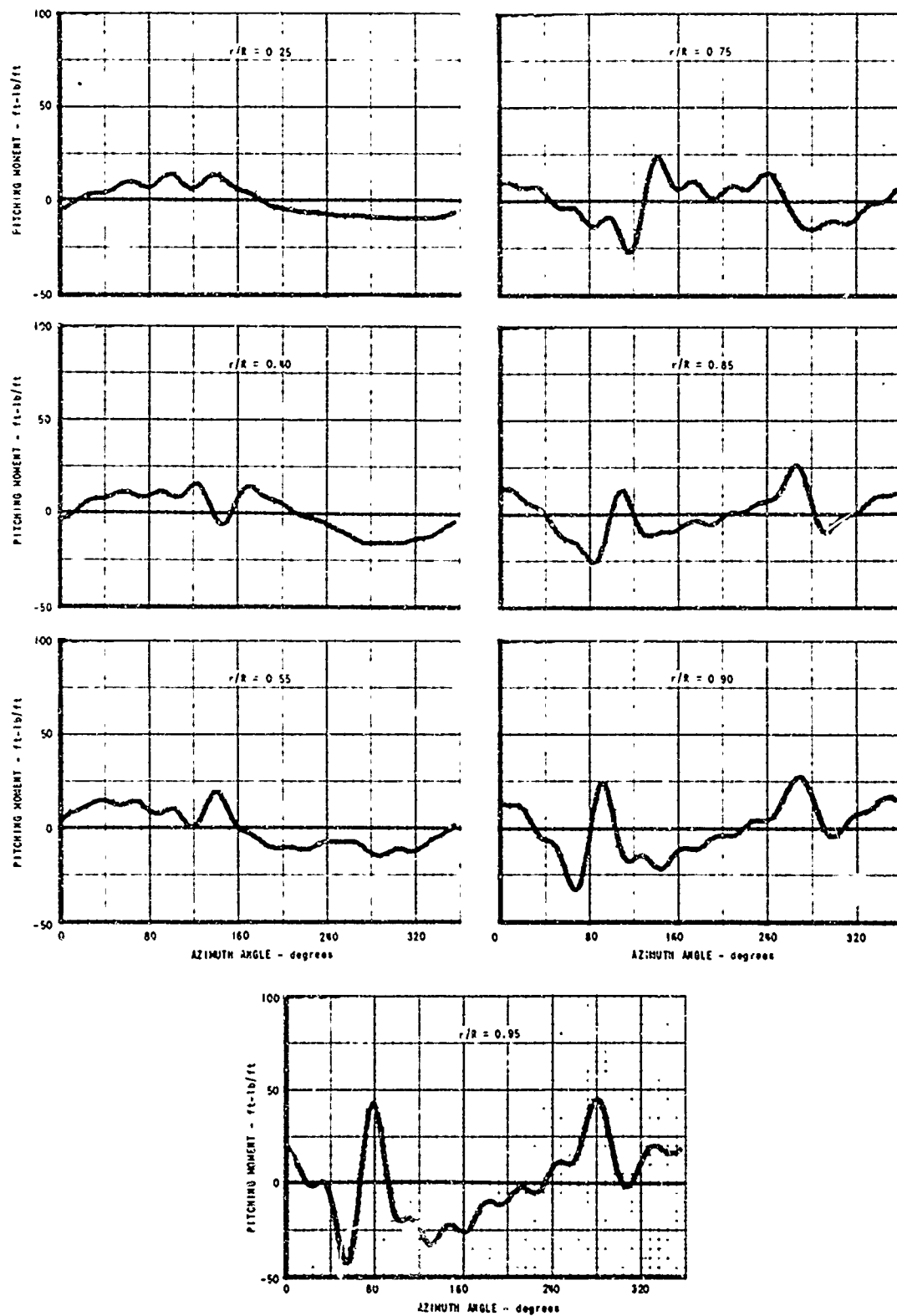
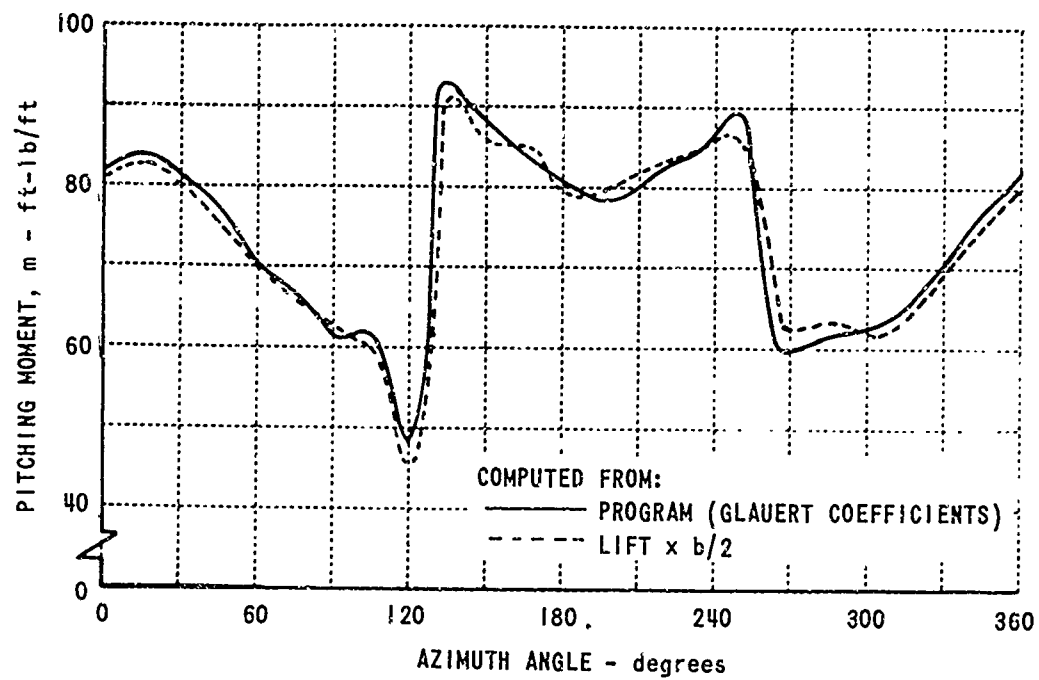
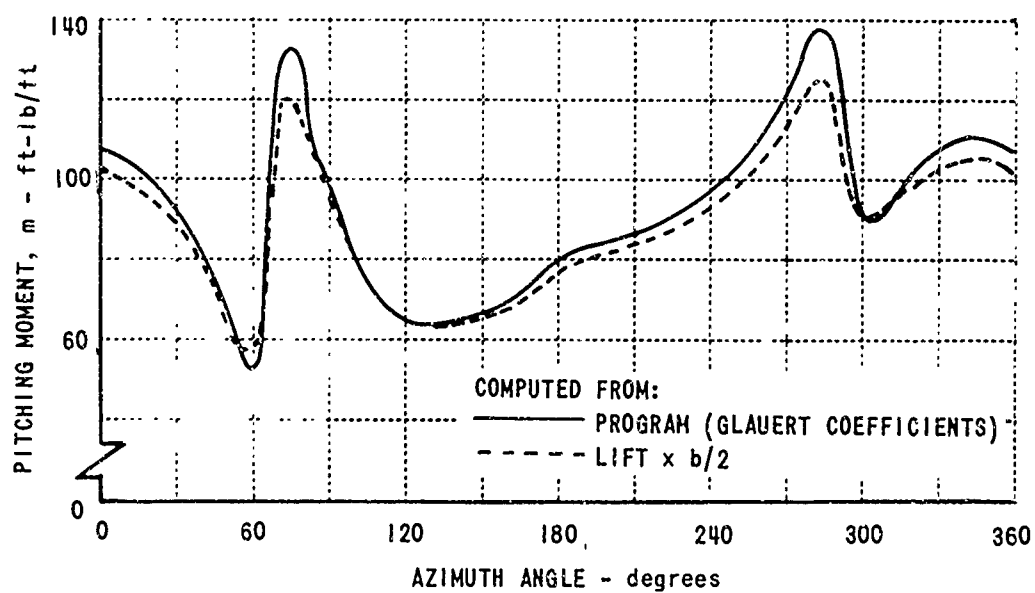


Figure 14d. COMPUTED PITCHING MOMENTS; H-34 AT $\mu = 0.18$.



a. $r/R = 0.75$



b. $r/R = 0.95$

Figure 15. COMPUTED PITCHING MOMENTS ABOUT MID-CHORD; H-34 AT $\mu = 0.18$.

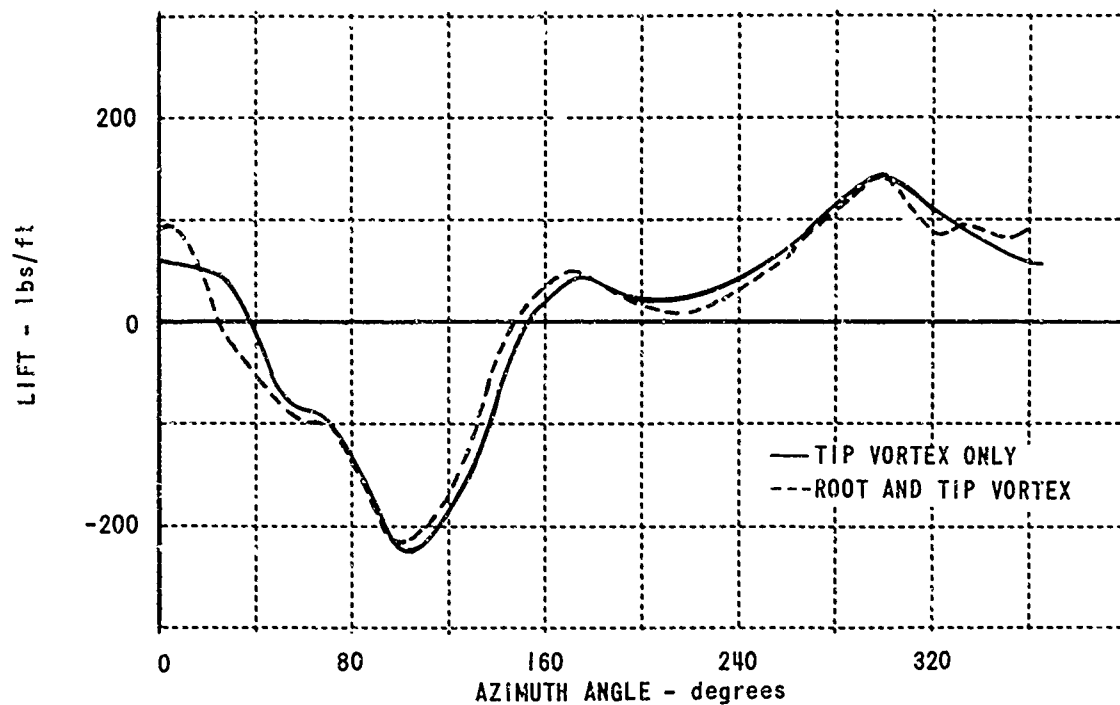


Figure 16a. COMPARISON OF COMPUTED LIFT AT $r/R = 0.95$ FOR WAKE WITH AND WITHOUT A CONCENTRATED ROOT TRAILING VORTEX, HU-1A AT $\mu = 0.26$.

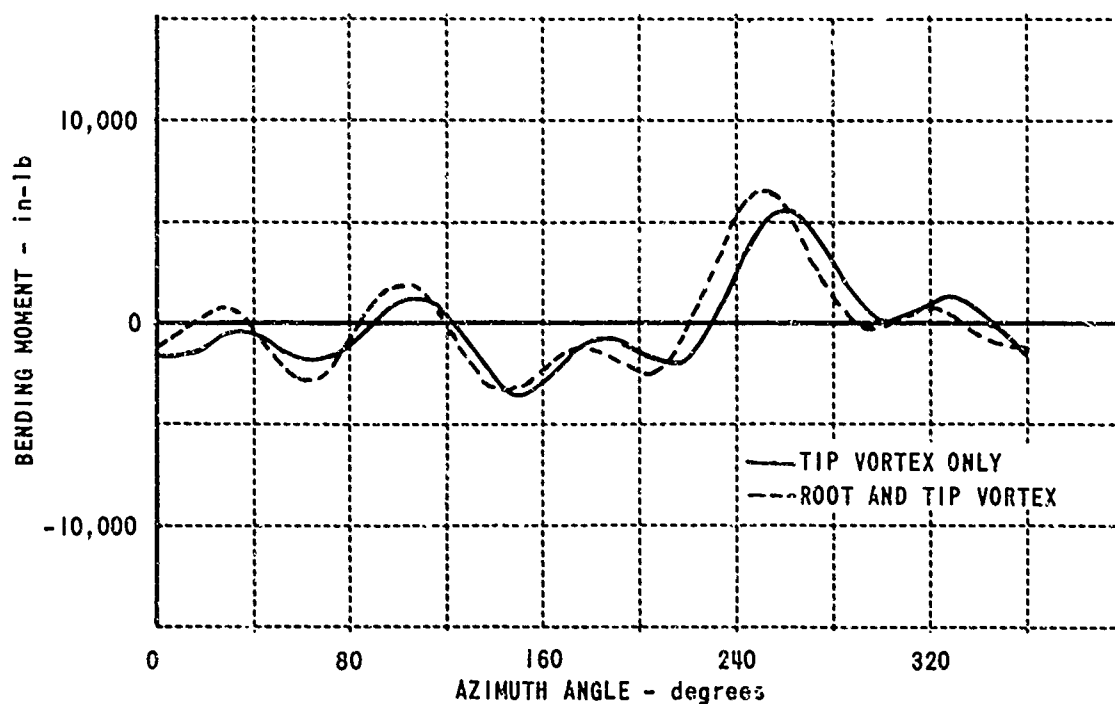


Figure 16b. COMPARISON OF COMPUTED BENDING MOMENT AT $r/R = 0.21$ WITH AND WITHOUT A CONCENTRATED ROOT TRAILING VORTEX, HU-1A AT $\mu = 0.26$.

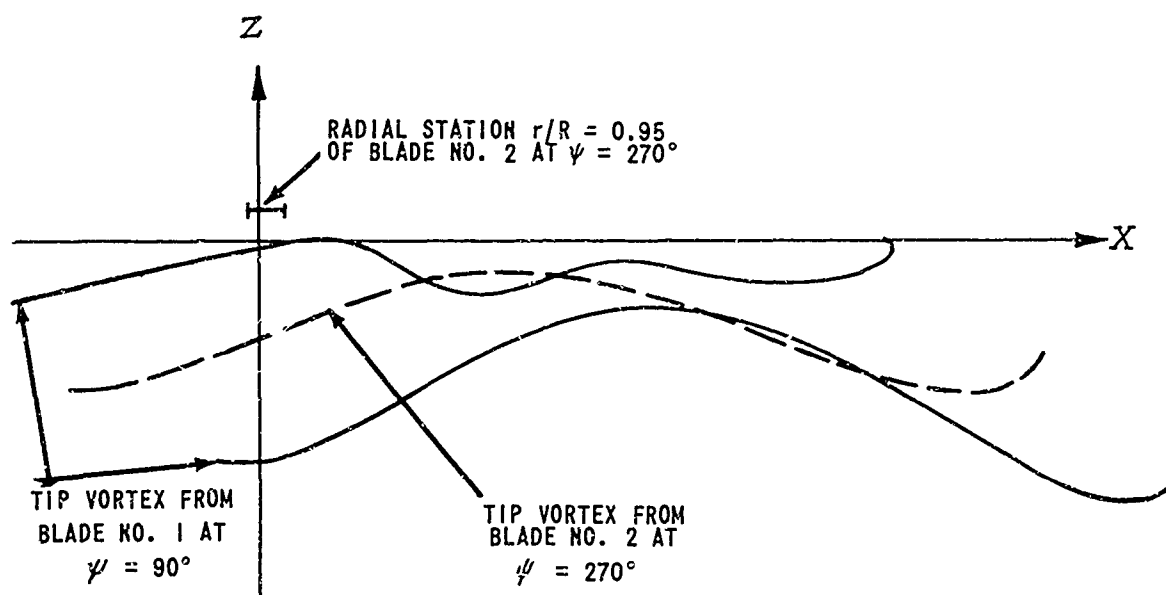


Figure 17. DISTORTED TIP VORTICES ON RETREATING SIDE OF ROTOR DISK AS USED IN COMPUTATION, BLADES IN THE $\psi = 90^\circ$ AND 270° POSITIONS; HU-1A AT $\mu = 0.08$.

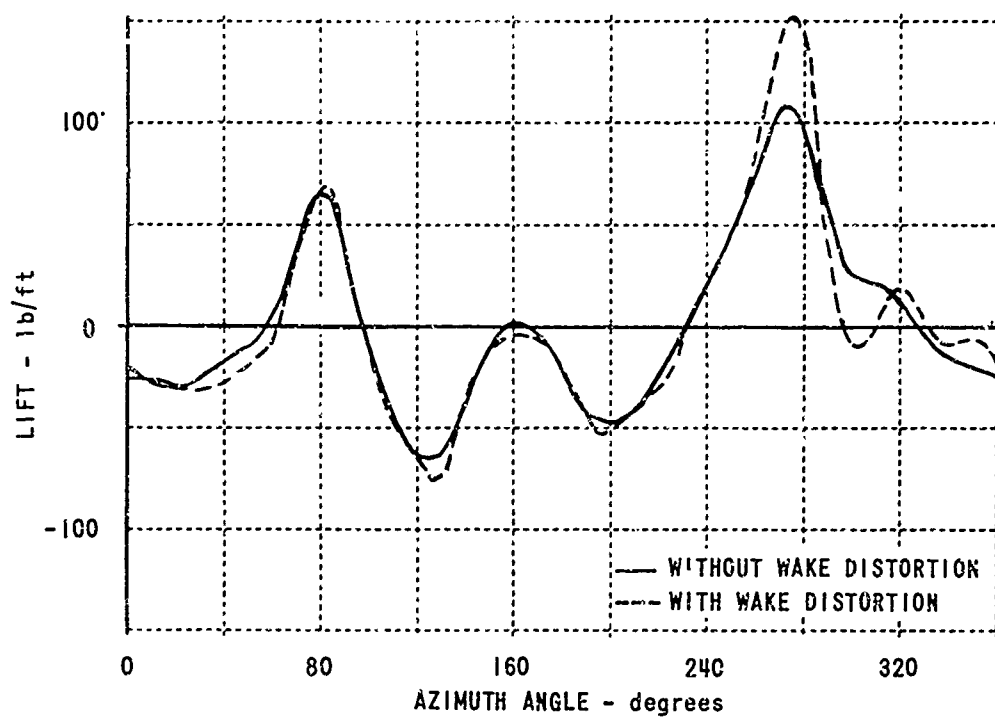


Figure 18. COMPARISON OF LIFT AT $r/R = 0.95$ COMPUTED WITH AND WITHOUT WAKE DISTORTION, HU-1A AT $\mu = 0.08$.

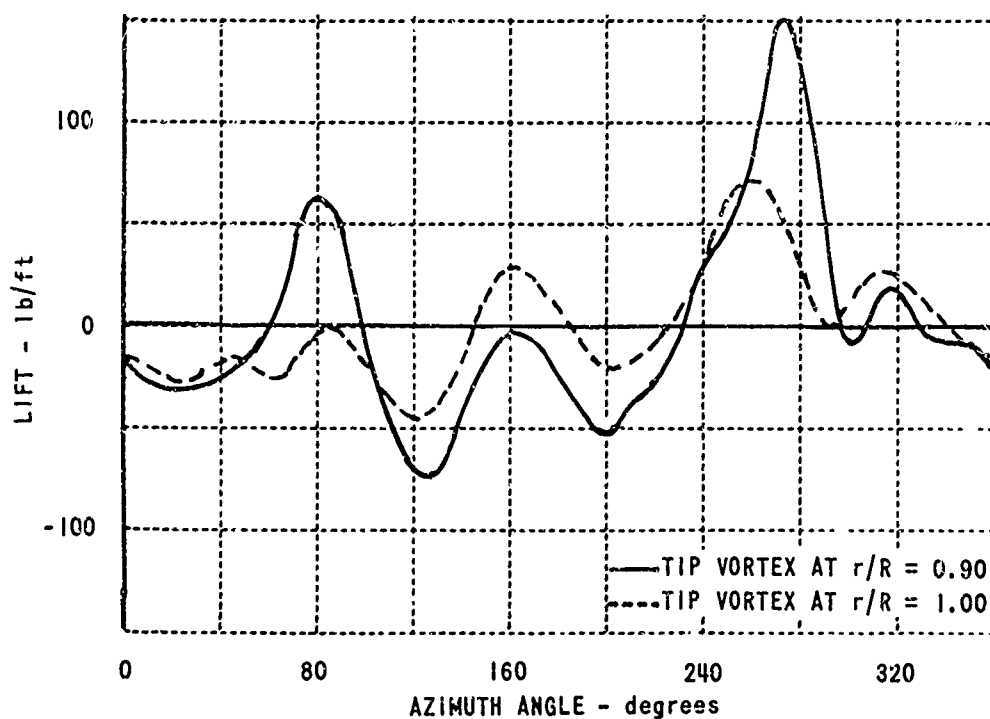


Figure 19. COMPARISON OF LIFT AT $r/R = 0.95$ COMPUTED FOR TWO POSITIONS OF THE TIP VORTEX IN THE WAKE, HU-1A AT $\mu = 0.08$.

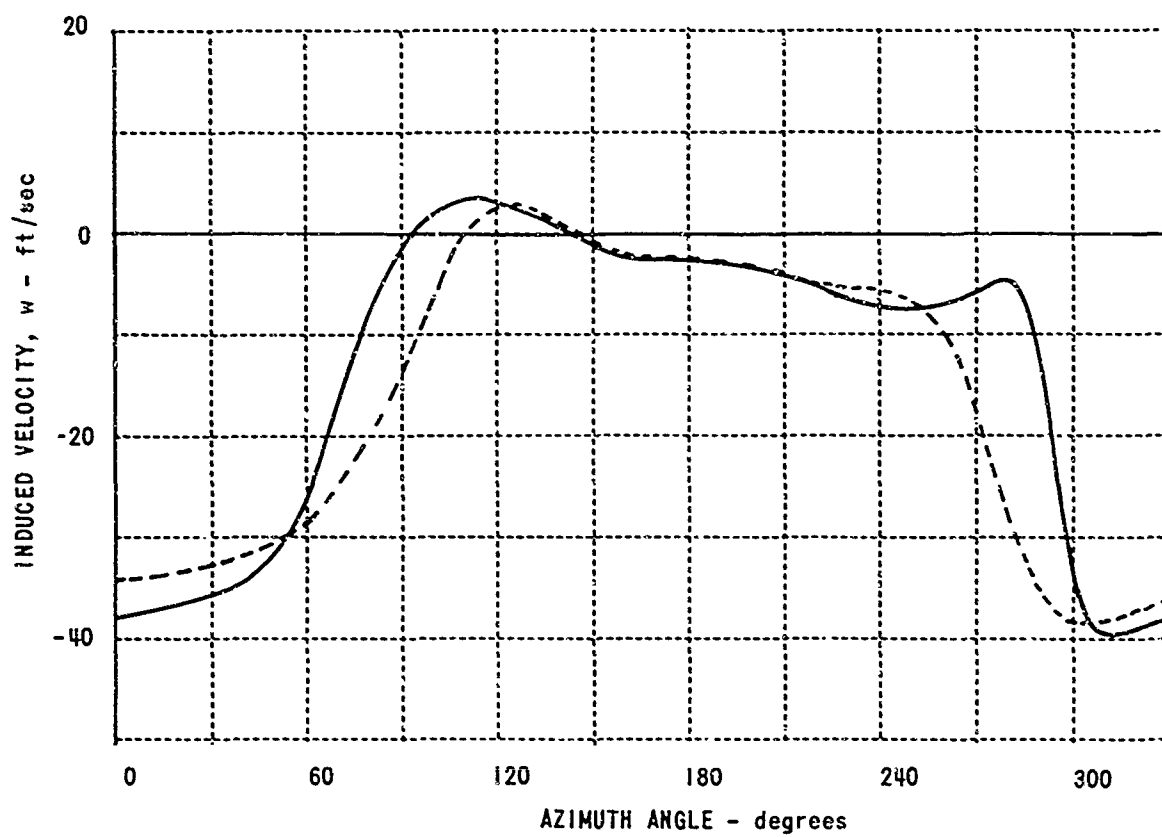


Figure 20. COMPARISON OF THE INDUCED VELOCITY AT $r/R = 0.95$ FOR TWO RADIAL POSITIONS OF THE TIP VORTEX IN THE WAKE; HU-1A AT $\mu = 0.08$.

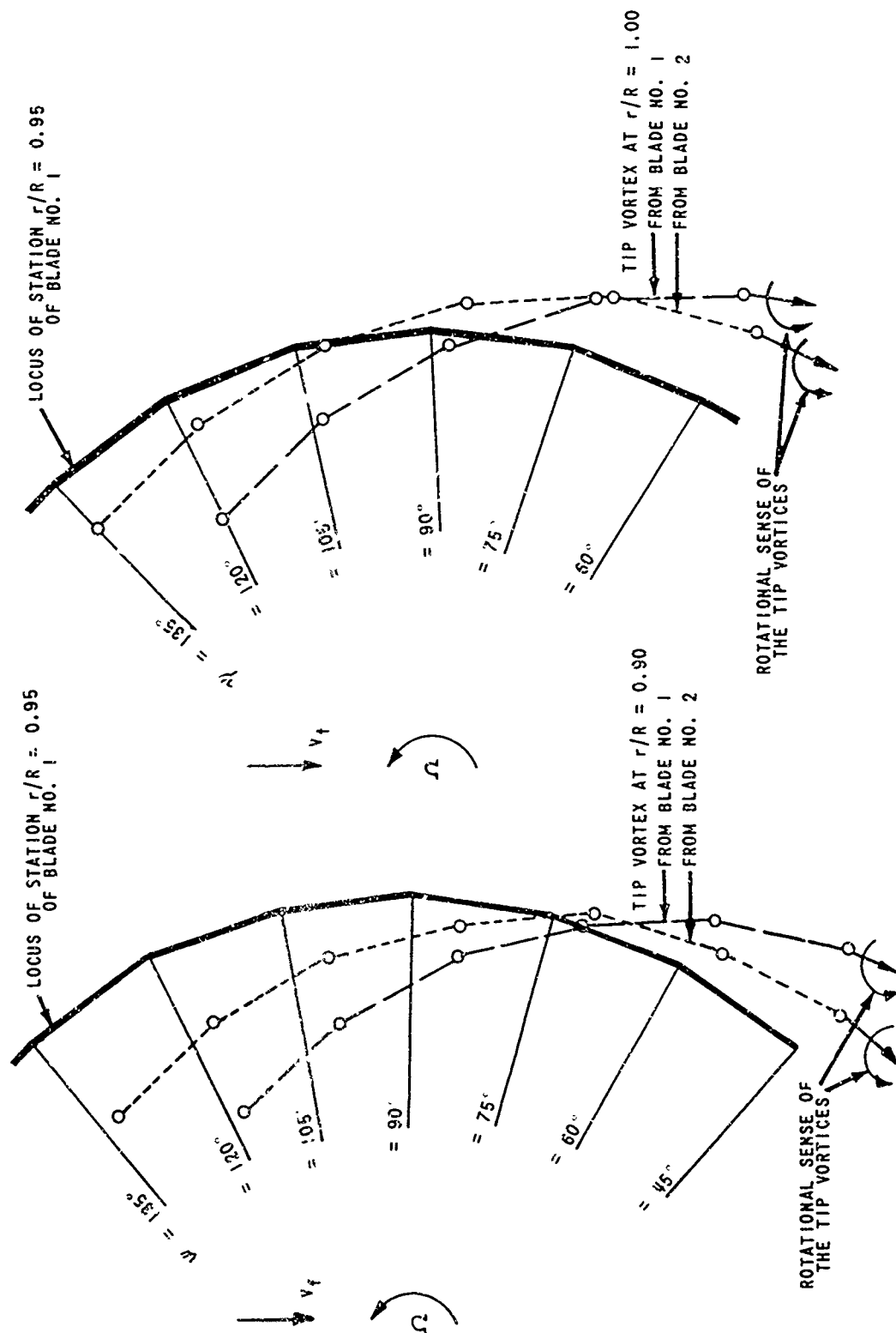


Figure 21. RELATIVE ORIENTATION OF THE BLADE AND RECENT TIP VORTICES ON ADVANCING SIDE OF THE DISK, HU-1A AT $\mu = 0.08$.

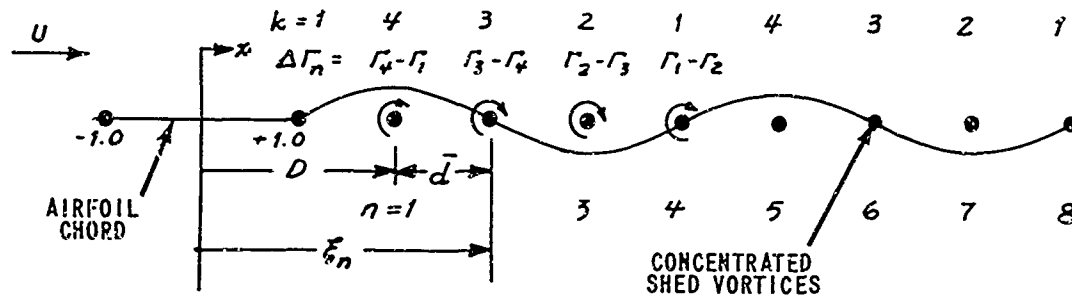
APPENDIX I

TWO-DIMENSIONAL OSCILLATING WING INVESTIGATION

OF WAKE SHED VORTEX REPRESENTATION

A numerical computational procedure was developed and programmed for computing the lift and pitching moments experienced by a two-dimensional oscillating wing whose shed wake was represented by equally spaced concentrated vortices. This procedure is parallel to that developed and used to represent the rotor blade and described under the section Blade Representation. For this problem, however, the integrals for the cosine components of chordwise induced velocity distribution due each wake vortex element can be evaluated in closed form. The procedure is outlined below, and the results of the investigation are presented and discussed.

The notation to be used is illustrated in the following diagram



The airfoil chord is centered on the x -axis with the leading and trailing edges at $x = -1$ and $x = +1$ respectively. The airfoil shed vorticity is represented by a distribution of concentrated equally spaced two-dimensional vortices and the nondimensional spacing given by

$$\bar{d} = \frac{2\pi U}{X b \omega} \quad (\text{half-chords traveled per shed vortex}) \quad (I-1)$$

where

U = freestream velocity

b = airfoil semichord

ω = frequency of airfoil oscillations

\bar{X} = number of shed vortices per cycle of the airfoil motion used in the wake representation

The nondimensional distance, D , from the midchord to the first shed vortex was taken to be independent of \bar{d} . When $D = 1 + \bar{d}$, the first shed vortex is behind the trailing edge a distance equal to the wake spacing and conceptually the vortices are being released from the trailing edge for the airfoil in each position, k , of its oscillation. When $D < 1 + \bar{d}$, the wake is considered to be advanced with respect to the airfoil. The distance of each shed vortex from the midchord is

$$\xi_n = (n-1)\bar{d} + D \quad (I-2)$$

and n is the relative position number of the vortex behind the trailing edge. The airfoil position number, k , is a label to indicate the relative position of the airfoil in its cycle of oscillation ($k = 1$ is the beginning of the oscillation and there are \bar{X} positions). The values of the airfoil bound vorticity, Γ_k , at each position in the cycle of oscillation are the unknowns and because of the periodicity of the problem they repeat at corresponding position numbers; there are thus \bar{X} unknown values of Γ_k . The strengths of the shed vortices and their positive sense are indicated in the diagram for the first few vortices behind the airfoil as the difference in strength of the bound vorticity between successive airfoil positions.

The chordwise aerodynamic boundary condition on the airfoil is expressed by the following integral equation,

$$(-h + U\alpha + x b \dot{\alpha}) + \sum_{n=1}^{N\bar{X}} \frac{\Delta \Gamma_n}{2\pi(\xi_n - x)b} - \frac{1}{2\pi} \int_{-1}^{+1} \frac{\gamma(\bar{x}) d\bar{x}}{(x - \bar{x})} = 0 \quad (I-3)$$

where N is the number of cycles of wake representation retained and h , α , and $\dot{\alpha}$ are the blade input oscillation in plunge and pitch. By letting $x = -\cos \theta$ and expanding the bound vorticity distribution in a Glauert series

$$\gamma(\theta) = 2(A_0 \cot \frac{\theta}{2} + \sum_{n=1}^{\infty} A_n \sin n\theta), \quad (I-4)$$

the integral of (I-3) can be evaluated as the following cosine series:

$$-\frac{1}{2\pi} \int_{-1}^{+1} \frac{\gamma(\bar{x}) d\bar{x}}{(x - \bar{x})} = -A_0 + \sum_{n=1}^{\infty} A_n \cos n\theta. \quad (I-5)$$

Thus equation (I-3) can be written as

$$-h + U\alpha - b\dot{\alpha} \cos \theta - A_0 + \sum_{n=1}^{\infty} A_n \cos n\theta + \sum_{n=1}^{NX} \frac{\Delta \Gamma_n / b}{2\pi(\xi_n + \cos \theta)} = 0. \quad (I-6)$$

By expanding each term of the summation in a cosine series and then equating coefficients of like terms in the resulting equation, the following expressions for the Glauert coefficients are obtained:

$$\begin{aligned} \pi b A_0 &= \frac{1}{2} \left[2\pi b (-h + U\alpha) \right] + \frac{1}{2} \sum_{n=1}^{NX} \Delta \Gamma_n \mathcal{A}_{0n} \\ \pi b A_1 &= \pi b^2 \dot{\alpha} - \sum_{n=1}^{NX} \Delta \Gamma_n \mathcal{A}_{1n} \\ \pi b A_m &= - \sum_{n=1}^{NX} \Delta \Gamma_n \mathcal{A}_{mn} ; \quad m = 2, 3, 4, \dots \end{aligned} \quad (I-7)$$

where

$$\mathcal{A}_{mn} = \frac{(\sqrt{\xi_n^2 - 1} - \xi_n)^m}{\sqrt{\xi_n^2 - 1}} \quad (I-8)$$

is the result of evaluating the Fourier cosine coefficients of the terms of the summation of (I-6).

The total bound vorticity for blade position k is obtained by integrating $\gamma(\theta)$ (equation I-4) over the chord. Thus,

$$\begin{aligned} \Gamma_k &= 2\pi b \left(A_0 + \frac{1}{2} A_1 \right)_k \\ \Gamma_k &= I_k + \sum_{n=1}^{NX} \Delta \Gamma_n (\mathcal{A}_{0n} - \mathcal{A}_{1n})_k \\ \Gamma_k &= I_k + \sum_{n=1}^{NX} \Delta \Gamma_n \zeta_{kn} \end{aligned} \quad (I-9)$$

where

$$I_k = \left[2\pi b (-h + U\alpha) + \pi b^2 \dot{\alpha} \right]_k$$

is the quasi-steady part of Γ_k , and

$$\zeta_{kn} = (\mathcal{A}_{0n} - \mathcal{A}_{1n})_k.$$

Because the $\Delta \Gamma_n$ are differences of the X values of Γ_k , (I-9) can be written as

$$\Gamma_k = I_k + \sum_{n=1}^{N-1} \left\{ (\Gamma_{k-1} - \Gamma_k)_1 \zeta_{k1} + (\Gamma_{k-2} - \Gamma_{k-1})_2 \zeta_{k2} + \dots \right\}. \quad (I-10)$$

By regrouping the summation on like Γ_k , a set of N simultaneous equations in Γ_k are obtained as

$$\Gamma_k = I_k + \sum_{j=1}^N \sigma_{kj} \Gamma_j \quad (I-11)$$

where σ_{kj} is the summation of all $\zeta's$ which in (I-10) are coefficients of Γ_j .

For specified I_k , the set of equations (I-11) are solved for the Γ_k and then the Glauert coefficients evaluated by equations (I-7). With the Glauert coefficients, the ratios of lift and moment to their quasi-steady values are, for each position, k , of the airfoil, computed from.

$$\begin{aligned} \left(\frac{L}{L_o} \right)_k &= \frac{2\pi b_k}{I_k} \left[A_o + \frac{1}{2} A_1 + \frac{ib\omega}{2U} \left(3A_o + A_1 + \frac{1}{2} A_2 \right) \right]_k \\ \left(\frac{M}{M_o} \right)_k &= \frac{2\pi b_k}{I_k} \left[A_o + \frac{1}{2} A_1 - \frac{ib\omega}{2U} \left(A_o + \frac{3}{4} A_1 - \frac{1}{4} A_2 \right) \right]_k \end{aligned} \quad (I-12)$$

where

$$\begin{aligned} L_o &= \rho U I_k \\ M_o &= \rho U I_k \frac{b_k}{2}. \end{aligned} \quad (I-13)$$

The Glauert coefficients are complex and thus the L/L_o and M/M_o will be complex.

The relative merit of this wake representation was investigated by computing the lift and pitching moment transfer functions (i. e., L/L_o and M/M_o versus reduced frequency, $b\omega/U$) and comparing with the classical results as presented by Karman and Sears in reference 8 for an airfoil oscillating in plunging or in pitching. It should be noted that the results as presented for oscillation in pitch represent only the pitch rate effects (i. e., due to $\dot{\alpha}$ only); this was done because the effect of the pitching displacement is the same as for plunging velocity (i. e., both \dot{h} and $\dot{\alpha}$ contribute only to the constant component of the impressed chordwise velocity distribution and thus affect only A_o whereas $\dot{\alpha}$ affects only A_1 .

The quasi-steady component, I_k , of the bound vorticity depends on both the pitching and plunging motions of the blade. Thus for the computations (whether for pitching or plunging oscillations), I_k is always set equal to $1 \cdot \cos \omega t$ and then interpreted as either the quasi-steady part of A_o or A_1 in evaluating the Glauert coefficients. That is, the difference in the

computations for the plunging and pitching cases is only in the evaluation of the A_0 and A_1 Glauert coefficients. Because I_k was taken as $1 \cdot \cos \omega t$, the cosine components of the resulting L/L_0 and M/M_0 are interpreted as the real parts and the sine components as the negative imaginary parts.

In Figure I. 1 are presented the results of the computations when the wake advance was set equal to zero (i. e., $D = 1 + \bar{a}$). That is, the distance of the first shed vortex behind the trailing edge is always equal to the shed vortex spacing, \bar{a} . The computations were made for $\bar{X} = 3, 8, 30$, and 90 shed vortices per cycle of the blade oscillation and the reduced frequency, $b\omega/U$ range from 0 to 0.8. Figure I. 1a presents the L/L_0 and M/M_0 for the airfoil oscillating in plunge, and Figure I. 1b presents them for the airfoil oscillating in pitch. The agreement with the classical solution improves as \bar{X} increases, which is to be expected because the wake representation is approaching the continuous wake. A vector drawn from the origin to a point on one of the curves represents the magnitude and phase angle (relative to the quasi-steady values) of that quantity for reduced frequency corresponding to the point; note that the scale of the abscissa has been broken between 0 and 0.5 on several figures. It is noted that the differences between the approximate wake results and the exact wake results is primarily in the phase and that the agreement is better for the pitching moments than the lift.

The computations were repeated for several values of the wake advance relative to the blade and, although the results improved with increasing wake advance, the optimum appeared to be about 70 percent. The results for the wake advanced 70 percent (i. e., $D = 1 + \bar{a}/3$) are presented in Figure I. 2. It can be seen that the curves for various numbers \bar{X} , of shed vortices per cycle are grouped much closer to the classical results and that the discrepancies in both the magnitude and phase angle have been reduced. The principal difference between the approximate and classical results is still in the phase angle; the pitching moments, M/M_0 , are in better agreement than the lift L/L_0 .

It should be remembered that the curves presented from this investigation are for a constant number, \bar{X} , of shed vortices per cycle. The use of a similar wake representation for a rotor does not result in \bar{X} being a constant, but rather \bar{X} is then a function of the blade radius and harmonic order of the blade dynamic response. For the rotor wake application, it is the shed vortex spacing, \bar{a} , which is relatively constant (there is some variation with azimuth angle, ψ , from the retreating to the advancing sides of the rotor) and the number, \bar{X} , of shed vortices per cycle decreases with increasing harmonic order (i. e., the lowest harmonics have the best representation).

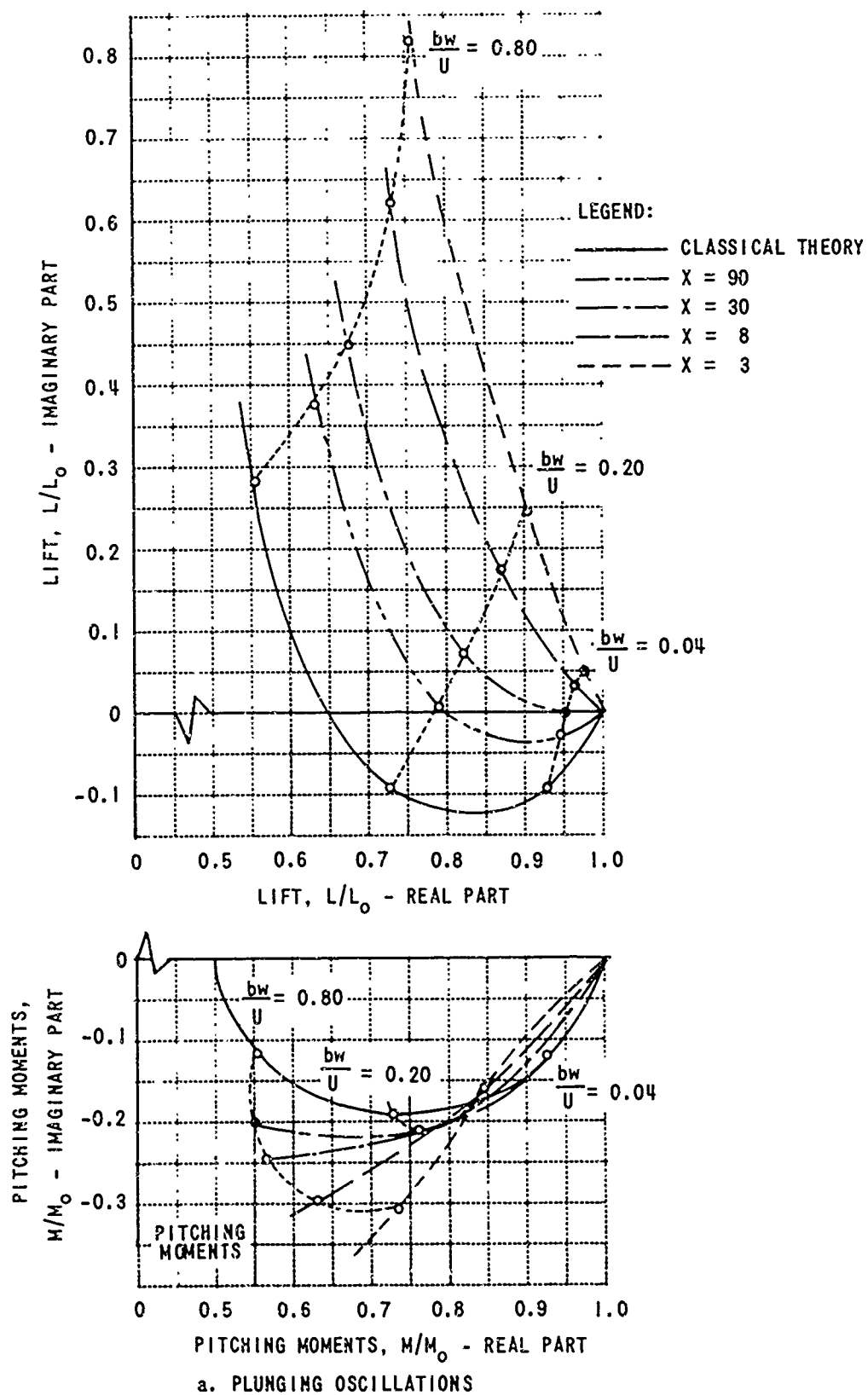
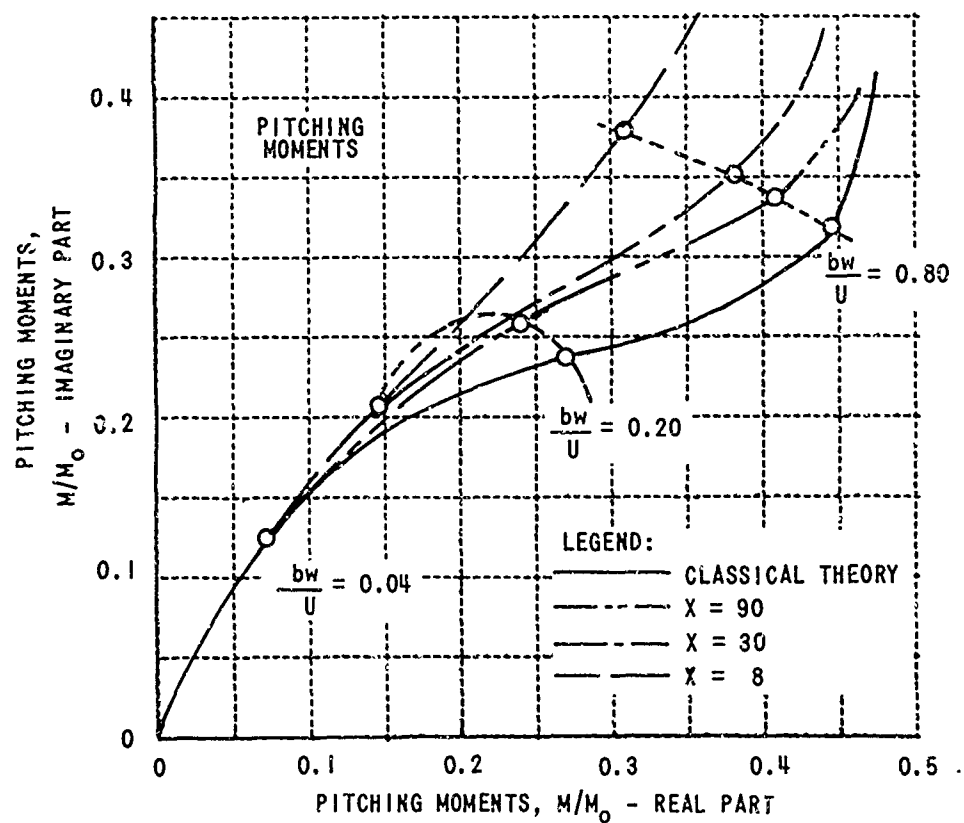
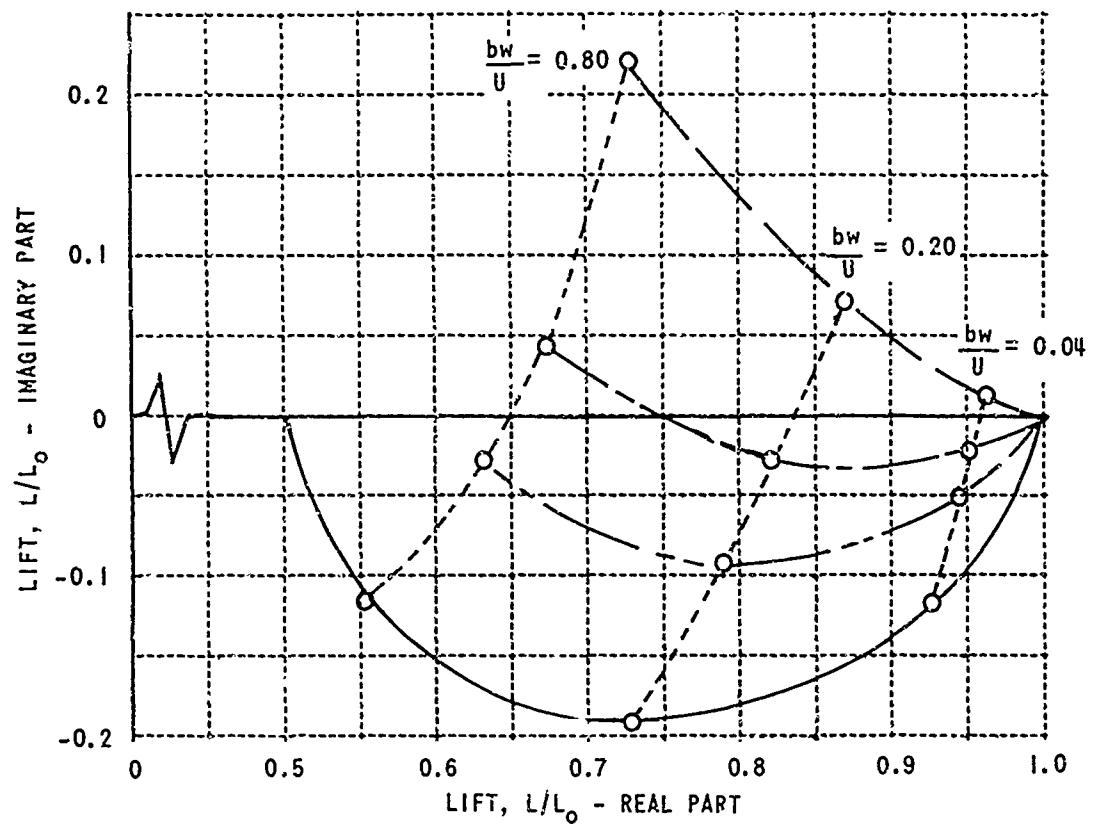
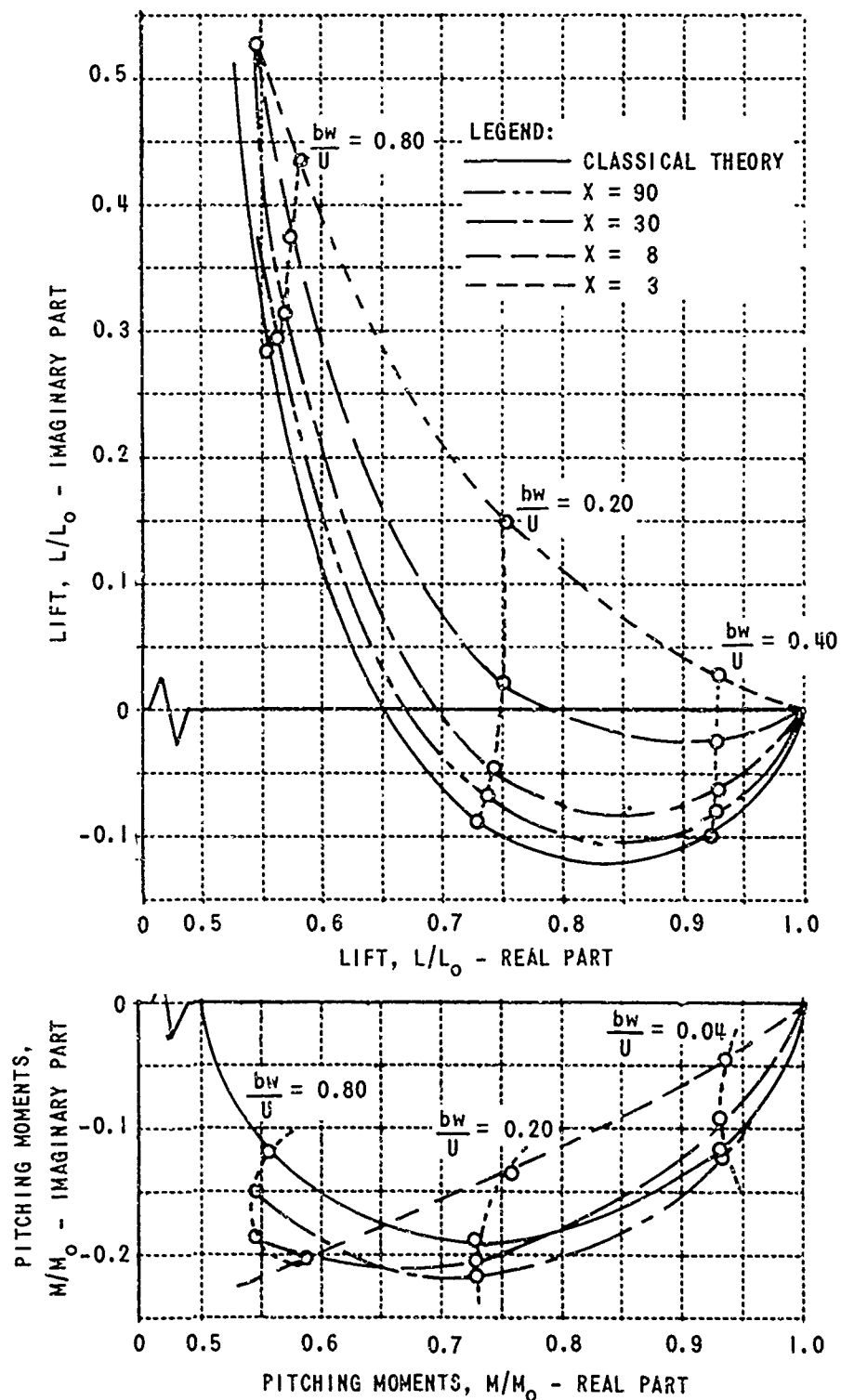


Figure I.1 TWO-DIMENSIONAL OSCILLATING AIRFOIL LIFT AND PITCHING MOMENT TRANSFER FUNCTIONS; ZERO WAKE ADVANCE ($D = 1 + \bar{d}$).



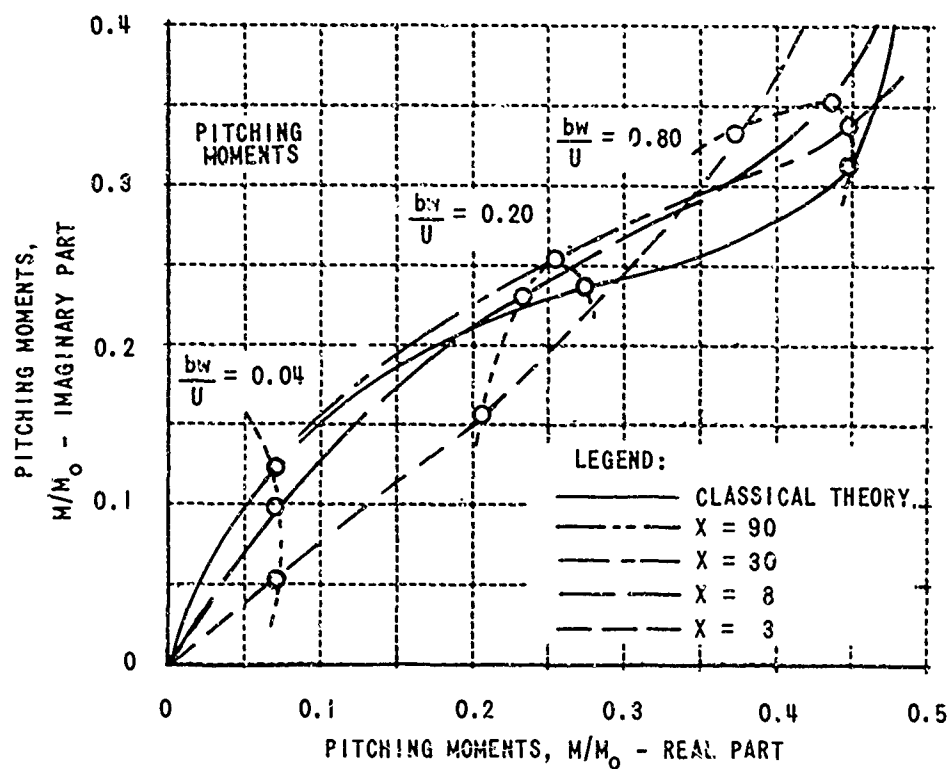
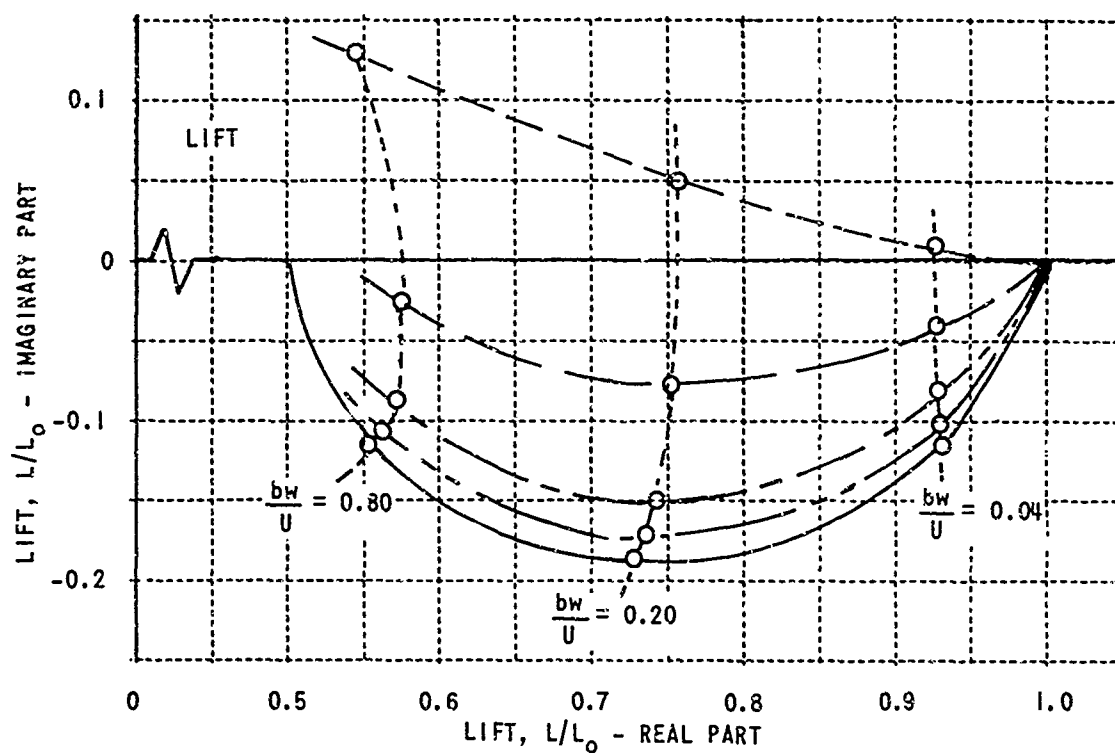
b. PITCHING OSCILLATIONS

Figure I.1 (Cont'd). TWO-DIMENSIONAL OSCILLATING AIRFOIL LIFT AND PITCHING MOMENT TRANSFER FUNCTIONS; ZERO WAKE ADVANCE ($D = 1 + \bar{d}$).



a. PLUNGING OSCILLATIONS

Figure I.2. TWO-DIMENSIONAL OSCILLATING AIRFOIL LIFT AND PITCHING MOMENT TRANSFER FUNCTIONS; 0.70 WAKE ADVANCE ($D = 1+d/3$).



b. PITCHING OSCILLATIONS

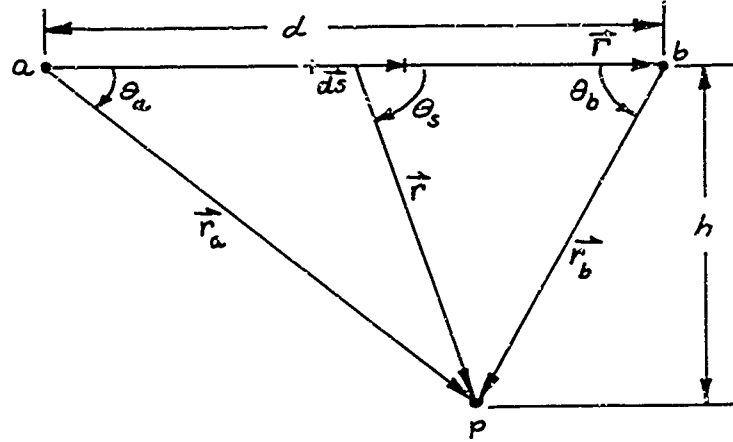
Figure I.2 (Cont'd). TWO-DIMENSIONAL OSCILLATING AIRFOIL LIFT AND PITCHING MOMENT TRANSFER FUNCTIONS; 0.70 WAKE ADVANCE ($D = 1 + \bar{d}/3$).

APPENDIX II

THE CHORDWISE INDUCED VELOCITY DISTRIBUTION

DUE TO A WAKE VORTEX ELEMENT

The notation to be used is defined in the following diagram, where a and b are the end points of the straight-line vortex filament and p is the point at which the induced velocity is to be computed. These three points can be arbitrarily oriented in space.



The differential induced velocity at a point due to an elemental length of vortex filament is given in vector notation as

$$d\vec{q} = \frac{\Gamma}{4\pi r^3} (\vec{ds} \times \vec{r}). \quad (\text{II-1})$$

This can be put in the following form:

$$d\vec{q} = \left(\frac{\Gamma h}{4\pi r^3} ds \right) \vec{K} \quad (\text{II-2})$$

where the expression in parentheses is the magnitude and \vec{K} is a unit vector in the direction of the velocity which can be expressed in Cartesian components as

$$\begin{aligned} \vec{K} = \left(\frac{r_a}{h} \right) \{ & (\cos \gamma_a \cos \beta_s - \cos \beta_a \cos \gamma_s) \vec{i} \\ & + (\cos \alpha_a \cos \gamma_s - \cos \gamma_a \cos \alpha_s) \vec{j} \\ & + (\cos \beta_a \cos \alpha_s - \cos \alpha_a \cos \beta_s) \vec{k} \}. \end{aligned} \quad (\text{II-3})$$

The cosines of the angles α , β , and γ subscripted with a and b are, respectively, the direction cosines of the vectors \vec{r} and \vec{r}_a of the diagram on the previous page.

The total velocity at ρ due to the vortex filament is obtained by integrating (II-2) over the length of the filament from a to b ; the result is

$$\vec{q} = \frac{\Gamma h}{4\pi} \left[\frac{d - (r_a - r_b) \cos \theta_a}{r_a^2 r_b (1 - \cos^2 \theta_a)} \right] \vec{k} . \quad (\text{II-4})$$

For use in the numerical computations, this expression for the velocity is written in terms of the direction numbers (and thereby the coordinates of the three points) of the two radius vectors from the filament end points to the point, ρ , as follows:

$$\vec{q} = \left[\frac{(\Gamma/4\pi)(r_a + r_b)}{r_a r_b (r_a r_b + l_a l_b + m_a m_b + n_a n_b)} \right] \left\{ (m_a n_b - m_b n_a) \vec{i} + (l_a n_b + l_b n_a) \vec{j} + (l_a m_b - l_b m_a) \vec{k} \right\} \quad (\text{II-5})$$

where

$$\left. \begin{aligned} l_i &= x - \xi_i \\ m_i &= y - \eta_i \\ n_i &= z - \zeta_i \\ r_i^2 &= l_i^2 + m_i^2 + n_i^2 \end{aligned} \right\} i = a \text{ or } b$$

are the direction numbers and magnitudes of the vectors, r_a and r_b . The (x, y, z) are the coordinates of the point, ρ , and (ξ, η, ζ) are the coordinates of the vortex filament end points with the corresponding subscript.

Only the z -component of the chordwise induced velocity distribution is used in the present method. The expression for this chordwise distribution can be derived from the z -component of (II-5) by considering it to express the induced velocity at any one point (x, y, z) on the chord and expressing this point in terms of a chordwise coordinate s (relative to the midchord) by the following expressions:

$$\begin{aligned} x &= x_m - \frac{\Delta x}{b} s \\ y &= y_m - \frac{\Delta y}{b} s \\ z &= z_m - \frac{\Delta z}{b} s \end{aligned} \quad (\text{II-6})$$

where

$$\Delta x = x_L - x_M$$

$$\Delta y = y_L - y_M$$

$$\Delta z = z_L - z_M$$

are the direction numbers for the semichord (subscripts L and M designate the leading edge and the midchord points, respectively). When these expressions are substituted for x, y and z in the z -components of (II-5), the following expression for the z -component of the chordwise induced velocity is obtained in terms of the chordwise coordinate s :

$$q_z = \frac{\left(\frac{\Gamma}{4\pi}\right) \left[\sqrt{C_1 + C_2 s + C_3 s^2} + \sqrt{C_4 + C_5 s + C_6 s^2} \right] \left[C_7 + C_8 s + C_9 s^2 \right]}{\sqrt{C_1 + C_2 s + C_3 s^2} \sqrt{C_4 + C_5 s + C_6 s^2} \left[\sqrt{C_1 + C_2 s + C_3 s^2} \sqrt{C_4 + C_5 s + C_6 s^2} + C_{10} + C_{11} s + C_{12} s^2 \right]} \quad (\text{II-7})$$

where

$$C_1 = (x_M - \xi_a)^2 + (y_M - \eta_a)^2 + (z_M - \zeta_a)^2$$

$$C_2 = -\frac{2}{b} \left[(x_M - \xi_a) \Delta x + (y_M - \eta_a) \Delta y + (z_M - \zeta_a) \Delta z \right]$$

$$C_3 = \frac{1}{b^2} \left[\Delta x^2 + \Delta y^2 + \Delta z^2 \right] = 1$$

$$C_4 = (x_M - \xi_b)^2 + (y_M - \eta_b)^2 + (z_M - \zeta_b)^2$$

$$C_5 = -\frac{2}{b} \left[(x_M - \xi_b) \Delta x + (y_M - \eta_b) \Delta y + (z_M - \zeta_b) \Delta z \right]$$

$$C_6 = C_3 = 1$$

$$C_7 = (x_M - \xi_a)(y_M - \eta_b) - (x_M - \xi_b)(y_M - \eta_a)$$

$$C_8 = -\frac{1}{b} \left[\left\{ (x_M - \xi_a) - (x_M - \xi_b) \right\} \Delta y + \left\{ (y_M - \eta_b) - (y_M - \eta_a) \right\} \Delta x \right]$$

$$C_9 = 0$$

$$C_{10} = (x_M - \xi_a)(x_M - \xi_b) + (y_M - \eta_a)(y_M - \eta_b) + (z_M - \zeta_a)(z_M - \zeta_b)$$

$$C_{11} = \frac{1}{2} (C_2 + C_5)$$

$$C_{12} = C_3 = 1.$$

(II-8)

For the present application, the first four Fourier cosine components of the induced velocity distribution given by (II-7) are desired but the integrals for the Fourier coefficients of (II-7) could not be evaluated. The complexity of equation (II-7) arises because it expresses the chordwise induced velocity for all relative orientations of the chord and vortex filament, including the situation where they are extremely close (or intersecting) and the chordwise velocity variations are very rapid. It was assumed that, for this application, the chord to wake filament distances encountered in the computer program will never be extremely small and, therefore, the corresponding chordwise variations of the induced velocity due to the elements will not be very rapid. Thus when (II-7) is expanded in a power series, about $s = 0$, only the first four components are retained and this finite power series is transformed to a cosine series. The resultant power series is:

$$\begin{aligned} \frac{4\pi\gamma}{r} = & \frac{\alpha_0}{\beta_0} + \left[\frac{\alpha_1}{\beta_0} - \frac{\alpha_0\beta_1}{\beta_0^2} \right] s \\ & + \left[\frac{\alpha_2}{\beta_0} - \frac{\alpha_1\beta_1}{\beta_0^2} + \alpha_0 \left(\frac{\beta_1^2}{\beta_0^3} - \frac{\beta_2}{\beta_0^2} \right) \right] s^2 \\ & + \left[\frac{\alpha_3}{\beta_0} - \frac{\alpha_2\beta_1}{\beta_0^2} + \alpha_1 \left(\frac{\beta_1^2}{\beta_0^2} - \frac{\beta_2}{\beta_0^2} \right) + \alpha_0 \left(\frac{2\beta_1\beta_2}{\beta_0^3} - \frac{\beta_3}{\beta_0^2} - \frac{\beta_1^3}{\beta_0^4} \right) \right] s^3 \end{aligned} \quad (\text{II-9})$$

where

$$\alpha_0 = c_7 (\sqrt{c_1} + \sqrt{c_4})$$

$$\alpha_1 = c_7 \left(\frac{1}{2} \frac{c_2}{\sqrt{c_1}} + \frac{1}{2} \frac{c_5}{\sqrt{c_4}} \right) + c_8 (\sqrt{c_1} + \sqrt{c_4})$$

$$\alpha_2 = c_7 \left[\sqrt{c_1} \left(\frac{1}{2c_1} - \frac{1}{8} \frac{c_2^2}{c_1^2} \right) + \sqrt{c_4} \left(\frac{1}{2c_4} - \frac{1}{8} \frac{c_5^2}{c_4^2} \right) \right] + \frac{c_8}{2} \left(\frac{c_2}{\sqrt{c_1}} + \frac{c_5}{\sqrt{c_4}} \right)$$

$$\begin{aligned} \alpha_3 = & c_7 \left[\sqrt{c_1} \left(\frac{1}{16} \frac{c_2^3}{c_1^3} - \frac{1}{4} \frac{c_2}{c_1^2} \right) + \sqrt{c_4} \left(\frac{1}{16} \frac{c_5^3}{c_4^3} - \frac{1}{4} \frac{c_5}{c_4^2} \right) \right] \\ & + c_8 \left[\sqrt{c_1} \left(\frac{1}{2c_1} - \frac{1}{8} \frac{c_2^2}{c_1^2} \right) + \sqrt{c_4} \left(\frac{1}{2c_4} - \frac{1}{8} \frac{c_5^2}{c_4^2} \right) \right] \end{aligned}$$

$$\beta_0 = c_1 c_4 + c_{10} \sqrt{c_1 c_4}$$

$$\beta_1 = c_1 c_5 + c_2 c_4 + \sqrt{c_1 c_4} \left[c_{11} + \frac{c_{10}}{2} \left(\frac{c_2}{c_1} + \frac{c_5}{c_4} \right) \right]$$

$$\begin{aligned}
\beta_2 = & c_1 + c_2 c_5 + c_4 + \sqrt{c_1 c_4} \left[c_{10} \left(\frac{1}{2c_1} - \frac{1}{8} \frac{c_2^2}{c_1^2} + \frac{1}{4} \frac{c_2 c_5}{c_1 c_4} + \frac{1}{2c_4} - \frac{1}{8} \frac{c_5^2}{c_4^2} \right) \right. \\
& \left. + \frac{c_{11}}{2} \left(\frac{c_2}{c_1} + \frac{c_5}{c_4} \right) + 1 \right] \\
\beta_3 = & c_2 + c_5 + \sqrt{c_1 c_4} \left\{ \frac{c_{10}}{2} \left[\frac{1}{8} \left(\frac{c_2^3}{c_1^3} + \frac{c_5^3}{c_4^3} \right) - \frac{1}{2} \left(\frac{c_2}{c_1^2} + \frac{c_5}{c_4^2} \right) \right. \right. \\
& \left. \left. + \frac{c_5}{c_4} \left(\frac{1}{2c_1} - \frac{1}{8} \frac{c_2^2}{c_1^2} \right) + \frac{c_2}{c_1} \left(\frac{1}{2c_4} - \frac{1}{8} \frac{c_5^2}{c_4^2} \right) \right] + \right. \\
& \left. + c_{11} \left[\left(\frac{1}{2c_1} - \frac{1}{8} \frac{c_2^2}{c_1^2} \right) + \frac{1}{4} \frac{c_2 c_5}{c_1 c_4} + \left(\frac{1}{2c_4} - \frac{1}{8} \frac{c_5^2}{c_4^2} \right) \right] + \frac{1}{2} \left(\frac{c_2}{c_1} + \frac{c_5}{c_4} \right) \right\}
\end{aligned} \tag{II-10}$$

and the c 's are defined in (II-8). In the computer program a further hierarchy of symbolization was used to take advantage of the repetition of certain groups and combinations of the c 's and thereby increase the computational efficiency.

The transformation from the power series (II-9) to the following cosine series

$$\frac{4\pi}{r} q_3 = s_0 + s_1 \cos \theta + s_2 \cos 2\theta + s_3 \cos 3\theta \tag{II-11}$$

is effected by the following transformation:

$$\begin{aligned}
s &= -b \cos \theta \\
\text{where} \\
s_0 &= a_0 + \frac{1}{2} a_2 \\
s_1 &= -a_1 - \frac{3}{4} a_3 \\
s_2 &= \frac{1}{2} a_2 \\
s_3 &= -\frac{1}{4} a_3
\end{aligned} \tag{II-12}$$

and the a_n ($n = 0, 1, 2, 3$) are the coefficients of (II-9) multiplied by b_n . Thus (II-12) are the desired expressions for the first four cosine coefficients of the chordwise induced velocity distribution due to a single wake element, but it should be noted they have been approximated by truncating the power series.

APPENDIX III

EFFICIENT METHOD FOR NUMERICALLY COMPUTING DERIVATIVES OF PERIODIC FUNCTIONS

If a periodic function is numerically defined at NA equally spaced points on its period, it is possible to represent it with a finite Fourier series of NA terms (reference 12, page 430). When NA is an even number, the series is

$$f(\psi_k) = \sum_{n=0}^{\frac{NA}{2}} a_n \cos n \psi_k + \sum_{n=1}^{\frac{NA}{2}-1} b_n \sin n \psi_k \quad (\text{III-1})$$

where

$$a_0 = \frac{1}{NA} \sum_{k=1}^{k=NA} f(\psi_k) \quad (\text{III-1a})$$

$$\left. \begin{aligned} a_n &= \frac{2}{NA} \sum_{k=1}^{k=NA} f(\psi_k) \cos n \psi_k \\ b_n &= \frac{2}{NA} \sum_{k=1}^{k=NA} f(\psi_k) \sin n \psi_k \end{aligned} \right\} \begin{array}{l} n \neq 0 \\ n < \frac{NA}{2} \end{array} \quad (\text{III-1b})$$

$$a_{\frac{NA}{2}} = \frac{1}{NA} \sum_{k=1}^{k=NA} f(\psi_k) \cos \pi(k-1) \quad (\text{III-1c})$$

$$\psi_k = (k-1) \Delta \psi$$

$$\Delta \psi = 2\pi/NA$$

When NA is an odd number, the last cosine term, $a_{NA/2}$, is absent.

The first derivative of the function can also be represented by a Fourier series as follows:

$$f'(\psi_k) = -\sum_{n=1}^{\frac{NA}{2}} n a_n \sin n \psi_k + \sum_{n=1}^{\frac{NA}{2}-1} n b_n \cos n \psi_k. \quad (\text{III-2})$$

If the expressions (III-1) are substituted for the coefficients of (III-2), the derivative can be written as

$$f'(\psi_k) = \sum_{\bar{k}=1}^{NA} f(\psi_{\bar{k}}) \left\{ \frac{2}{NA} \sum_{n=1}^{\frac{NA}{2}-1} n \sin \left[\left(\frac{2\pi}{NA} \right) n(\bar{k} - k) \right] \right\} \quad (\text{III-3})$$

which expresses the derivative at a point, ψ_k , in terms of the magnitude of the function at the NA points, $\psi_{\bar{k}}$. It is noted that the expression in braces is only a function of the number, NA , of points at which the function is defined and thus can be precomputed as a set of coefficients.

This procedure is equivalent to solving for the Fourier coefficients of the function by equation (III-1) and then evaluating the derivatives by (III-2); however, it eliminates the step of evaluating the Fourier coefficients by precomputing coefficients of $f(\psi_{\bar{k}})$ in (III-3). This will save a considerable amount of numerical computation when the derivatives must be evaluated for more than one function and each function is defined at the same number, NA , of points.

This procedure was used in the present prediction method because the derivatives of two combinations of Glauert coefficients must be evaluated for each radial station (thus $2 \times NR$ functions) and this must be repeated for each iteration.

It should be noted that this procedure is also applicable to the higher derivatives. For example, the expression for the 2nd derivative is

$$f''(\psi_k) = - \sum_{\bar{k}=1}^{NA} f(\psi_{\bar{k}}) \left\{ \frac{2}{NA} \sum_{n=1}^{\frac{NA}{2}-1} n^2 \cos \left[\left(\frac{2\pi}{NA} \right) n(\bar{k} - k) \right] + \frac{NA}{4} (-1)^{\bar{k}-k} \right\} \quad (\text{III-4})$$

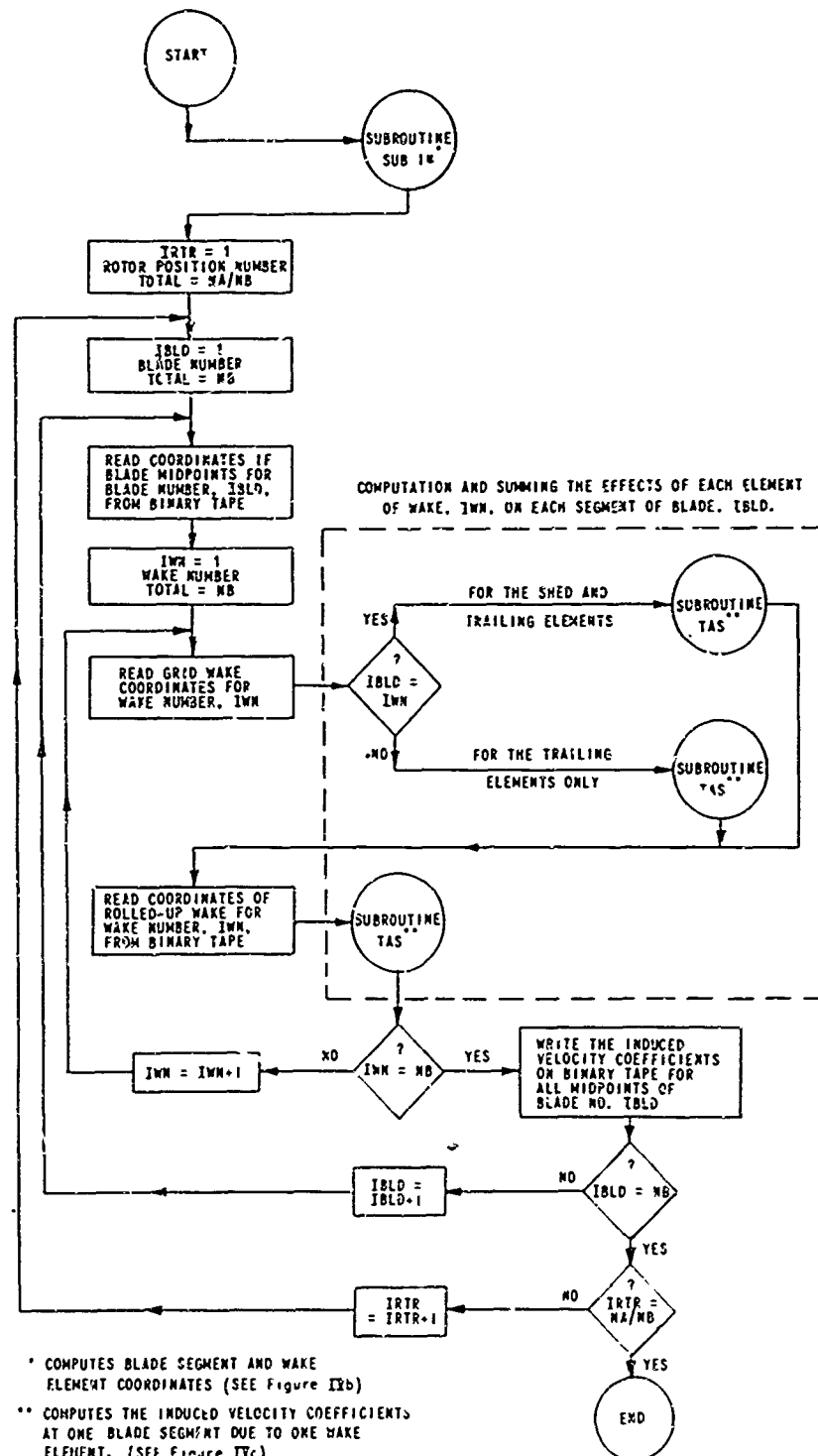
APPENDIX IV

FLOW DIAGRAM FOR THE COMPUTER PROGRAM (PARTS 1 AND 2)

These flow diagrams do not present all the details of the program but only the general flow of both parts and their subroutines. The flow diagrams for program Parts 1 and 2 and their subroutines are presented in Figure IV.1 and IV.2, respectively. The symbols used in these diagrams are defined below.

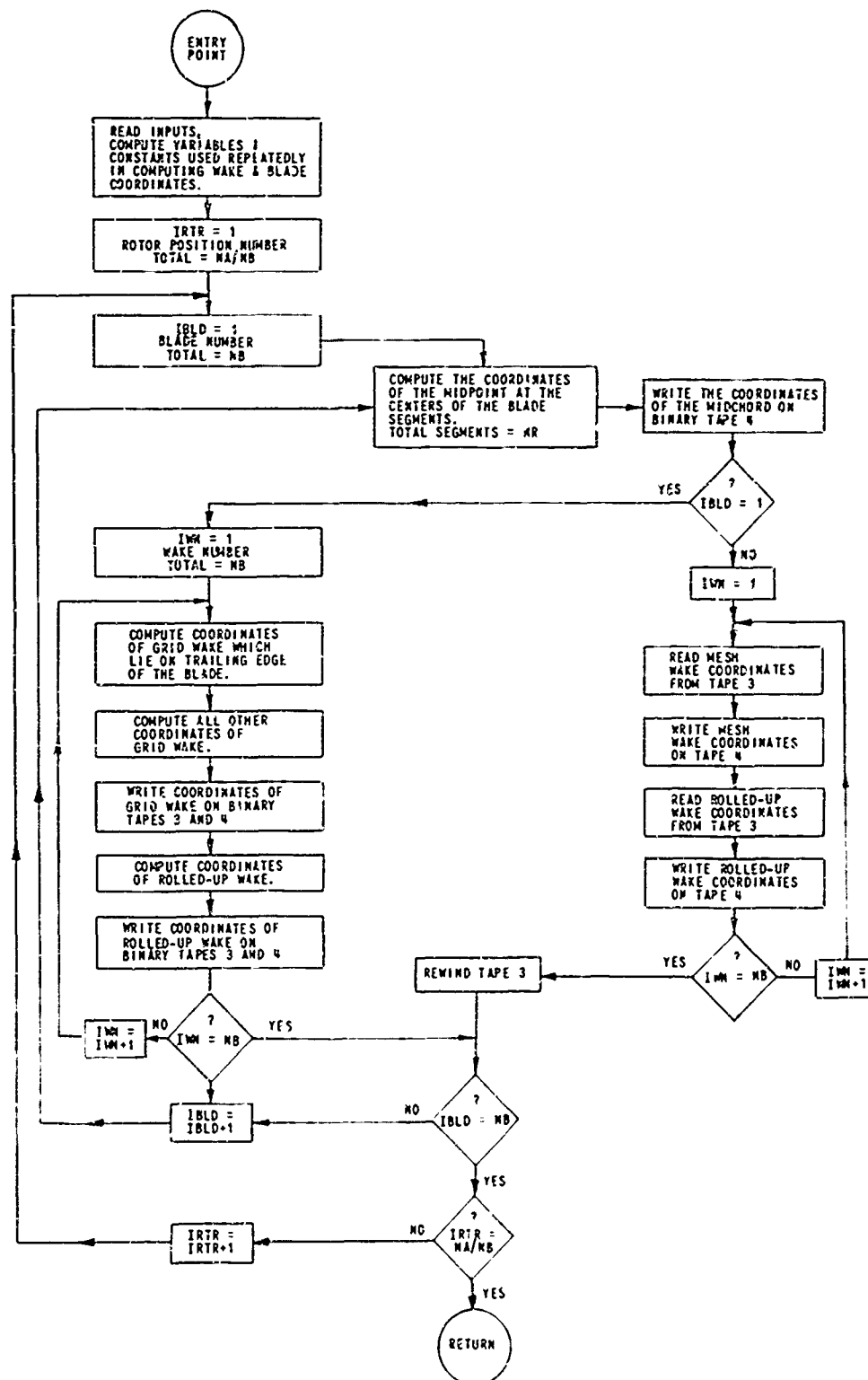
COORD	Name of subroutine which computes blade and wake coordinates
CVLM	The convergence limit for both the Γ_g and the generalized coordinates
GNCRD	Name of subroutine which solves the equations of motion for the response in the generalized coordinates
GNFRCE	Name of subroutine which computes the lift, pitching moments and generalized forces
I	Constant term of the " Γ " equation $(-\dot{h} + V_1 \alpha_g + \frac{1}{2} b \dot{\alpha}_g)$
IBLD	Blade number
IRTR	Rotor position number
IS	Mode (or degree of freedom) number
IST	Glauert coefficient subscript
ISYM	Control word which indicates whether the mode under consideration is symmetric (= +1) or antisymmetric (= -1)
ITG	Iteration number for the Γ -equations
ITM	Iteration number for the blade motions
ITYP	Control word which indicates whether the rotor has a teetering hub (= 1) or a rigid hub (= 2)

IWN	Blade number, whose wake is under analysis
KT	Blade spanwise segment number
KA	Azimuth position number
NA	Number of azimuth positions
NB	Number of blades
ND	Number of blade modes (degrees of freedom)
NER	Number of equally spaced radial blade segments at which the computed lift is interpolated. This is for use in evaluating integrals of the generalized airload.
NITG	Maximum number of iterations allowed on the Γ -equations
NITM	Maximum number of iterations allowed on the blade motions
NR	Number of blade spanwise segments
RA	Distance from wake vortex element to blade segment
RTOGAM	Ratio of the change (between successive iterations) in Γ to its present value
RTOGCD	Ratio of the change (between successive iterations) in tip deflection (for each mode) to its present value
ZN1, ZN2, ZN3	Zones of influence about a blade segment. They determine how the induced effects (due to each wake element) on the blade segment are to be computed.



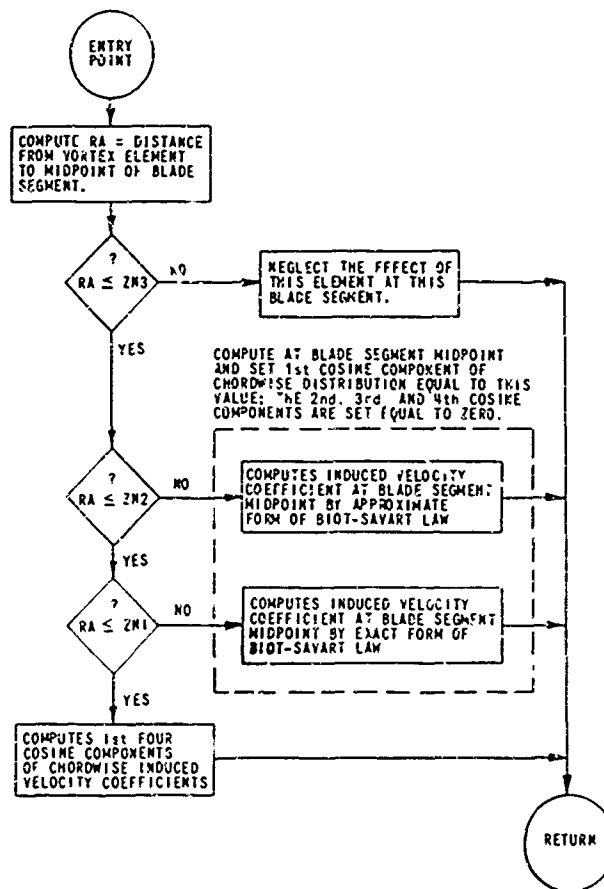
a. MAIN PROGRAM OF PART I

Figure IV.1 FLOW DIAGRAM FOR PART I OF COMPUTER PROGRAM.



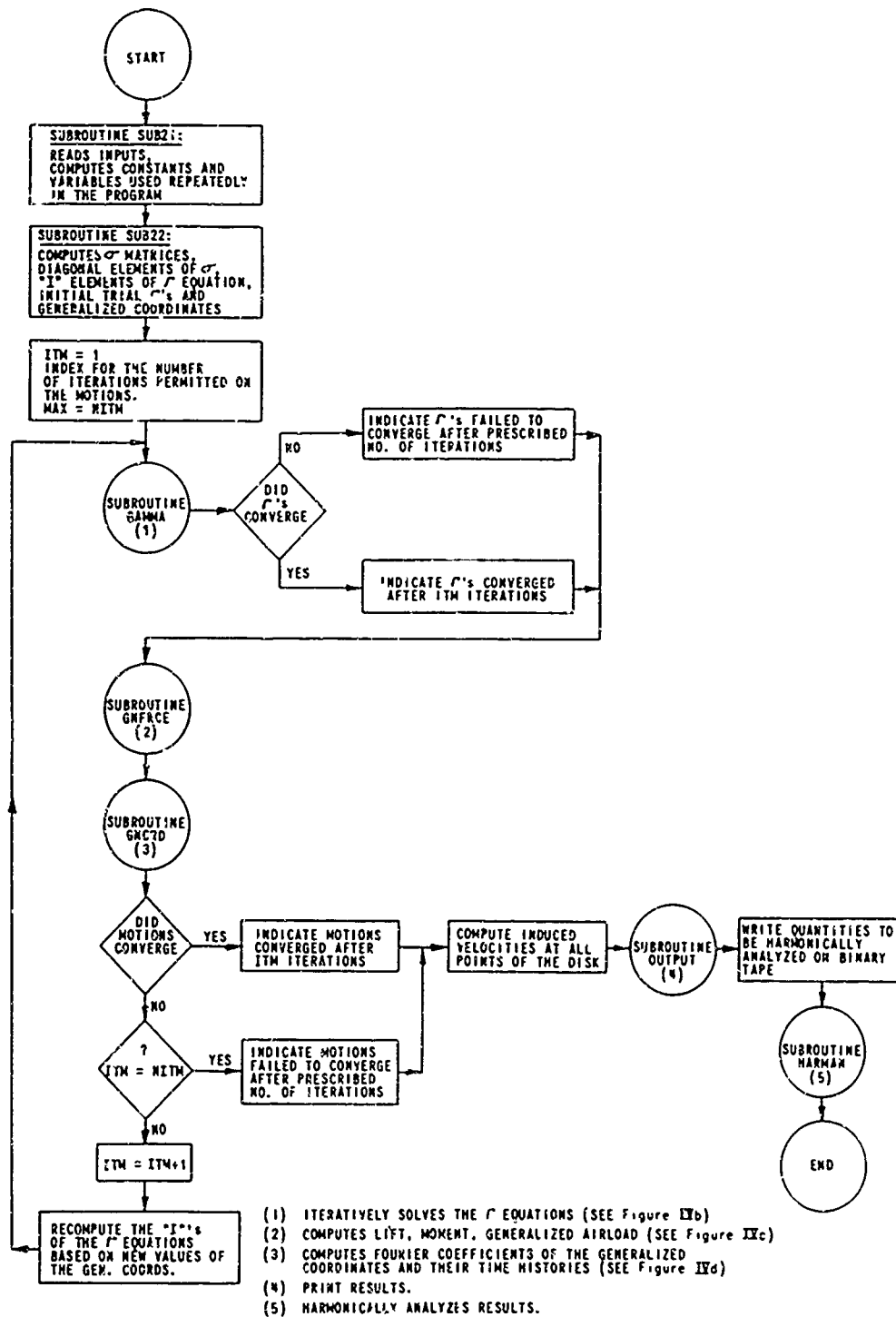
b. SUBROUTINE 14 OF PART I

Figure IV.1 (Cont'd) FLOW DIAGRAM FOR PART I OF COMPUTER PROGRAM.



c. SUBROUTINE COORD OF PART I

Figure IV.1 (Cont'd) FLOW DIAGRAM FOR PART I OF COMPUTER PROGRAM.



a. MAIN PROGRAM OF PART 2

Figure IV.2 FLOW DIAGRAM FOR PART 2 OF COMPUTER PROGRAM.

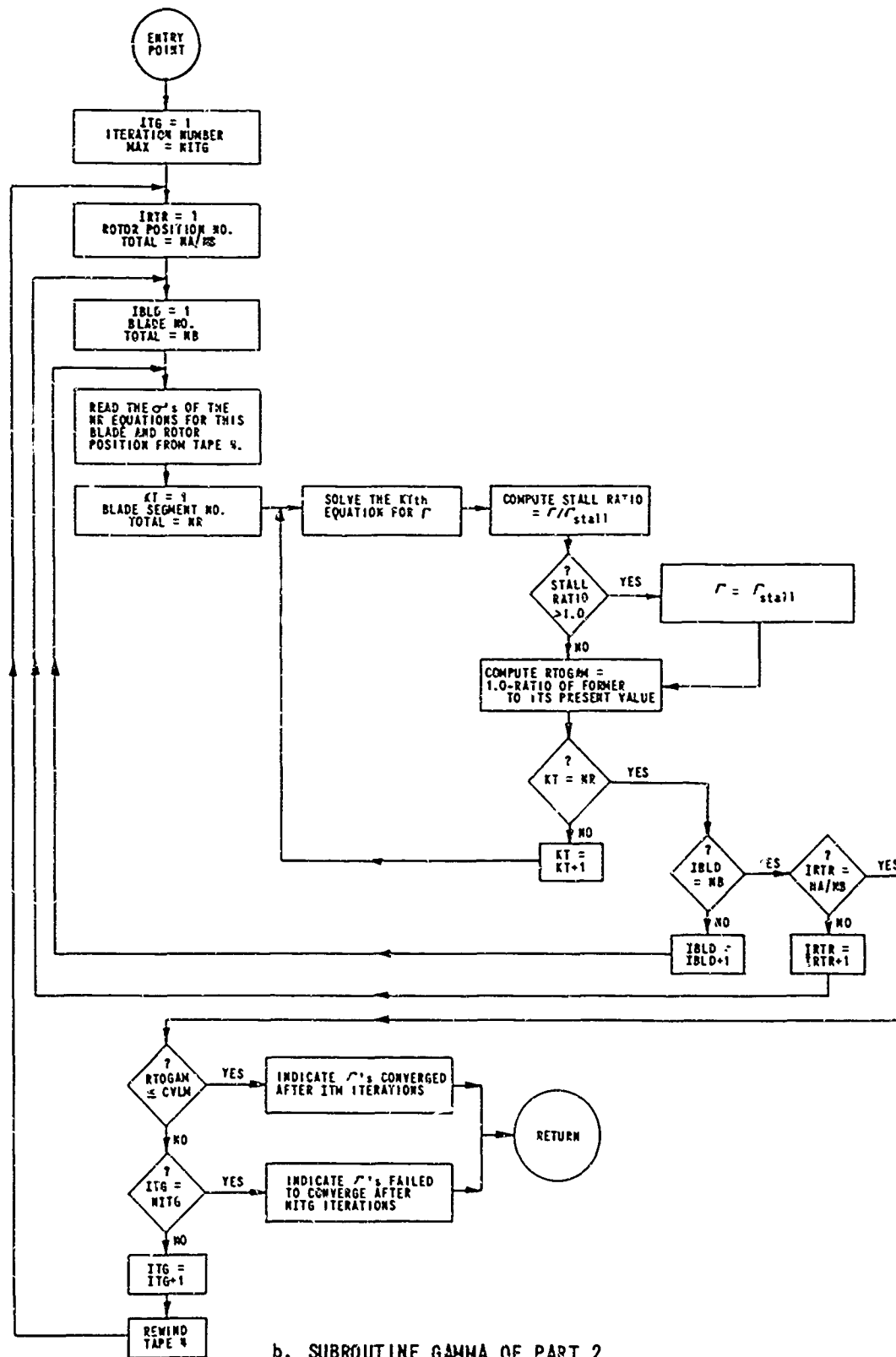
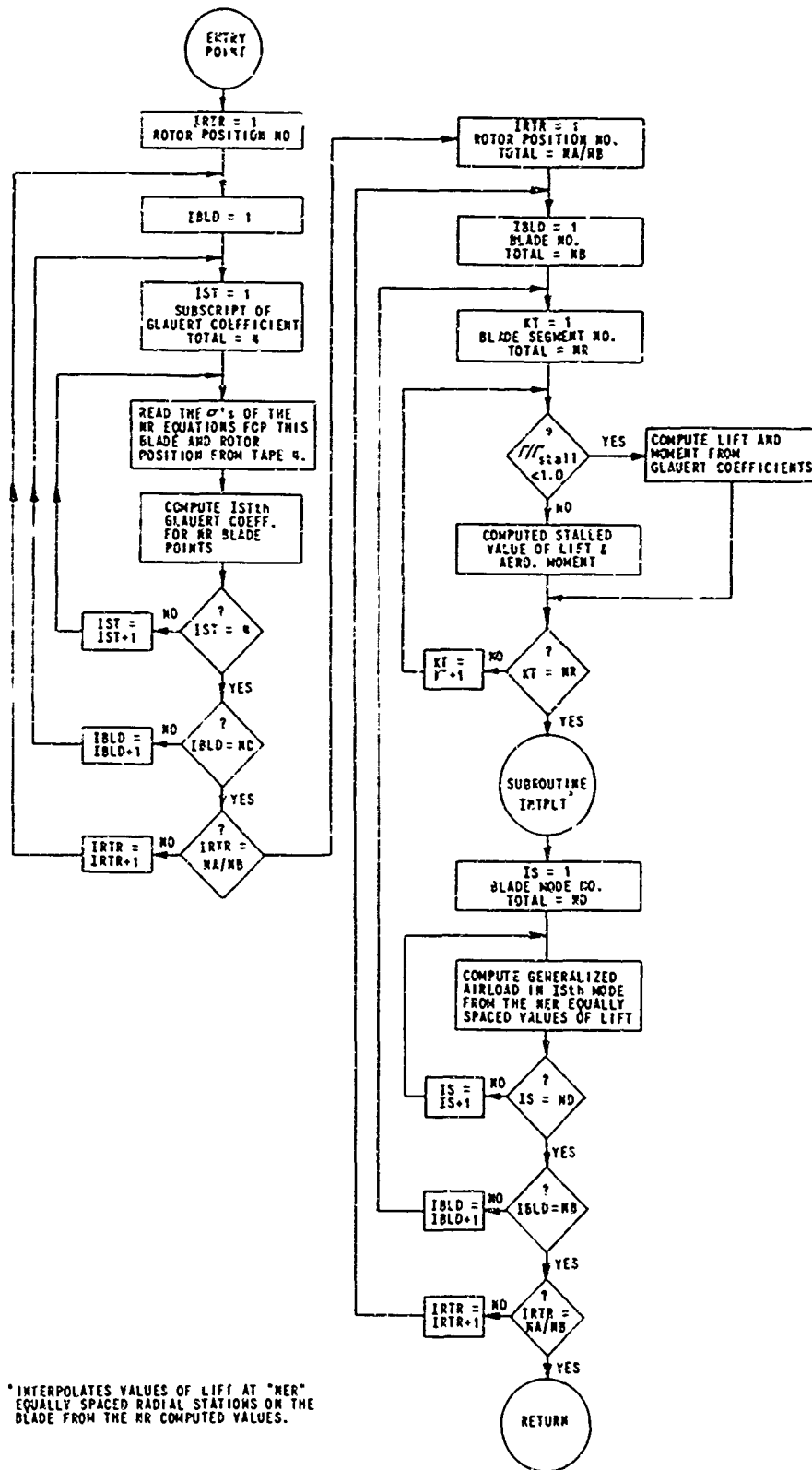
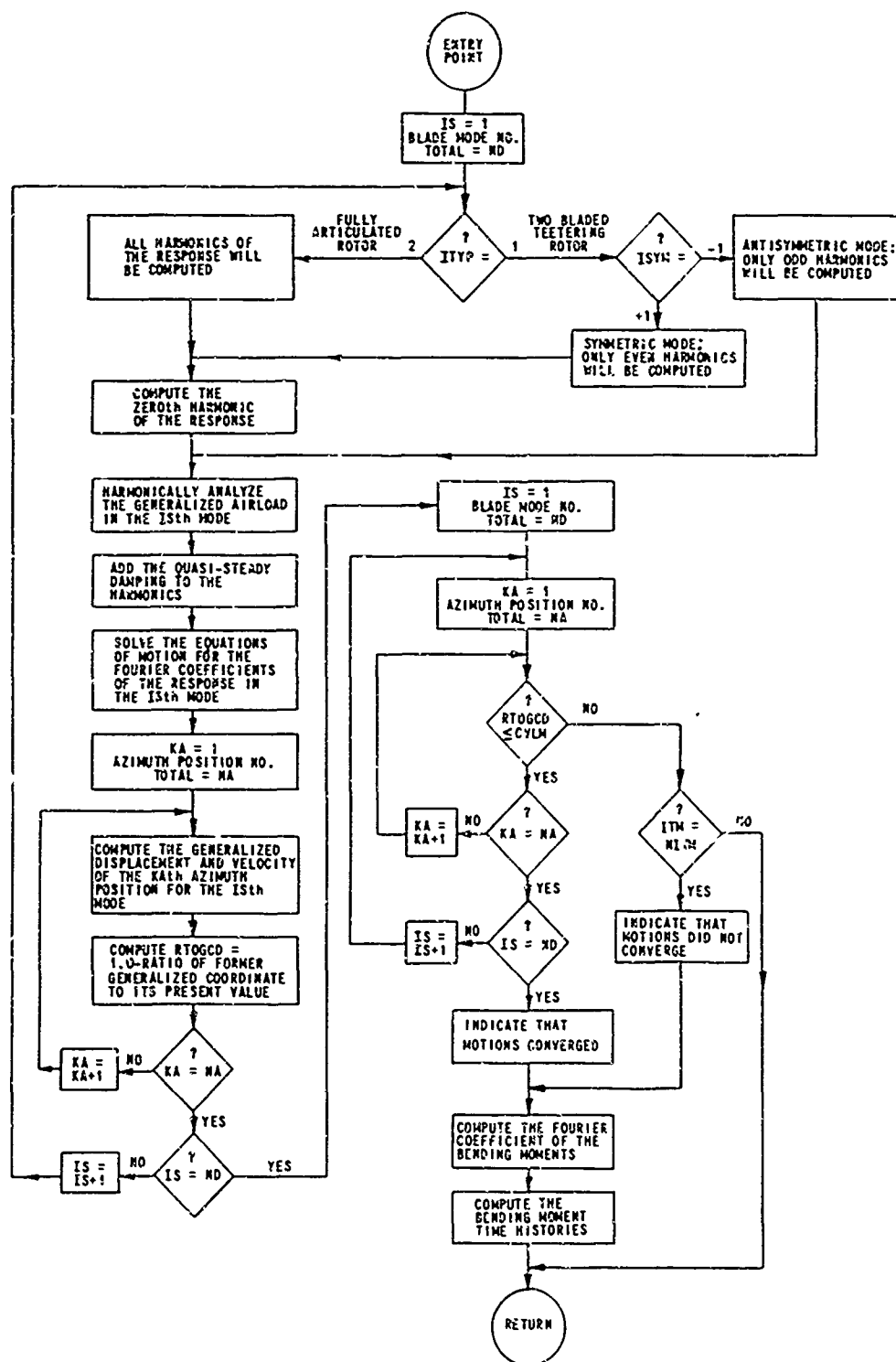


Figure IV.2 (Cont'd) FLOW DIAGRAM FOR PART 2 OF COMPUTER PROGRAM.



c. SUBROUTINE GNFCE OF PART 2

Figure IV.2 (Cont'd) FLOW DIAGRAM FOR PART 2 OF COMPUTER PROGRAM.



d. SUBROUTINE GNCRD OF PART 2

Figure IV.2 (Cnt'd) FLOW DIAGRAM FOR PART 2 OF COMPUTER PROGRAM.

Unclassified

Security Classification

DOCUMENT CONTROL DATA - R&D		
<i>(Security classification of title, body of abstract and indexing annotation must be entered when the overall report is classified)</i>		
1 ORIGINATING ACTIVITY (Corporate author) Cornell Aeronautical Laboratory, Inc. Buffalo, New York 14221		2a REPORT SECURITY CLASSIFICATION Unclassified 2b GROUP
3 REPORT TITLE A Method for Predicting the Aerodynamic Loads and Dynamic Response of Rotor Blades		
4 DESCRIPTIVE NOTES (Type of report and inclusive dates) Final Report April 1964 - July 1965		
5 AUTHOR(S) (Last name, first name, initial) Piziali, Raymond A.		
6. REPORT DATE January 1966	7a TOTAL NO OF PAGES 96	7b NO OF REFS 9
8a CONTRACT OR GRANT NO DA 44-177-AMC-163(T) b. PROJECT NO 1P125901A14604 c d	9a ORIGINATOR'S REPORT NUMBER(S) USAAVLABS Technical Report 65-74 9b OTHER REPORT NO(S) (Any other numbers that may be assigned this report) BB 1932-S-1	
10 AVAILABILITY/LIMITATION NOTICES Distribution of this document is unlimited.		
11 SUPPLEMENTARY NOTES	12 SPONSORING MILITARY ACTIVITY US Army Aviation Materiel Laboratories Fort Eustis, Virginia	
13 ABSTRACT <p>A method for predicting the aerodynamic loads and the flapwise bending moments experienced by the blades of a rotor in steady translational flight has been developed. The blade representation which is used satisfies the chordwise aerodynamic boundary condition, and a simplified discrete vortex filament representation is used for the wake of each blade. An iterative procedure was developed which yields a simultaneous solution for the aerodynamic loads and dynamic response experienced by the rotor blades.</p> <p>The lift loadings and bending moments were computed for two flight conditions of the H-34 and the HU-1A rotors. Comparisons of these results with measured results are presented as time histories and radial distributions of the harmonic components.</p>		

Unclassified

Security Classification

14 KEY WORDS		LINK A		LINK B		LINK C	
		ROLE	WT	ROLE	WT	ROLE	WT
Helicopter Rotor Blades Aerodynamic Loads Dynamics							

INSTRUCTIONS

1. ORIGINATING ACTIVITY: Enter the name and address of the contractor, subcontractor, grantee, Department of Defense activity or other organization (*corporate author*) issuing the report.

2a. REPORT SECURITY CLASSIFICATION: Enter the overall security classification of the report. Indicate whether "Restricted Data" is included. Marking is to be in accordance with appropriate security regulations.

2b. GROUP: Automatic downgrading is specified in DoD Directive 5200.10 and Armed Forces Industrial Manual. Enter the group number. Also, when applicable, show that optional markings have been used for Group 3 and Group 4 as authorized.

3. REPORT TITLE: Enter the complete report title in all capital letters. Titles in all cases should be unclassified. If a meaningful title cannot be selected without classification, show title classification in all capitals in parenthesis immediately following the title.

4. DESCRIPTIVE NOTES: If appropriate, enter the type of report, e.g., interim, progress, summary, annual, or final. Give the inclusive dates when a specific reporting period is covered.

5. AUTHOR(S): Enter the name(s) of author(s) as shown on or in the report. Enter last name, first name, middle initial. If military, show rank and branch of service. The name of the principal author is an absolute minimum requirement.

6. REPORT DATE: Enter the date of the report as day, month, year, or month, year. If more than one date appears on the report, use date of publication.

7a. TOTAL NUMBER OF PAGES: The total page count should follow normal pagination procedures, i.e., enter the number of pages containing information.

7b. NUMBER OF REFERENCES: Enter the total number of references cited in the report.

8a. CONTRACT OR GRANT NUMBER. If appropriate, enter the applicable number of the contract or grant under which the report was written.

8b, 8c, & 8d. PROJECT NUMBER: Enter the appropriate military department identification, such as project number, subproject number, system numbers, task number, etc.

9a. ORIGINATOR'S REPORT NUMBER(S): Enter the official report number by which the document will be identified and controlled by the originating activity. This number must be unique to this report.

9b. OTHER REPORT NUMBER(S): If the report has been assigned any other report numbers (*either by the originator or by the sponsor*), also enter this number(s).

10. AVAILABILITY/LIMITATION NOTICES: Enter any limitations on further dissemination of the report, other than those imposed by security classification, using standard statements such as:

- (1) "Qualified requesters may obtain copies of this report from DDC."
- (2) "Foreign announcement and dissemination of this report by DDC is not authorized."
- (3) "U. S. Government agencies may obtain copies of this report directly from DDC. Other qualified DDC users shall request through _____."
- (4) "U. S. military agencies may obtain copies of this report directly from DDC. Other qualified users shall request through _____."
- (5) "All distribution of this report is controlled. Qualified DDC users shall request through _____."

If the report has been furnished to the Office of Technical Services, Department of Commerce, for sale to the public, indicate this fact and enter the price, if known.

11. SUPPLEMENTARY NOTES. Use for additional explanatory notes.

12. SPONSORING MILITARY ACTIVITY. Enter the name of the departmental project office or laboratory sponsoring (*paying for*) the research and development. Include address.

13. ABSTRACT Enter an abstract giving a brief and factual summary of the document indicative of the report, even though it may also appear elsewhere in the body of the technical report. If additional space is required, a continuation sheet shall be attached.

It is highly desirable that the abstract of classified reports be unclassified. Each paragraph of the abstract shall end with an indication of the military security classification of the information in the paragraph, represented as (TS), (S), (C) or (U).

There is no limitation on the length of the abstract. However, the suggested length is from 150 to 225 words.

14 KEY WORDS Key words are technically meaningful terms or short phrases that characterize a report and may be used as index entries for cataloging the report. Key words must be selected so that no security classification is required. Identifiers, such as equipment model designation, trade name, military project code name, geographic location, may be used as key words but will be followed by an indication of technical context. The assignment of links, rules, and weights is optional.

Unclassified

Security Classification